technische universität
dortmund

Structure and electronic properties of supported noble metal clusters

Dissertation

zur Erlangung des Doktorgrades der Naturwissenschaften
der Fakultät Physik der Technischen Universität Dortmund

vorgelegt von
Sabrina Hoffmann

Dortmund, Dezember 2012

Contents

1 Introduction and motivation

Nanoparticles are widely known from media and their use in fashionable products such as sun protecting cremes and antiperspirant. However, such nanoparticles and small clusters are no new invention of the 21st century. Gold clusters of different sizes have already been used in medieval times to produce colored glass for beautiful windows, which can still be found in our days in churches such as the Cologne Cathedral (figure 1.1). The size of the used gold particles hereby determines the resulting color, e.g. the red color in the church window. Remarkably, the medieval glaziers did not have the scientific background and knowledge gained from fundamental research, which is accessible in our times.
Today the visible color is well known to be the result of absorption of light by noble metal clusters of a distinct size inside the glass. Another impressive example for such an absorption of light is the so called Lycurgus Cup, which is a Roman artifact from the fourth century (figure 1.2). The glass used to produce this cup consists of numerous small gold droplets, which absorb a specific energy range of the impinging light spectrum resulting in a bright red color for transmitted light.
In 1857 Michael Faraday published first experimental results on the relations of gold to light [Far57], in which he presented different color effects for gold particles of different size and shape. A theoretical approach to the absorption of light by small spherical gold particles was first released by Gustav Mie in 1908 [Mie08] predicting a collective excitation of the conduction electrons. A lot of time has passed since these beginnings of the so called plasmonics, the interaction of light with matter, a highly interesting topic for present and future research and application.
The following introduction will first give a short explanation of clusters and their special structural properties as well as the interaction of noble metal clusters with light. Subsequently, a brief overview on the structure and the contents of this thesis.

Regarding matter a cluster can be found between the physics of a single atom on the one side and condensed matter physics with long range ordered crystal structures on the other side. This intermediate state is situated in the region of three to a few thousand atoms and a size scale of 10^0-10^1 nm. Here, the structure and thus, the electronic properties of noble metal clusters alter significantly with size and shape as well as with the environmental properties. For use in present and future applications such as i.e. nanoantennas [Mer08] or biosensors [Hae02, Bro12] (figure 1.3) it is essential to know the size and structure of the used clusters and particularly environmentally induced changes of their structure and electronic properties.
For other applications of clusters such as catalysis [Li,08] or the enhancement of solar cells [Wes00] knowledge of the size, the geometrical structure and electronic properties are inevitable, particularly in contact to other materials such as a substrate or a matrix, into which the clusters are embedded.

Figure 1.1: Picture of an old colorful church window as found in the Cologne Cathedral. The red color originates from small gold clusters in the glass. Picture adapted from [Ley08].

Figure 1.2: Picture of the Lycurgus Cup, a Roman artifact from the fourth century. Due to noble metal particles in the used glass the cup appears green in reflected light and red in transmitted light. Picture adapted from [Leo07].

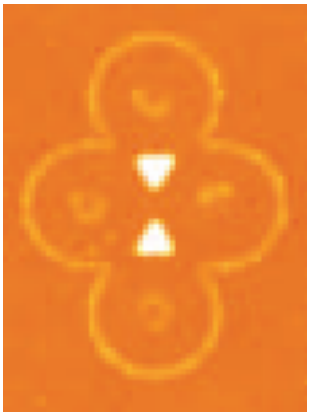

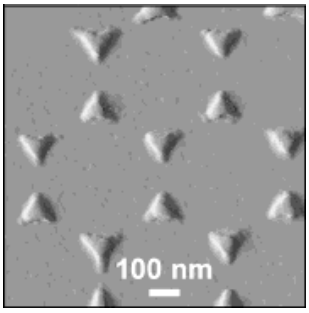

Figure 1.3: Left: Resonant optical nanoantennas [Mer08], right: nanoscale optical biosensors [Hae02].

Optical spectroscopy measurements of the cluster plasmon resonance are a well known experimental method to determine the electronic properties of small metal clusters with respect of their size and shape. It is suited to investigate the influence of a matrix material on the free electron oscillations in noble metal clusters.

The structural properties of silver clusters such as lack of long range order and no periodic crystal structure combined with a large fraction of surface atoms yield an alteration of the density of states compared to crystalline silver. Using the element specific x-ray absorption spectroscopy, in which a core electron is excited to an unoccupied state by an impinging photon, it is possible to probe the unoccupied density of states [Kon88]. The method is highly sensitive to changes in the oxidation state of the investigated element.

This thesis is organized as follows. **Chapter 2** gives an overview of the theory of cluster formation in a supersonic nozzle expansion combined with a short introduction to the gas dynamics of this process and the mechanics of cluster condensation.
In a second section the optical properties of noble metal clusters are introduced starting with the Mie theory in quasi static approximation for spherical clusters and taking into account influences such as the free path effect resulting in surface damping due to the finite size of the cluster, interband transitions and chemical interface damping. Subsequently, the theory is altered to account for the ellipsoidal shape of deposited clusters followed by an introduction of the measurand extinction.
The following sections give an overview of inelastic x-ray scattering and the influence of the oxidation state on the unoccupied density of states followed by a short description of the ab-initio calculation software FEFF9 [Reh10].

Chapter 3 provides an overview of the experimental setups such as the THErmal CLuster Apparatus (THECLA), with which all investigated samples are prepared, the setup used for the optical spectroscopy measurements and a short descriptions of the experimental endstations used for the x-ray absorption measurements.

In **chapter 4** a summary of the investigated sample systems is provided followed by the results gained from optical spectroscopy and x-ray absorption spectroscopy. Subsequently, the x-ray absorption measurements are compared to ab-initio calculations for better quantification of the results.

The thesis ends in **chapter 5** with a summary of the conclusions gained from the two experimental methods as well as an outlook on further questions and investigations.

2 Theory

2.1 Theory of the cluster formation in a supersonic nozzle expansion

All investigated samples presented in this thesis were produced in a supersonic nozzle expansion using the cluster source THErmal CLuster Apparatus (THECLA) designed by Hövel [Höv95]. The idea behind this cluster source originally was to be able to produce a highly intense focused cluster beam, which allowed the investigation of free Ag clusters in comparison to the same clusters deposited on a certain substrate or into a matrix. The choice of a nozzle expansion for the formation of clusters originates from the necessity of large amounts of clusters, which are emitted in a shallow angle close to the beam axis. Other methods such as production of clusters in a gas aggregation source or in a magnetron

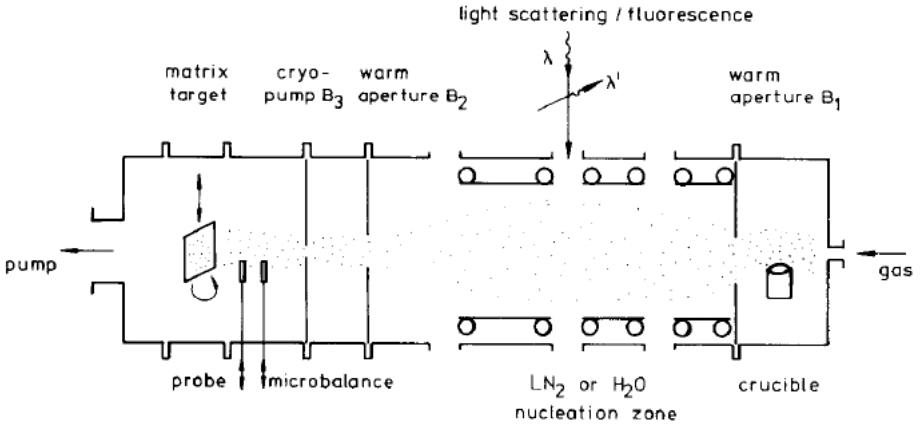

Figure 2.1: Scheme of a typical gas aggregation source [Fra85].

sputtering source yield cluster beams of a much lower intensity, which were not suitable for the afore mentioned application. In the gas aggregation source (figure 2.1) the cluster material is vaporized into an inert noble gas, where the molecules are cooled by collisions with the gas atoms. When the temperature of the cluster material reaches a certain value agglomeration occurs. The cluster-gas-mixture is then guided through a system of apertures into the vacuum chamber. Since the cluster current is nondirectional, a large number of clusters remains in the source chamber.
In a laser ablation source (figure 2.2) a laser pulse is focused on a target consisting of the cluster material, thus, dissolving several atom layers of the material partly ionizing the atoms. The forming plasma (T= 10000-20000 K) is then expanded into a helium (He)

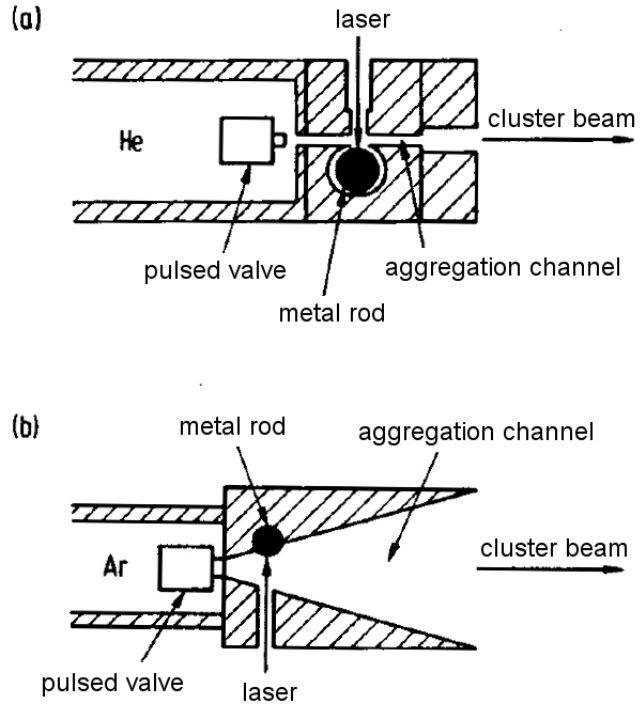

Figure 2.2: Laser ablation sources (R.E. Smalley): a) Formation of pure metal clusters, b) Embedding a metal atom inside an Ar cluster [Hab92].

atmosphere, where it is cooled down by collisions with the He atoms. The achievable cluster current, which is in direct relation to the quantity of clusters produced in this cluster source, is too low for the original purpose of THECLA.

The following sections give a brief description of the gas dynamics of a supersonic expansion as well as an insight in the condensation parameters and optical response of metal clusters. Subsequently, the interaction of x-ray radiation with matter and precisely, the absorption of an impinging x-ray photon by an atom will be explained.

2.1.1 Gas dynamics of a supersonic expansion

Regarding the expansion of a gas from a region of high pressure through an orifice to a region of low pressure, two limit cases are known for the acceleration of the gas molecules, which can be characterized using the Knudsen number $Kn = \overline{\ell}/d$ (figure 2.3). If the mean

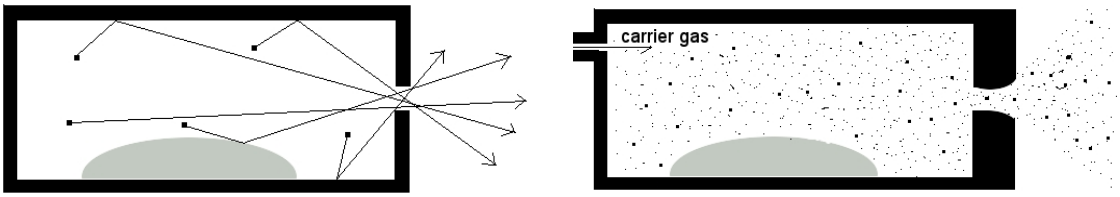

Figure 2.3: Left: Molecular flow with $Kn = \overline{\ell}/d \gg 1$, right: Supersonic expansion with $Kn = \overline{\ell}/d \ll 1$.

free path of the molecules $\overline{\ell}$ is much bigger than the diameter of the orifice d, the molecules can pass the orifice almost without collisions between the particles. The so called molecular flow is used e.g. to produce epitaxially grown layers.
If the vapor pressure in the chamber rises, the mean free path of the molecules $\overline{\ell}$ decreases. For a Knudsen number $Kn = \overline{\ell}/d \ll 1$ the molecules can collide inside the orifice yielding a supersonic flow, which can be described with the dynamics of a gas continuum. In this adiabatic expansion the particles are cooled down and highly focused in the direction of the beam axis.
The following description of the gas dynamics is based on Hövel [Höv95]. For a one dimensional flow through a flow tube with decreasing cross-section (figure 2.4) the expansion of an ideal gas from an initial state with pressure p_0, temperature T_0, cross-section A_0 and velocity v_0 to the final state (marked with 1) is adiabatic and isentropic, thus, mass and energy are conserved. In this expansion there is neither heat transfer with the environment ($\Delta Q = 0$) nor a change of the entropy for reversible processes ($\Delta S = 0$)[Fri73].

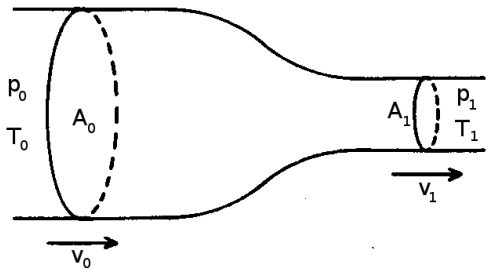

Figure 2.4: Flow tube with decreasing cross-section.

For an ideal gas with $pV = nRT$, where p denotes the pressure, V is the volume, T the temperature, n is the quantity of material and R denotes the universal gas constant, the combination of energy and mass conservation yields

$$\frac{1}{2}v_0^2 + c_\mathrm{p}T_0 = \frac{1}{2}v_1^2 + c_\mathrm{p}T_1 \,, \tag{2.1}$$

with c_p denoting the specific heat of the ideal gas.
If the initial velocity in flow direction is $v_0 = 0$ at a temperature T_0, equation (2.1) becomes

$$c_p T_0 = \frac{1}{2} v_1^2 + c_p T_1 \,. \tag{2.2}$$

By introducing the Mach number $M := v/a$ with the local sonic velocity a

$$a = \sqrt{\gamma \frac{kT}{m}} \,, \tag{2.3}$$

the adiabatic exponent $\gamma = c_p/c_v$, the Boltzmann constant k and the mass of the gas particles m with

$$c_p = \frac{\gamma}{\gamma - 1} \frac{k}{m} \,, \tag{2.4}$$

equation (2.2) holds

$$\frac{T_1}{T_0} = \left(1 + \frac{1}{2}(\gamma - 1) M^2\right)^{-1} \,. \tag{2.5}$$

Using the Poisson equation [Wut92]

$$\left(\frac{p_1}{p_0}\right) = \left(\frac{V_0}{V_1}\right)^{\gamma} = \left(\frac{T_1}{T_0}\right)^{\gamma/(\gamma-1)} = \left(\frac{\rho_1}{\rho_0}\right)^{\gamma} \tag{2.6}$$

the local pressure and density along the beam axis hold

$$\frac{p_1}{p_0} = \left(\frac{T_1}{T_0}\right)^{\gamma/(\gamma-1)} \,, \tag{2.7}$$

$$\frac{\rho_1}{\rho_0} = \left(\frac{T_1}{T_0}\right)^{1/(\gamma-1)} \,. \tag{2.8}$$

A relation between the Mach number and position during expansion follows from mass conservation

$$\rho_1 A_1 v_1 = \rho_2 A_2 v_2 \,. \tag{2.9}$$

With "*" denoting the state, in which $M = 1$, the following relation can be obtained

$$\frac{A}{A^*} = \frac{\rho^* v^*}{\rho v} = \frac{\rho^* a^*}{\rho M a} = \frac{\rho^*}{M \rho} \left(\frac{T^*}{T}\right)^{1/2} = \frac{1}{M} \left(\frac{1 + \frac{1}{2}(\gamma - 1)}{1 + \frac{1}{2}(\gamma - 1) M^2}\right)^{-1/(\gamma-1)-1/2} \,. \tag{2.10}$$

In an expansion through a flow tube with a circular cross-section the change to supersonic flow occurs at the position with the smallest diameter where $M = 1$. During the acceleration of the gas molecules in the adiabatic expansion the Mach number and thus, the

velocity v increases, while the temperature $T_1 \longrightarrow 0$ (see equation (2.5)). For large M the beam velocity v, which holds

$$v = M \cdot a = M \cdot a_0 \left(\frac{T}{T_0}\right)^{1/2} \tag{2.11}$$

with $a_0 = \sqrt{\gamma \frac{kT_0}{m}}$ approaches a maximum

$$v_\infty = a_0 \sqrt{\frac{2}{\gamma - 1}}\,, \tag{2.12}$$

which for a monoatomic gas with $\gamma = \frac{5}{3}$ corresponds to $v_\infty = 2.24 \cdot \sqrt{\frac{kT_0}{m}}$.
This very simple model of a one-dimensional flow holds for a supersonic nozzle as long as the opening angle 2α remains small. For a nozzle with a conical supersonic area (figure 2.5), an opening angle of $2\alpha = 10°$, a diameter at the narrowest point of $d \approx 0.42$ mm and a length of $L \approx 25$ mm most of the thermal velocity of the gas molecules, which is aimed at all directions in space is transformed into velocity in flow direction through collisions between the particles. The acceleration further yields a cooling of the gas, which results in a decrease of the collision probability. Thus, at the end of the supersonic nozzle the cold particle flow is strongly aligned to the beam axis with thermal velocity $v_{\text{therm}} \longrightarrow 0$.

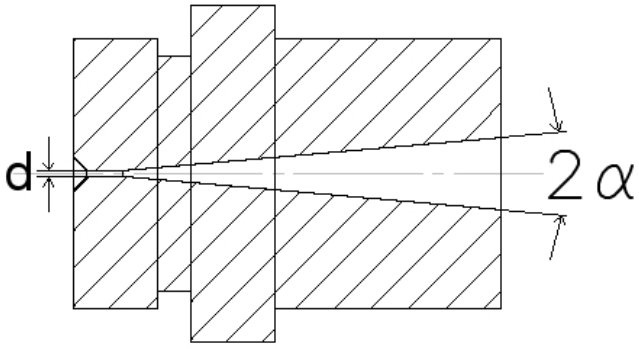

Figure 2.5: Scheme of a conical supersonic nozzle.

2.1.2 Problems regarding the supersonic expansion

The model of a one-dimensional continuous flow holds for a realistic supersonic expansion as long as the molecules and the agglomerating clusters perform sufficient collisions. Since the particle density decreases fast with ongoing expansion the supersonic flow can turn into a molecular flow. Thus, the Mach number will not rise infinitely but approaches a maximum [And74], which is proportional to the Knudsen number

$$M_T = \text{const.}\,(Kn)^{-0.4}\ . \tag{2.13}$$

In contrast to the afore introduced simple model four different temperatures have to be considered for the flow dynamics. As long as the expansion is in accordance with a supersonic flow the temperature distributions parallel and perpendicular to the flow direction ($T_\parallel, T_\perp$) and the temperatures related to the rotational and vibrational degrees of freedom ($T_{\text{rot}}, T_{\text{vib}}$) are equal. For a molecular flow the temperatures reach different final values ($T_\parallel \leq T_\perp \leq T_{\text{rot}} \leq T_{\text{vib}}$).
An additional difficulty arises from the fact that the vacuum, into which the gas molecules are expanded is not perfect. The gas, which remains inside the experimental chamber due to the limited pumping speed, can interact with the gas beam of the cluster source in different ways.

- For high background pressures the flow speed can be reduced very abruptly ($M < 1$) yielding the formation of a so called Mach disk at position [Bie61, Bie62]

  $$x_M \approx 0.65 \cdot d\sqrt{\frac{p_0}{p_1}} \tag{2.14}$$

  on the beam axis. The position depends on the diameter of the nozzle d, the pressure p_0 and the background pressure p_1. For constant gas flow $q \propto d^2 p_0$ and pumping speed $S = q/p_1$ the position of the Mach disk is independent of pressure and diameter of the nozzle and thus constant.

- For low background pressure the hard shock front becomes weaker and for a certain low density of the background atoms no Mach disk appears. Thus, the perturbations of the supersonic flow can be treated as deflection by background atoms.

To account for these limitations the positions of the cluster source and the aperture system are well chosen inside THECLA.

2.1.3 Theoretical approach to cluster condensation in a supersonic expansion

The expansion of a supersaturated gas into vacuum yields a supersonic flow in which, for the right choice of temperature, pressure and diameter of the nozzle, condensation to clusters may occur. After Hagena [Hag81] the thermodynamic process can be described as follows (figure 2.6).

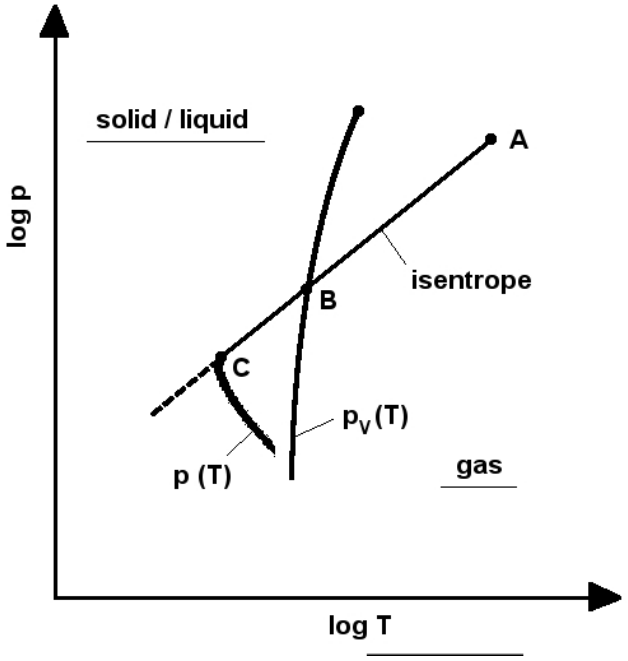

Figure 2.6: Expansion line $p(T)$ and vapor pressure curve $p_v(T)$ of a condensing gas double-logarithmically printed [Hag81].

Starting from stagnation conditions T_0 and p_0 at point A the gas expands along the isentrope up to point B where the vapor pressure curve $p_v(T)$ crosses. This marks equilibrium between the gas phase and the solid/liquid phase. From this point of equilibrium the expansion follows the isentrope into the supersaturated region, where at point C the formation of clusters sets in and leads to a collapse of the supersaturated state. The expansion then turns to the equilibrium line $p_v(T)$. The position of the "onset-point" C depends on the stagnation conditions at point A, the thermodynamics e.g. temperature T_B of the saturation point and the nozzle geometry, which determines the kinetics and time scale of the expansion.
Figure 2.7 shows a sketch of the condensation in a supersonic nozzle as shown in [Weg70].
A detailed theoretical description of the condensation is still a demanding task. Here, the interacting mixture forms an equilibrium concentration, which could be derived from equilibrium cluster density via sums of states using kinetic models and statistical thermodynamics. Still, for molecular gases rotational and oscillational degrees of freedom and electronic states for metallic molecules have to be taken into account. Additionally, in the supersaturated state the equilibrium state consists of only one condensed phase instead of

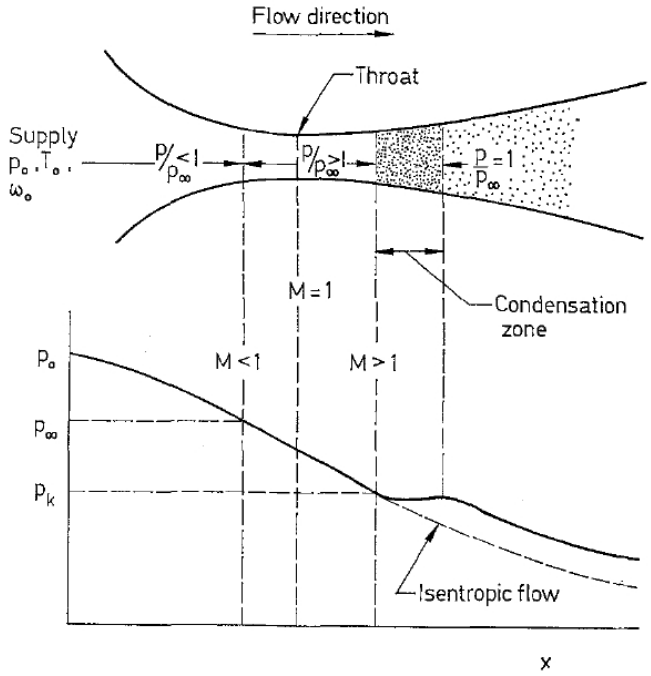

Figure 2.7: Sketch of the condensation process in a supersonic nozzle with stagnation conditions T_0, p_0, the saturation ratio p/p_∞, Mach number M, solid/vapor phase equilibrium pressure p_∞ and condensation pressure p_k [Weg70].

a gas-cluster-mixture.
Up to now the nucleation process still is not completely understood. Publications from 2004 and 2005 were still looking for the exact theory to describe the kinetics of cluster growth [Nap04, Kra05] taking into account collisions between atoms and clusters. Here it is important to keep in mind that most of these collisions do not result in cluster growth but mainly serve as cooling mechanism by transferring the condensation heat to the colliding gas molecules.
Recent work on the calculation of homogeneous cluster condensation in supersonic flows from Jansen et al. [Jan10, Jan11] show reasonable agreement with experimental data taken for water cluster and ammonia cluster condensation in a supersonic flow [Bob02]. For their simulation they take into account creation of dimers through collision stabilization of collision complexes, elastic monomer-cluster collisions, which change internal energies of the colliding particles, inelastic monomer-cluster collisions resulting in monomer sticking, cluster-cluster coalescence and evaporation of monomers from clusters [Jan11].
Still, they do not take into account rotational degrees of freedom and metal clusters.

2.1.4 Scaling laws

An attempt to predict cluster formation in supersonic expansions has been made years ago by Hagena [Hag74, Hag87]. Due to the lack of precise theory he stated that for a constant nozzle diameter $d_{\mathrm{eq}} = \text{const.}$ similar condensation conditions are given for equal values of the so called reduced scaling parameter Γ^* with

$$\Gamma^* = \left(n_0 r_{\mathrm{ch}}^3\right) \cdot \left(\frac{D}{r_{\mathrm{ch}}}\right)^q \cdot \left(\frac{T_0}{T_{\mathrm{ch}}}\right)^{0.25 \cdot q - 1.5} , \tag{2.15}$$

and the parameters describing the supersonic expansion, i.e. the density n_0, the temperature T_0 of the gas in front of the nozzle and the diameter D of a nozzle without supersonic cone. The parameter q lies in between the limits $0.5 < q \leq 1$.
For noble gas clusters q was determined experimentally to be $q \approx 0.85$. The properties of the gas are described by a characteristic length

$$r_{\mathrm{ch}} = \left(\frac{m}{\rho_s}\right)^{1/2} \tag{2.16}$$

with the atomic mass m and the bulk density ρ_s, and a characteristic temperature

$$T_{\mathrm{ch}} = \frac{\Delta h_0^0}{k} \tag{2.17}$$

with the sublimation enthalpy Δh_0^0 and the Boltzmann constant k. For Γ^* in the range of 200 to 1000 cluster condensation sets in. For even bigger values the cluster quantity and size increase. With a typical nozzle diameter D of a few $1/10$ mm the reachable partial pressure and thus, the density for silver as cluster material does not result in a Γ^* high enough for cluster formation. Since an increase in nozzle diameter results in a high increase of used cluster material, the utilization of a nozzle with a conical supersonic region with small opening angle 2α is suitable. This conical part of the nozzle increases the time before the supersonic flow turns into a molecular flow.
With a Mach number on the beam axis $M(x)$ in an expansion from a conventional sonic nozzle with $x \gg D$ and $\gamma = 5/3$ [And74]

$$M(x) \approx \left(5.83 \frac{x}{D}\right)^{1.67-1} \tag{2.18}$$

and the geometry of the supersonic nozzle

$$\frac{A}{A^*} = \left(2 \frac{x}{D} \tan\alpha\right)^2 , \tag{2.19}$$

which follows after equation (2.10) in combination with equation (2.19), the Mach number for an expansion from a supersonic nozzle can be expressed as

$$M(x) \approx \left(5.83 \frac{x}{(0.736 \cdot D / \tan\alpha)}\right)^{1.67-1} . \tag{2.20}$$

Thus, the flow of a supersonic nozzle for $M \gg 1$ corresponds to the flow of a sonic nozzle with a diameter of

$$D_{\mathrm{eq}} = 0.736 \frac{D}{\tan \alpha} \,. \tag{2.21}$$

With $\alpha = 5^\circ$ for the here used nozzle the effective diameter becomes

$$D_{\mathrm{eq}}^{\alpha=5^\circ} = 8.4D \,. \tag{2.22}$$

Thus, the used material reduces with a factor $(8.4)^2 = 71$. The addition of a carrier gas such as argon yields another reduction of a factor 4 [Hag91, Hag81], which results in a Γ^* increased by a factor 4.

2.2 Optical properties of small noble metal clusters

In the following sections the interaction of light with small metal clusters will be discussed starting from a quasi-static approximation of the Mie theory [Mie08, Boh83, Kre95] for single spherical clusters. Further on the influence of the cluster surface in the so called free path effect will be discussed as well as the alteration of the theory due to deposition induced cluster deformation. Additionally, the influence of the environment such as a matrix, in which the clusters are embedded, will be discussed.

2.2.1 Basic principles of absorption of light in metal clusters

Regarding the absorption of light in bulk silver, the optical constants in the visible region consist of two parts: the collective movement of the free conduction band electrons and interband transitions, which yield optical absorption. As an interband transition is a transition between conduction and valence bands the so called intraband transition is a transition between occupied and unoccupied quantized levels in the conduction band. Figure 2.8 shows the bandstructure for bulk silver. The occupied density of states was measured with UV photo emission spectroscopy (UPS) by Wern [Wer85] and the unoccupied density of states was calculated by Eckardt et al. [Eck84].
The visible energy gap between the highest occupied energy levels (HOMO) and the Fermi energy E_F of silver near the L-point of the Brillouin zone is 3.8 eV. This energy gap is the direct interband transition with the lowest energy, which marks the interband absorption edge from 4d-band to 5sp-band. The use of optical absorption spectroscopy to probe the absorption of light in silver yields the joint density of states. In an optical absorption spectrum the 4d-5sp energy gap is seen around 3.88 eV with the absorption occurring from collective excitations of the free electrons in the lower energy region and the interband transitions above 3.88 eV.
For Ag clusters of approximately 250 atoms, which is the mean size of the clusters investigated here, the optical absorption alters significantly especially due to the limited size and thus, the influence of the surface. The alteration can be seen in the region where the collective oscillation of the free electrons appear in the spectra as the so called cluster plasmon resonances. These oscillations are damped due to the cluster surface, which will be explained in detail in the following sections.
The resonance resulting from the oscillating electrons can be described with the quasi-static Mie theory [Mie08, Boh83] for a single spherical metal particle and can thus be called Mie resonance. Figure 2.9 shows the absorption of light for small spherical silver clusters compared to the resonance-free absorption of a silver film with similar thickness.
The different parts of the absorption for the silver clusters originating from collective electron excitations and interband transitions can clearly be distinguished. The interband transitions can be found below 320 nm (3.88 eV), which marks the absorption edge for transitions between the 4d- and 5sp-band, the electron oscillations lie above 320 nm. For silver bulk the volume plasma resonance lies shortly below the interband edge around 3.8 eV. The absorption spectrum was calculated using a simplified model for individual spherical silver clusters, in which the conduction electrons are treated as a free electron gas in a

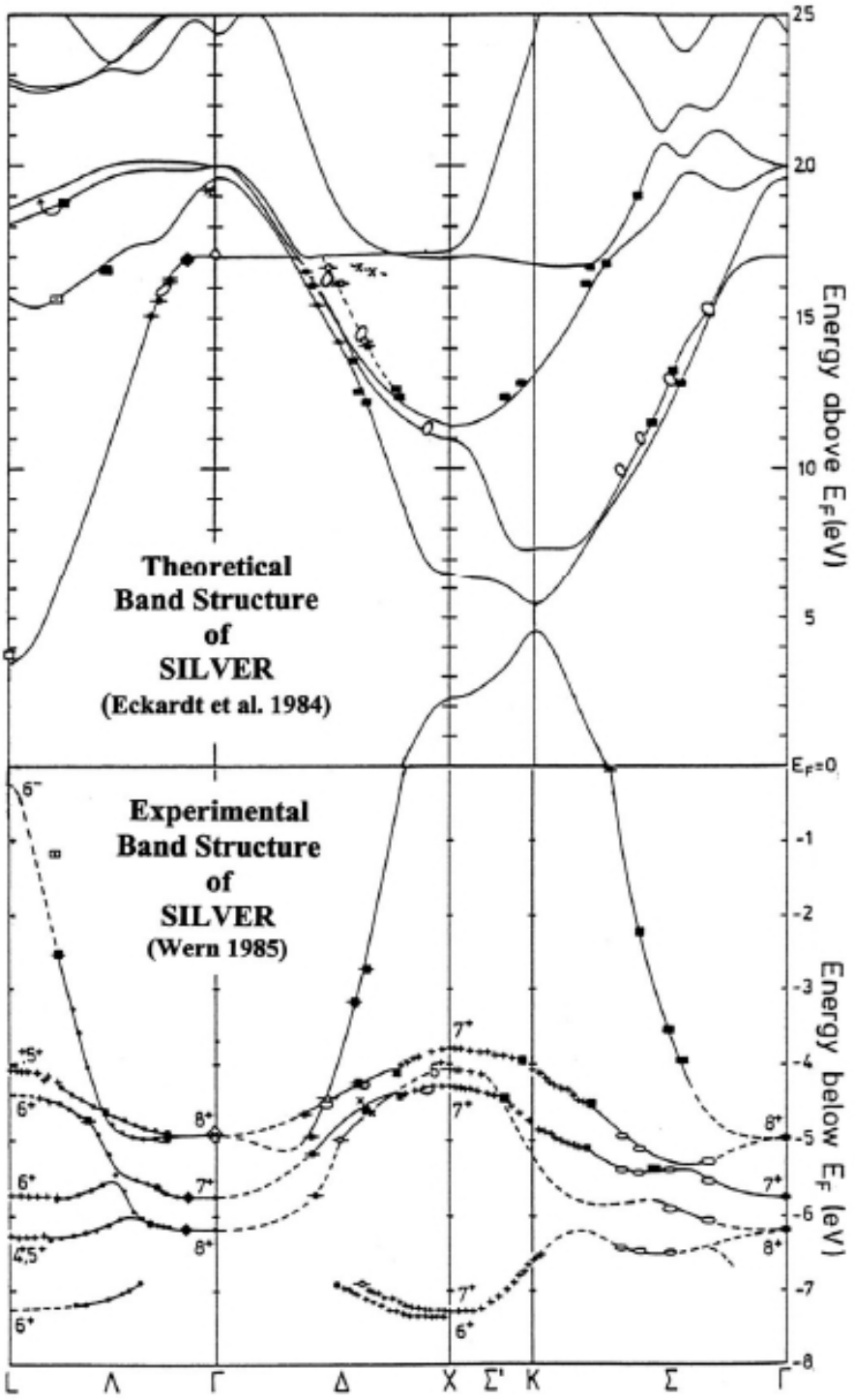

Figure 2.8: Bandstructure of bulk silver. Occupied density of states measured with UPS [Wer85], unoccupied density of states calculated [Eck84]. Picture taken from [Hil01].

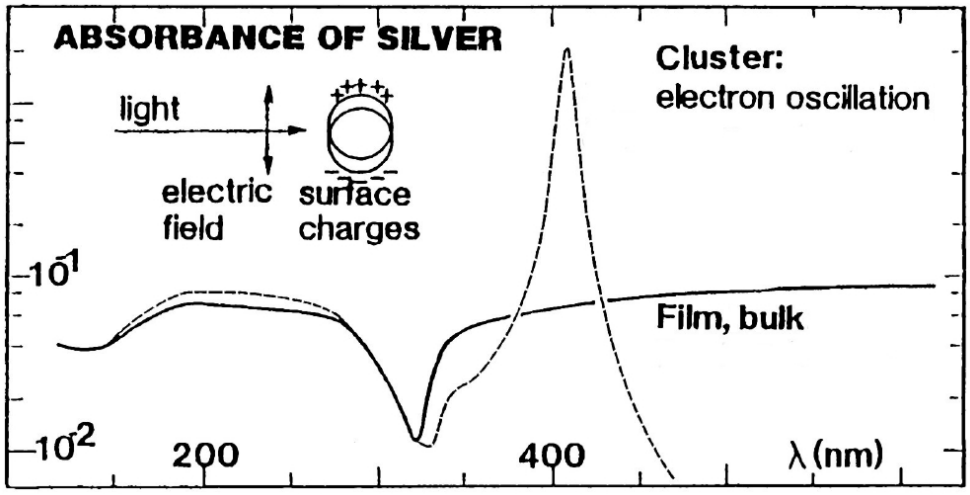

Figure 2.9: Absorption behavior of silver clusters and bulk silver in the spectral region 100 to 600 nm. The absorption resulting from excitations of the free electrons lies above 320 nm (3.88 eV band gap), the interband transitions can be found below 320 nm. The optical excitation between the 4d- and 5sp-band around 320 nm is seen as an optical interband edge (joint density of states). Picture taken from [Kre95].

quasi-static approximation: the electric field of the light wave excites the electrons, which start to oscillate against the positively charged atoms (dipole approximation).

2.2.2 Mie theory in quasi-static dipole approximation and dielectric function of realistic metals

For small spherical metal clusters with a diameter $2R$ and a complex dielectric function $\epsilon(\omega) = \epsilon_1(\omega) + i\epsilon_2(\omega)$ in an environment with a real dielectric constant ϵ_m the Mie theory describes the whole absorption process from a classical electrodynamical point of view [Mie08]. Using the Maxwell equations it is possible to get analytical terms for the interaction cross-sections such as the absorption cross-section σ_{abs}, the scattering cross-section σ_{scat} and the extinction cross-section $\sigma_{\text{ext}} = \sigma_{\text{abs}} + \sigma_{\text{scat}}$, which consist of spherical harmonics to account for the possible multipole resonances.
For spherical clusters with diameter much smaller than the wavelength of the incident light $2R \ll \lambda$ (precisely for silver clusters: $2R < 15$ nm) the scattering cross-section becomes negligible compared to the absorption cross-section yielding an extinction cross-section that only consists of dipole absorption [Boh83]:

$$\sigma_{\text{ext}} = \sigma_{\text{abs}} = 9\frac{\omega}{c}\epsilon_m^{3/2}V_0\frac{\epsilon_2(\omega)}{\left[\epsilon_1(\omega) + 2\epsilon_m\right]^2 + \epsilon_2(\omega)^2} . \tag{2.23}$$

Here, c denotes the vacuum light velocity and $V_0 = (4/3)\,\pi R^3$ is the volume of the cluster. For a frequency ω_1 the dipole absorption cross-section has a resonance with

$$\epsilon_1(\omega_1) \approx -2\epsilon_m , \tag{2.24}$$

if $\epsilon_2(\omega)$ is not too large or does not alter significantly around ω_1. Developing the dielectric function around ω_1 with

$$\begin{aligned} \epsilon_1(\omega) &\approx -2\epsilon_m + \left(\left.\frac{d\epsilon_1(\omega)}{d\omega}\right|_{\omega_1}\right)(\omega - \omega_1) , \\ \epsilon_2(\omega) &\approx \epsilon_2(\omega_1) \qquad \text{for } \omega \approx \omega_1 \end{aligned} \tag{2.25}$$

yields the full width at half maximum (FWHM) Γ of the resonance structure

$$\Gamma \approx \frac{2\epsilon_2(\omega_1)}{\left|\left(\left.\frac{d\epsilon_1(\omega)}{d\omega}\right|_{\omega_1}\right)\right|} . \tag{2.26}$$

The resonance structure in σ_{ext} after (2.23) for $\epsilon_1(\omega_1) = -2\epsilon_m$ can be understood as a resonant collective oscillation of the conduction electrons against a uniform static positive background (jellium model) with ϵ_2 damping the oscillation. This structure will be denoted cluster plasmon resonance although for a realistic metal not only the free electrons influence the dielectric function.
To describe a more realistic metal, the afore shown Drude dielectric function has to be expanded to interband transitions, which yield an additional susceptibility

$$\chi^{\text{Inter}}(\omega) = \chi_1^{\text{Inter}}(\omega) + i\chi_2^{\text{Inter}}(\omega) . \tag{2.27}$$

Thus, the dielectric function in the ultraviolet and visible spectral region becomes

$$\epsilon(\omega) = 1 + \chi^{\text{Drude}}(\omega) + \chi^{\text{Inter}}(\omega) = 1 - \frac{ne^2/(\epsilon_0 m_{\text{eff}})}{\omega^2 + i\gamma_0\omega} + \chi^{\text{Inter}}(\omega) . \tag{2.28}$$

2.2.3 Free path effect and Drude dielectric function of small metal clusters

In small metal clusters the cluster surface has a damping effect on the collective electron oscillations as it limits the mean free path l_∞ of the electrons [Kre69, Kre70]. If l_∞ becomes comparable to the cluster size the electrons start to interact with the surface yielding an additional contribution to the damping constant γ_0. Usually, the mean free path of electrons in bulk metals is comparably large. From data given in [Ehr62] the mean free path of silver is $l_\infty = 52$ nm at room temperature.
The free path model treats processes that yield damping in bulk material as well as in clusters such as scattering from phonons, lattice defects and from the cluster surface as independent. Thus, they add up to the total damping as

$$\gamma = \frac{1}{\tau} = \frac{1}{\tau_\infty} + \frac{1}{\tau_{\text{surf}}} = \frac{v_F}{l_\infty} + A \cdot \frac{v_F}{R} \,, \tag{2.29}$$

with the Fermi velocity v_F and the mean collision times τ_∞ and τ_{surf}. The parameter A includes the electron scattering from the cluster surface [Kre85].
The dielectric function of a metal cluster then becomes

$$\begin{aligned} \epsilon(\omega, R) &= \epsilon^{\text{bulk}} - \epsilon^{\text{bulk}}_{\text{Drude}} + \epsilon^{\text{damped}}_{\text{Drude}} \\ &= \epsilon^{\text{bulk}} - \frac{\left(-\omega_p^2\right)}{\omega^2 + i\omega\gamma_0} + \frac{\left(-\omega_p^2\right)}{\omega^2 + i\omega\left(\gamma_0 + Av_F/R\right)} \,. \end{aligned} \tag{2.30}$$

For good metals with $\gamma_0 \ll \omega_p$ in the region of the plasmon resonance the full width at half maximum then becomes

$$\Gamma(R) \approx \Gamma_0 + A \cdot \frac{2\omega_p^2/\omega_1^3}{\left|\left(\frac{d\epsilon_1}{d\omega}\big|_{\omega_1}\right)\right|} \cdot \frac{v_F}{R} \,. \tag{2.31}$$

Γ_0 denotes the full width at half maximum for the bulk metal plasmon resonance. Comparison between calculated size dependent dielectric functions after (2.30) and $A = 1$ from literature values for bulk silver and dielectric functions, which were gained through Kramers-Kronig analysis from spectra taken for Ag clusters in glass [Kre70], shows significantly high agreement (figure 2.10).

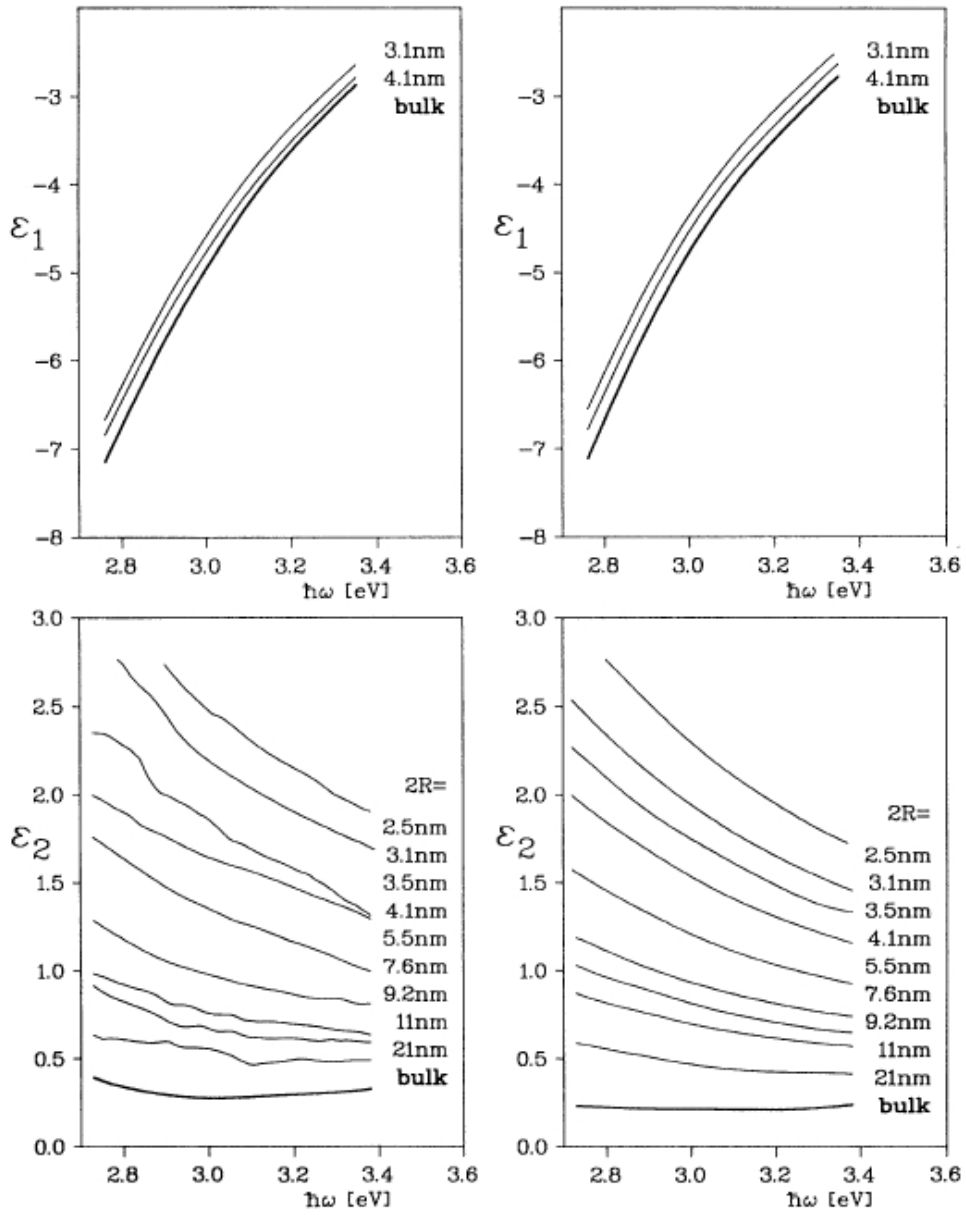

Figure 2.10: Alteration of the dielectric function of silver depending on cluster size [Höv93]. Left: Gained from extinction measurements through Kramers-Kronig analysis, right: Calculated from equation (2.30) and $A = 1$ for bulk silver [Kre70].

2.2.4 The influence of interband transitions

As already mentioned the dielectric function of a metal cluster in the ultraviolet and visible spectral region does not only consist of the absorption by excitation of collective electron oscillations but also of interband transitions. The susceptibility of bulk silver interband transitions χ^{Inter} can be described using transition matrix elements $\vec{e} \cdot M_{\text{if}}$ for transitions from an initial state E_{i} to a final state E_{f} and can be found by using Kramers-Kronig analysis [Bas75, Kra72, Kra76].
In a cluster most of the parameters influencing interband transitions can be altered compared to bulk material. Some of these are:

- Fermi energy and Fermi velocity
- effective mass m_{eff}
- transition probabilities M_{if}
- band structure: occupation and position of the energy levels for initial and final states $E_{\text{i}}, E_{\text{f}}$
- surface states
- lattice constant and structure and thus, band structure and density of conduction electrons

Regarding for example possible changes in the band structure due to size effects one can see that loss of the long range order as well as changes in the short range order occur yielding a shift and a broadening of the energy bands [Kra72, Kra76]. Changes in the transition probabilities M_{if} can be caused by the high percentage of surface atoms.
In optical measurements performed on silver clusters by Hövel [Höv95] it is visible that the slope parameter of the interband absorption edge for silver clusters is smaller than for bulk silver and that the edge is shifted to lower energies. Figure 2.11 shows the influence of the interband transitions on the dielectric function of silver. The upper part of the figure shows the real part ϵ_1, the dielectric function of the free electrons ϵ_1^{free} and the interband transitions $\delta\epsilon_1$, the lower part depicts the real and the imaginary part of the dielectric function, ϵ_1 and ϵ_2, respectively. Size dependent changes in the interband transitions may thus influence the cluster plasmon resonance if there is an overlap of the two absorption processes.
Not only the size of the cluster can influence the dielectric function, but a similar influence can be seen regarding temperature effects [Ott61, Kre74]. For higher temperatures the changes of the dielectric function are comparable to the size dependent changes, which could be explained by the loss of long range order and the decrease in the mean free path l_∞.

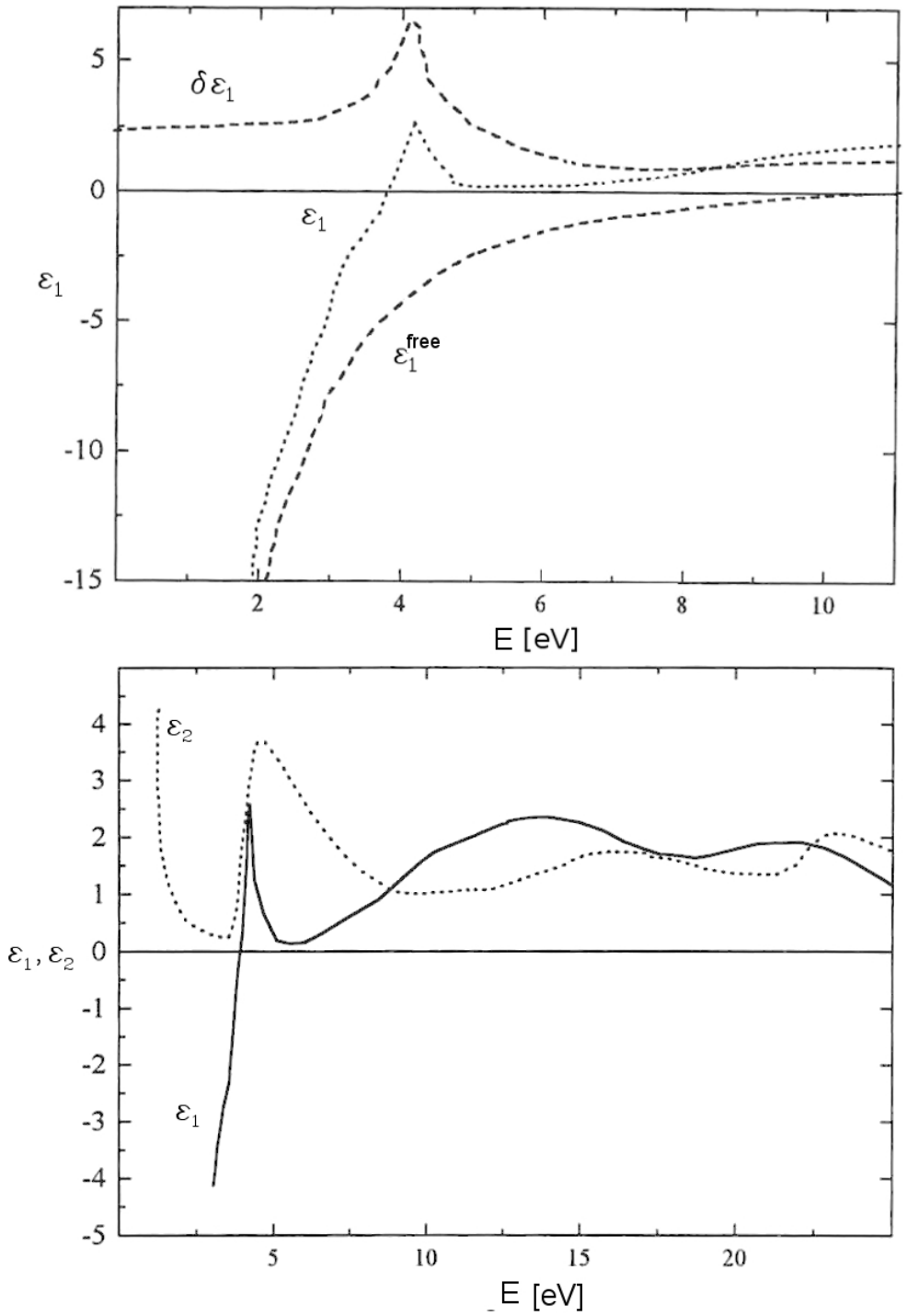

Figure 2.11: Influence of the interband transitions on the dielectric function of bulk silver. Top: Real part ϵ_1 of the dielectric function, ϵ_1^{free} free electron dielectric function, $\delta\epsilon_1$ interband transitions , bottom: Real and imaginary part of the dielectric function ϵ_1 and ϵ_2, respectively [Ehr62].

2.2.5 Chemical interface damping

As already mentioned before, the surface of small metal clusters has a large influence on their optical properties as can be explained with the free path effect. Another important aspect is not only the surface as a limit for oscillating conduction electrons but also the surrounding material such as i.e. an adsorbed layer on the cluster surface or a matrix, in which the clusters are embedded. Beyond the pure influence of the dielectric function ϵ_m of the surrounding material, the structure of the surface itself has a great impact on the cluster plasmon excitation. The so-called chemical interface damping will be introduced in the following section. Additionally, a very brief overview on a quantum mechanical model introduced by Persson [Per93] will be given, which enables a microscopic view on the processes.
The experimentally determined full width at half maximum of cluster plasmon resonances often shows a $(1/R)$ dependence, which can be denoted as

$$\Gamma_{\mathrm{exp}}\left(R\right) = \Gamma_0 + a/R\,, \tag{2.32}$$

with the bulk limit case $\Gamma_0 = \lim_{R\longrightarrow\infty}\Gamma(R)$ and slope parameter a, which strongly depends on the surrounding matrix. For realistic metals the slope parameter a becomes

$$a = \frac{2v_F\omega_p^2/\omega_1^3}{\left|\left(\frac{d\epsilon_1}{d\omega}\big|_{\omega_1}\right)\right|}\cdot A\,, \tag{2.33}$$

where v_F denotes the Fermi velocity and A is the parameter of the free path effect.
Generally, the prefactor of A depends on ω_1 and thus, on the dielectric constant ϵ_m of the surrounding material. But it is not only ϵ_m, which influences the width of the plasmon resonance. At cluster/matrix interfaces an energy transfer can occur, which is a result of temporary charge-transfer-reactions [Höv93]. This effect, which shows similarities to the interpretation of the chemical contribution to surface enhanced Raman-scattering [Ott91], can be explained with a transfer of excited electrons into matrix-cluster-interface energy states, when they collide with the surface. Thus, a disturbance of the collective oscillation of the electrons in the conductance band may occur [Per93].
The chemical interface damping can alter the position of the plasmon resonance as well as the full width at half maximum depending on the size of the cluster. An external field $\Phi(\vec{r}) = -E_0 z$ in quasi-static approximation with $\vec{r}$ in spherical coordinates (r,θ,ϕ) becomes

$$\Phi\left(\vec{r}\right) = -\left(1 - \frac{R^3}{r^3}\frac{\widetilde{\epsilon}-\epsilon_m}{\widetilde{\epsilon}+2\epsilon_m}\right) rE_0\cos\theta \quad \text{for } r > R\,, \tag{2.34}$$

$$\Phi\left(\vec{r}\right) = -\frac{3\epsilon_m}{\widetilde{\epsilon}+2\epsilon_m} rE_0\cos\theta \quad \text{for } r < R\,. \tag{2.35}$$

The modified dielectric function $\widetilde{\epsilon}$ with correction $\chi^s(\omega) = \chi_1^s(\omega) + i\chi_2^s(\omega)$ induced by the interface holds

$$\widetilde{\epsilon}(\omega) = \epsilon^{\mathrm{cluster}}(\omega) + \chi^s(\omega)\,. \tag{2.36}$$

The power P absorbed by the cluster from an external electric field

$$\vec{E}(t) = \frac{1}{2}\vec{E}_0 e^{-i\omega t} + c.c. \tag{2.37}$$

in the quasi-static approximation denotes as

$$P = P_{\text{cluster}} + P_s = \frac{9}{2}\epsilon_0 \omega \epsilon_m^2 V_0 \frac{\left|\vec{E}_0\right|^2}{\left|\widetilde{\epsilon}(\omega) + 2\epsilon_m\right|^2} \left[\epsilon_2^{\text{cluster}}(\omega) + \chi_2^s(\omega)\right] . \tag{2.38}$$

The power, which is absorbed additionally parallel to the interface $P_\parallel$ with N evenly distributed adsorbate molecules becomes

$$P_\parallel = \frac{1}{3} N M \frac{\epsilon_0^2 \omega_p^4}{n^2 e^2 \omega^2} \left|\frac{3\epsilon_m}{\widetilde{\epsilon}(\omega) + 2\epsilon_m}\right|^2 \left|\vec{E}_0\right|^2 \cdot \text{Re}\{\eta(\omega)\} , \tag{2.39}$$

with the complex friction coefficient $\eta(\omega)$, the mass of the adsorbate molecule M and the electron density n. The component of the additionally absorbed power perpendicular to the interface $P_\perp$ can be written as

$$P_\perp = \frac{N}{6}\epsilon_0 \epsilon_m \omega \left|\frac{3\widetilde{\epsilon}(\omega)}{\widetilde{\epsilon}(\omega) + 2\epsilon_m}\right|^2 \left|\vec{E}_0\right|^2 \cdot \text{Im}\{\alpha_\perp(\omega)\} \tag{2.40}$$

with the polarizability of the adsorbate $\alpha_\perp$. The absorbed power $P_\parallel$ and $P_\perp$ can be described with $\chi_2^\parallel(\omega)$ and $\chi_2^\perp(\omega)$, respectively, which contribute to $\chi_2^s(\omega) = \chi_2^\parallel(\omega) + \chi_2^\perp(\omega)$ in equation (2.38). For more details the reader shall be referred to [Per93, Höv93, Höv95].

2.2.6 Absorption of ellipsoidal silver clusters

All of the afore presented theories consider the metal clusters spherical, which is in good agreement with the form of free metal clusters in vacuum. As soon as the clusters are deposited with high velocity onto a substrate or into a matrix the clusters are deformed. A second influence on cluster form is a change in the interface energy due to the contact to the substrate. The result is a partially flattened ellipsoid, which is depicted in figure 2.12. In quasi-static approximation the dipole moment $\vec{p}$ for an ellipsoid with the three semiaxes

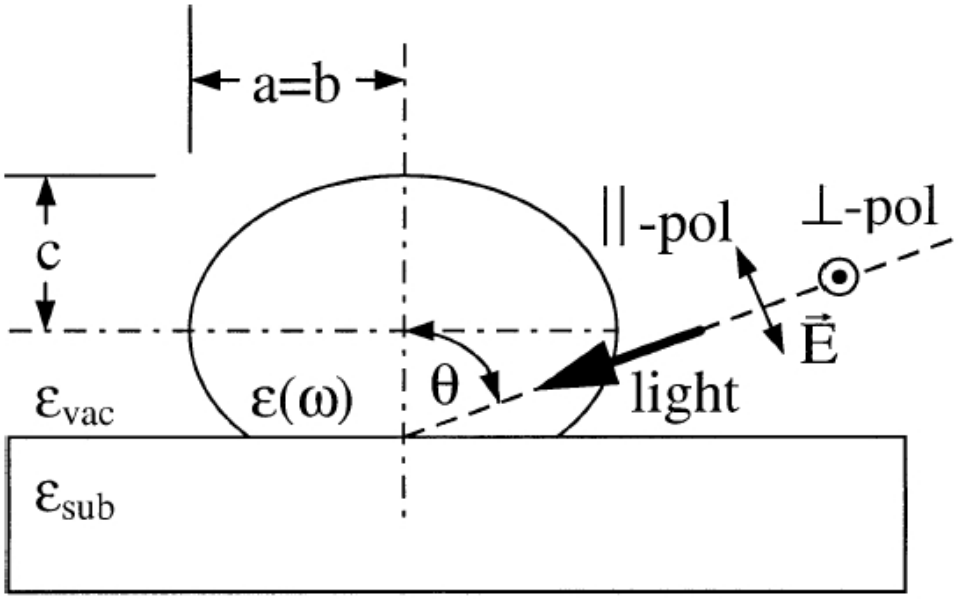

Figure 2.12: Truncated spherical cluster on a substrate. Depicted is the geometry of optical extinction measurements with polarized light and oblique incidence to determine the cluster form. a, b, c denote the semiaxes of the ellipsoid, $\epsilon_{\text{vac}}, \epsilon_{\text{sub}}$ are the dielectric constants of vacuum and substrate, respectively. θ describes the incident angle, $\vec{E}$ is the electrical field vector parallel ($\|$) and perpendicular ($\perp$) to the incident plane [Höv97].

a, b, c in x, y, z direction, respectively, holds

$$\vec{p} = \begin{pmatrix} p_x \\ p_y \\ p_z \end{pmatrix} = \epsilon_0 \epsilon_m \begin{pmatrix} \alpha_1 & 0 & 0 \\ 0 & \alpha_2 & 0 \\ 0 & 0 & \alpha_3 \end{pmatrix} \begin{pmatrix} E_{0x} \\ E_{0y} \\ E_{0z} \end{pmatrix} , \tag{2.41}$$

with the incident electric field $\vec{E}_0$ [Boh83]. For an oblate ellipsoid, for which $a = b > c$, the polarizabilities $\alpha_1, \alpha_2, \alpha_3$ in directions of the semiaxes become

$$\alpha_i = 4\pi abc \frac{\epsilon - \epsilon_m}{3\epsilon_m + 3L_i(\epsilon - \epsilon_m)} , \quad i \in \{1, 2, 3\} . \tag{2.42}$$

The geometry factors L_i, for which

$$L_1 + L_2 + L_3 = 1 , \tag{2.43}$$

can be written as

$$\begin{aligned} L_1 = L_2 &= \frac{g(e)}{2e^2}\left[\frac{\pi}{2} - \arctan g(e)\right] - \frac{g^2(e)}{2} \\ \text{with} \quad g(e) &= \left(\frac{1-e^2}{e^2}\right)^{1/2} \quad \text{and} \quad e^2 = 1 - \frac{c^2}{a^2} \\ L_3 &= 1 - 2L_1 \,. \end{aligned} \tag{2.44}$$

For the electric field vector $\vec{E}_0$ parallel to one of the three semiaxes the extinction cross-section holds

$$\sigma_i = \frac{1}{L_i^2}\frac{\omega}{c_0}\epsilon_m^{3/2} V_0 \frac{\epsilon_2(\omega)}{\left[\epsilon_1(\omega) + (1/L_i - 1)\,\epsilon_m\right]^2 + \epsilon_2^2(\omega)} \,, \tag{2.45}$$

with $V_0 = (4/3)\,\pi abc$ the volume of the ellipsoid and c_0 the vacuum light velocity. This equation is not very precise since the dielectric function of the surrounding material ϵ_m is different for the part of the cluster in contact with the substrate from the rest of the cluster surface. For an isotrope effective dielectric function ϵ_m, which can be found with

$$\epsilon_m = x \cdot \epsilon_{\text{sub}} + (1-x)\,\epsilon_{\text{vac}} \,, \tag{2.46}$$

the absorption of an ellipsoidal cluster can be explained with the quasi-static approximation of the Mie-Gans-Theory [Gan12] (see eq. (2.45)). The parameter x can vary from $x = 0\% - 100\%$, where $x = 0\%$ corresponds to a free cluster in vacuum and $x = 100\%$ corresponds to a cluster embedded in a matrix.

In a second step of the determination of optical properties of ellipsoidal clusters a consideration introduced by Yamaguchi et al. will be taken into account [Yam74]. In this model the influence of the substrate on the polarizability of a cluster can be found by construction of a mirror dipole, which is positioned in the half space behind the substrate. Generally, the dipole moment P of non-interacting particles is linked to the polarizability α with $\vec{P} = \epsilon_0 \epsilon_m \overleftrightarrow{\alpha}\vec{E}$. The cluster dipole moment can be extended with the mirror dipole moment P^*:

$$P^* = \frac{\epsilon_{\text{sub}} - 1}{\epsilon_{\text{sub}} + 1} P \,. \tag{2.47}$$

An external local electric field at the position of the cluster [Höv95] (see section 2.2.5) is enforced by the field contribution of the mirror dipole, which can be denoted as

$$E_{\parallel}^* = \frac{1}{4\pi\epsilon_0 l^3} P^* = \frac{1}{4\pi\epsilon_0 l^3}\frac{\epsilon_{\text{sub}} - 1}{\epsilon_{\text{sub}} + 1} P \,, \tag{2.48}$$

$$E_{\perp}^* = \frac{2}{4\pi\epsilon_0 l^3} P^* = \frac{2}{4\pi\epsilon_0 l^3}\frac{\epsilon_{\text{sub}} - 1}{\epsilon_{\text{sub}} + 1} P \,, \tag{2.49}$$

where l is the distance between P and P^* and ϵ_0 is the permittivity of the vacuum. For ellipsoidal clusters l accounts for $l \leq 2R_{\text{cluster}}$ or $l \approx 2 \cdot c$ with the semiaxis c. An additional flattening of the rotational oblate ellipsoidal cluster at the area of contact to the substrate can be included by decreasing l.

Not only the mirror dipole influences the position of the plasmon resonance but also, for high filling factors, the beginning electromagnetic coupling of the neighboring clusters. This can be accounted for by constructing another mirror dipole P^{**}. With next neighbor distances much bigger than l (figure 2.13) the mirror dipole moments for a certain cluster j become

$$P^{**}_{j,\parallel} = P_{j,\parallel} - P^{*}_{j,\parallel} = \frac{2}{\epsilon_{\text{sub}} + 1} P_{j,\parallel} \,, \tag{2.50}$$

$$P^{**}_{j,\perp} = P_{j,\perp} - p^{*}_{j,\perp} = \frac{2\epsilon_{\text{sub}}}{\epsilon_{\text{sub}} + 1} P_{j,\perp} \,. \tag{2.51}$$

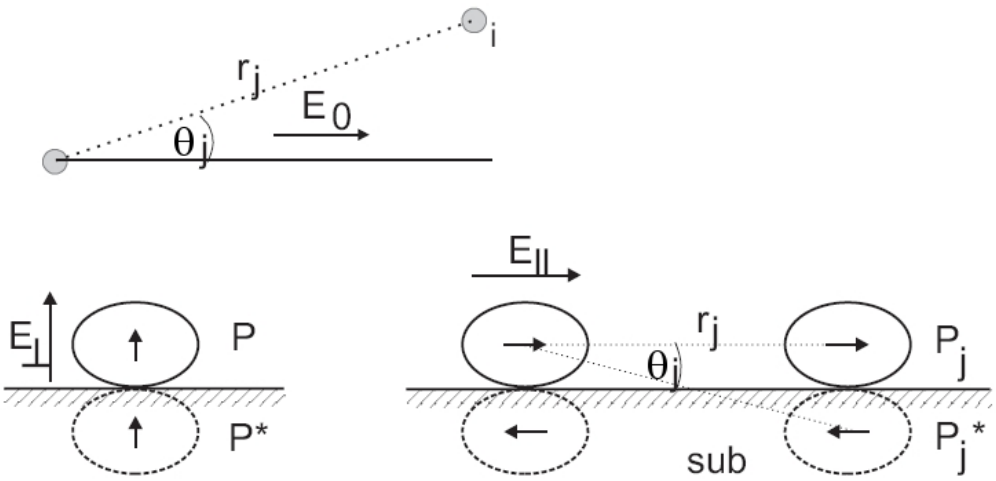

Figure 2.13: Top: Definition of the coordinates r_j and θ_j, bottom: Interaction of the cluster with its mirror dipole in the substrate and neighboring clusters. Picture taken from [Hil01].

The effective electric field of the jth cluster at the position of the cluster with the angle θ_j between the clusters position vector and the electric field in cylindrical coordinates r_j, θ_j holds

$$E^{**}_{\parallel} = -\frac{1}{4\pi\epsilon_0} \frac{2}{\epsilon_{\text{sub}} + 1} \sum_j \frac{1 - 3\cos^2\theta_j}{r_j^3} P_{j,\parallel} \,, \tag{2.52}$$

$$E^{**}_{\perp} = -\frac{1}{4\pi\epsilon_0} \frac{2\epsilon_{\text{sub}}}{\epsilon_{\text{sub}} + 1} \sum_j \frac{1}{r_j^3} P_{j,\perp} \,. \tag{2.53}$$

Thus, the electric field becomes

$$\vec{E} = \vec{E}_0 + \vec{E}^{*} + \vec{E}^{**} \,. \tag{2.54}$$

Changes in the plasmon resonance due to formation of aggregates of single silver clusters and particularly the electromagnetic coupling between the clusters have been investigated

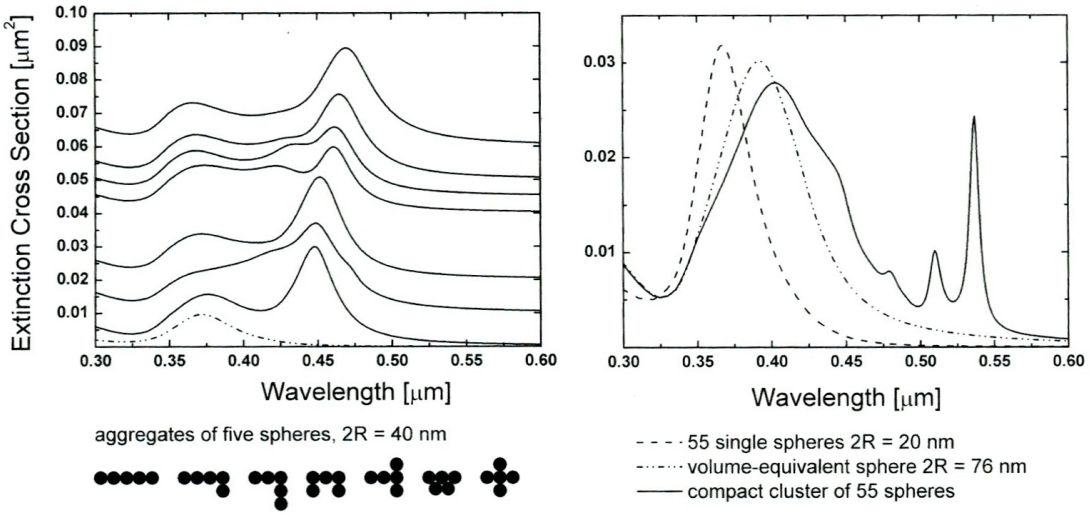

Figure 2.14: Left: Calculated extinction cross-section spectra of aggregates with 5 identical silver spheres of 2R=40 nm, right: Calculated extinction cross-section spectra of an icosadeltahedral aggregate of 55 spherical silver clusters with 2R=20 nm compared to the volume-equivalent sphere with $2R_{ev}$=76 nm [Qui11].

for many years. Quinten uses a generalized Mie theory to determine the optical properties of clusters with interparticle space less than five times the radius of the cluster [Qui11]. Figure 2.14 shows the extinction spectra calculated for aggregates of five spherical silver clusters in different arrangements and the calculated extinction spectra of 55 single silver clusters with 2R=20 nm compared to a volume-equivalent sphere and a compact cluster consisting of 55 spheres.
Directly visible is the fact that the different arrangements of the five silver clusters show significant alterations in the extinction cross-section spectra compared to a single silver cluster extinction. Changes in the coordination of the silver spheres yield not only a red shift in the plasmon energy but also the formation of multiple peaks. These new resonances mainly occur at lower photon energies since the interband transitions prevent formation of resonances in higher energy regions [Qui11]. The largest peak splitting occurs for chain-like silver structures.
The comparison of the extinction cross-section of single silver clusters and an aggregate of 55 silver clusters in the form of an icosadeltahedron shows multiple additional resonances in lower energy regions.

2.2.7 The extinction cross-section and the measurand extinction

The interactions of an electromagnetic wave ($\omega_{\text{response}} = \omega_{\text{incidence}}$) with a cluster define the extinction cross-section σ_{ext} (eq. 2.23). With the absorbed power P_{abs} and the scattered power P_{sca} normalized on the incident intensity I_0 the extinction cross-section holds

$$\sigma_{\text{ext}} = \sigma_{\text{abs}} + \sigma_{\text{sca}} = \frac{P_{\text{abs}}}{I_0} + \frac{P_{\text{sca}}}{I_0} \,. \tag{2.55}$$

This cross-section denotes the single cluster extinction, which in realistic experimental conditions can not be determined. For clusters with next neighbor distances $r_{\text{NN}} > 5R$ with the cluster radius R the intensity $I(x)$ can be written as (Lambert-Beer's law)

$$I(x) = I_0 \exp\left(-n_{\text{cluster}} \cdot \sigma_{\text{ext}} \cdot d\right) , \tag{2.56}$$

with a cluster density n_{cluster} in a sample with thickness d. A suitable measurand to determine the optical cluster properties is the so called extinction, which holds

$$\text{extinction} \equiv -\lg \frac{I}{I_0} \,, \tag{2.57}$$

where I_0 can be determined by measuring the pure substrate as a reference before cluster deposition. Thus, with $I_0 = I(0)$ and $I = I(d)$

$$\text{extinction} = \frac{1}{\ln 10} n_{\text{cluster}} \cdot d \cdot \sigma_{ext} \,, \tag{2.58}$$

the measurand extinction and the extinction cross-section σ_{ext} are identical except for a prefactor. To avoid electromagnetic coupling and beginning coalescence, for which the here shown single cluster extinction does not hold, the effective cluster film thickness for a 2-dimensional hexagonal close packing has to obey $d_{\text{eff}} < 0.19 \cdot R$, resulting from $r_{\text{NN}} > 5R$.

2.3 Theoretical approach to inelastic x-ray scattering

This chapter gives a short overview of inelastic x-ray scattering (IXS), for which the double differential scattering cross-section (DDSCS) will be derived from the principle of x-rays interacting with matter. Further on, the theory is refined for the resonant case (RIXS), which is especially suited to investigate electronic excitations. Regarding experimental methods, RIXS allows one to measure x-ray absorption edges in fluorescence yield. The subsequent section focuses on an approach to calculate ab-initio the cross-section for a RIXS experiment. This whole chapter is based on the theoretical description formulated by Sahle [Sah11] and thus, following Schülke [Sch07].

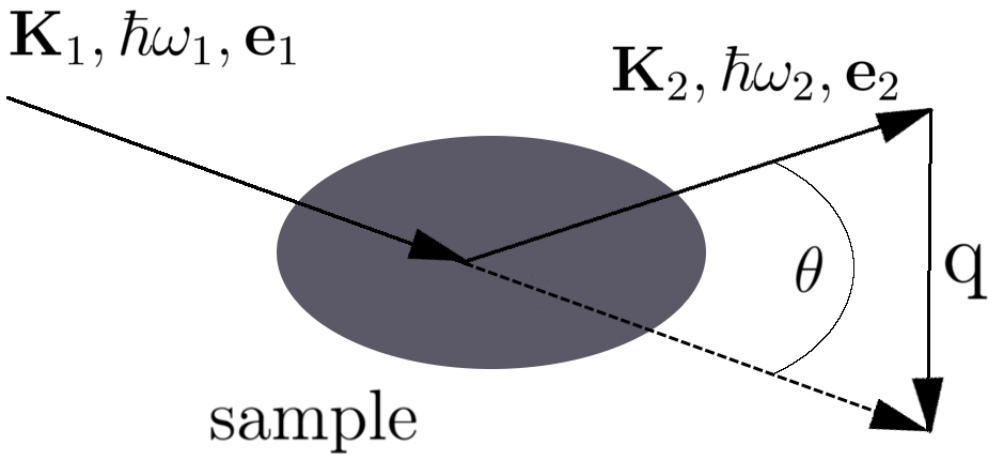

Figure 2.15: Scheme of a typical x-ray scattering event. X-rays with wave vector $\mathbf{K}_1$, energy $\hbar\omega_1$ and polarization vector $\mathbf{e}_1$ are scattered by the sample resulting in wave vector $\mathbf{K}_2$, energy $\hbar\omega_2$ and polarization vector $\mathbf{e}_2$. The energy $\hbar\omega = \hbar\omega_1 - \hbar\omega_2$ and the momentum $\hbar\mathbf{q}$=$\hbar\mathbf{K}_1$-$\hbar\mathbf{K}_2$ are transferred to the scattering system.

2.3.1 Double differential scattering cross-section

In a typical inelastic scattering experiment a photon of energy $\hbar\omega_1$, wave vector $\mathbf{K}_1$ and polarization (unit) vector $\mathbf{e}_1$ impinges upon a target, where it is scattered under an angle θ into a photon of energy $\hbar\omega_2$, wave vector $\mathbf{K}_2$ and polarization vector $\mathbf{e}_2$. It excites the target from an initial state $|\mathrm{i}\rangle$ with initial energy E_i to a final state $|\mathrm{f}\rangle$ with final energy E_f. Following energy conservation with

$$\hbar\omega = E_\mathrm{f} - E_\mathrm{i}\,, \tag{2.59}$$

the energy $\hbar\omega \equiv \hbar\left(\omega_1 - \omega_2\right)$ as well as the momentum $\hbar\mathbf{q} \equiv \hbar\left(\mathbf{K}_1 - \mathbf{K}_2\right)$ are transferred to the target [Sch07].
In a typical inelastic x-ray scattering experiment the DDSCS is measured at a solid angle element $\mathrm{d}\Omega_2$ of the scattering beam as a function of $\mathbf{q}$ and ω:

$$\frac{\mathrm{d}^2\sigma}{\mathrm{d}\Omega_2 \mathrm{d}\hbar\omega_2} \equiv \frac{\begin{array}{c}\text{current of photons scattered into the solid angle element}\\ [\Omega_2, \Omega_2 + \mathrm{d}\Omega_2] \text{ and into the range of energy } [\hbar\omega_2, \hbar\omega_2 + \mathrm{d}\hbar\omega_2]\end{array}}{\text{current density of the incident photons} \times \mathrm{d}\Omega_2 \times \mathrm{d}\hbar\omega_2}\,. \tag{2.60}$$

Following Blume [Blu85] and thus Schülke [Sch07], the DDSCS will be derived from basic principles of the interaction of x-rays with matter. The nonrelativistic Hamiltonian for a system of j electrons in a quantized electromagnetic field up to the order of (v/c) is given by:

$$\begin{aligned}\mathbf{H} = &\frac{1}{2m}\sum_\mathrm{j}\left(\mathbf{p}_\mathrm{j} - \frac{e}{c}\mathbf{A}\left(\mathbf{r}_\mathrm{j}\right)\right)^2 + \sum_{\mathrm{jj'}}\mathbf{V}\left(\mathbf{r}_{\mathrm{jj'}}\right)\\ &- \frac{e\hbar}{2mc}\sum_\mathrm{j}\sigma_\mathrm{j}\cdot\nabla\times\mathbf{A}\left(\mathbf{r}_\mathrm{j}\right) - \frac{e\hbar}{4m^2c^2}\sum_\mathrm{j}\sigma_\mathrm{j}\cdot\mathbf{E}\left(\mathbf{r}_\mathrm{j}\right)\times\left[\mathbf{p}_\mathrm{j} - \frac{e}{c}\mathbf{A}\left(\mathbf{r}_\mathrm{j}\right)\right]\\ &+ \sum_{\mathbf{K}\lambda}\hbar\omega_\mathbf{K}\left[c^+\left(\mathbf{K}\lambda\right)c\left(\mathbf{K}\lambda\right) + \frac{1}{2}\right]\,,\end{aligned} \tag{2.61}$$

with the electron mass m, the elementary electric charge e, and the speed of light c. σ denotes the Pauli spin matrices and $c^+\left(\mathbf{K}\lambda\right)$ and $c\left(\mathbf{K}\lambda\right)$ are the creation and annihilation operator of the quantized electromagnetic field, respectively. The first term in (2.61) accounts for the kinetic interaction of the electrons in a present electromagnetic field. Here, $\mathbf{p}_\mathrm{j}$ is the momentum operator of the jth electron and $\mathbf{A}\left(\mathbf{r}_\mathrm{j}\right)$ the operator of the vector potential of the electromagnetic field at position $\mathbf{r}_\mathrm{j}$ of the jth electron. The second term describes the potential energy of the interacting electron system and the third and fourth term describe the potential energy of the magnetic moment as well as its connection with the electrons' spin in the magnetic field of radiation $(\nabla\times\mathbf{A})$ and with $(1/c)\left(\mathbf{v}\times\mathbf{E}\right)$, respectively.
In this thesis the magnetic structure of matter is of no further interest. Therefore, the terms of the Hamiltonian containing the vector potential $\mathbf{A}$ as well as the Pauli matrices σ, i.e. the spin dependent terms, will be omitted. The last term of equation (2.61) describes the energy of the photon field, namely a summation over all modes of the photon field with wave vector $\mathbf{K}$ and polarization directions λ. After carrying out the square in the first

term of (2.61) and introducing $\mathbf{E} = -\nabla\phi - 1/c\dot{\mathbf{A}}$ with the Coulomb potential ϕ, one can isolate terms describing the interaction between the photon field and the electron. They will further on be treated as a small perturbation within perturbation theory and contain the vector potential explicitly:

$$H_1 = \frac{e^2}{2mc^2} \sum_{\mathrm{j}} \mathbf{A}^2 (\mathbf{r}_\mathrm{j}) \tag{2.62}$$

$$H_2 = -\frac{e}{mc} \sum_{\mathrm{j}} \mathbf{A} (\mathbf{r}_\mathrm{j}) \cdot \mathbf{p}_\mathrm{j} \, . \tag{2.63}$$

Using Fermi's golden rule for the here present scattering processes of one and two photons, the DDSCS is given by

$$\frac{\mathrm{d}^2\sigma}{\mathrm{d}\Omega_2 \mathrm{d}\hbar\omega_2} \propto \frac{2\pi}{\hbar} \left| \langle \mathrm{f} | H_1 | \mathrm{i} \rangle + \sum_{\mathrm{n}} \frac{\langle \mathrm{f} | H_2 | \mathrm{n} \rangle \langle \mathrm{n} | H_2 | \mathrm{i} \rangle}{E_\mathrm{i} - E_\mathrm{n}} \right|^2 \delta (E_\mathrm{i} - E_\mathrm{f}) \, . \tag{2.64}$$

Eq. (2.64) describes two possible excitations: the initial state $|\mathrm{i}\rangle$ can either be excited directly into the final state $|\mathrm{f}\rangle$ or via an intermediate state $|\mathrm{n}\rangle$. The case for resonant inelastic scattering will be described in detail in the next section.

2.3.2 X-ray absorption and resonant case

Resonant inelastic x-ray scattering (RIXS) occurs if the energy of the incident photon $\hbar\omega_1 \approx E_\mathrm{n} - E_\mathrm{i}$. In this case, in the evaluation of (2.64) terms with the resonance denominator $E_\mathrm{i} - E_\mathrm{n} - \hbar\omega_i$ become the dominant contribution and the DDSCS can be written as

$$\frac{\mathrm{d}^2\sigma}{\mathrm{d}\Omega_2 \mathrm{d}\hbar\omega_2} = \left(\frac{r_0}{m}\right)^2 \left(\frac{\omega_2}{\omega_1}\right) \sum_\mathrm{f} \sum_\mathrm{jj'} \sum_\mathrm{n} \left| \frac{\left\langle \mathrm{f} \left| \mathbf{e}_2^* \cdot \mathbf{p}_\mathrm{j} \exp\left(-i\mathbf{K}_2 \cdot \mathbf{r}_\mathrm{j}\right) \right| \mathrm{n} \right\rangle \left\langle \mathrm{n} \left| \mathbf{e}_1 \cdot \mathbf{p}_\mathrm{j'} \exp\left(i\mathbf{K}_1 \cdot \mathbf{r}_\mathrm{j'}\right) \right| \mathrm{i} \right\rangle}{E_\mathrm{i} - E_\mathrm{n} + \hbar\omega_1 - i\Gamma_\mathrm{n}/2} \right|^2 \delta\left(E_\mathrm{i} - E_\mathrm{f} + \hbar\omega\right) , \tag{2.65}$$

with the classical electron radius $r_0 = \frac{e^2}{mc^2}$. Equation (2.65) describes a typical x-ray absorption process, in which a tightly bound core level electron is coherently excited from an initial state $|\mathrm{i}\rangle$ into an intermediate state $|\mathrm{n}\rangle$ with finite lifetime. After this short time the electron de-excites into a final state $|\mathrm{f}\rangle$. If the coherence of the excitation and de-excitation processes is neglected, the absorption process can be explained as a single-particle process depicted in figure 2.16.

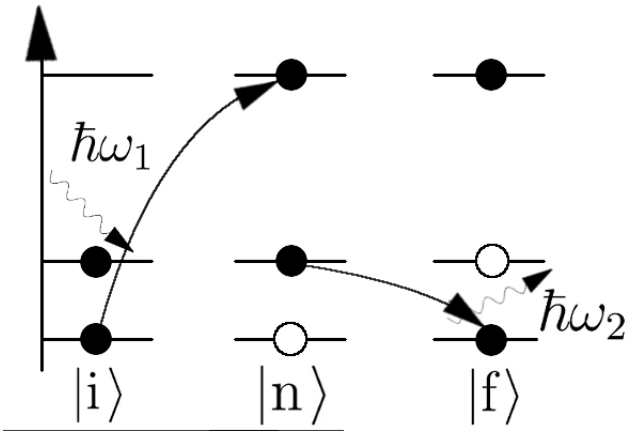

Figure 2.16: Descriptive visualization of the absorption process in the single-particle picture.

At the beginning of the process there is an incident photon $(\mathbf{K}_1, \hbar\omega_1, \mathbf{e}_1)$ and a tightly bound core electron in an initial state ($|\mathrm{i}\rangle$). If the energy of the incident photon is higher than the binding energy of the core level electron, it can be excited into either an unoccupied bound state or a free photo-electron state, depending on the symmetry of the initial state. The intermediate state consists of a hole in a deep core state and an electron in a formerly unoccupied state. Since the intermediate state is not stable, it decays after a finite lifetime into the final state ($|\mathrm{f}\rangle$) by filling the core hole with an electron from a bound state. Due to conservation of angular momentum the excitation and de-excitation have to obey selection rules such as the rules for electric dipole transitions with $\Delta\mathrm{L}{=}\pm1$ for the angular momentum L.
For absorption processes in the hard x-ray regime the decay is radiative, emitting a photon of energy $\hbar\omega_2$, wave vector $\mathbf{K}_2$ and polarization $\mathbf{e}_2$. Here, energy conservation only has to

be satisfied by the whole resonant scattering process. The excitation from the initial to the intermediate state does not have to be strictly energy conserving due to its short lifetime ($\hbar/\Gamma_\mathrm{n}$) [Sch07].
In a RIXS experiment the radiation from the target is analyzed for a range of incident energies to measure the transferred energy $\hbar\omega = \hbar\omega_1 - \hbar\omega_2$. These data can be displayed in a two-dimensional contour plot, the RIXS plane, which shows the recorded intensity versus the incident photon energy in one direction and the energy transfer in the other (figure 2.17).

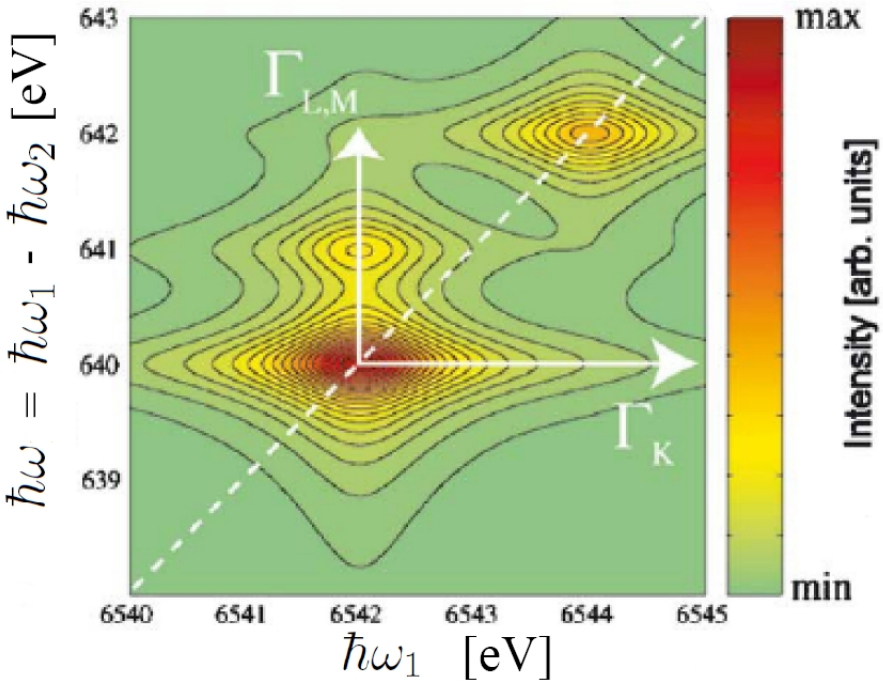

Figure 2.17: Calculated RIXS plane for a process as sketched in Fig. 2.16, Γ_K and $\Gamma_\mathrm{L,M}$ are the lifetime broadening of the K shell core hole and the final state (hole in the L or M shell), respectively. Image taken from [Gla05].

Oftentimes measuring the entire plane is not necessary. Then the intensity of an emission line can be monitored while scanning the energy of the incident photon across an absorption edge. The measured total intensity of the emission line is proportional to the absorption probability of x-rays, thus, it is often called x-ray absorption spectroscopy (XAS). This partial fluorescence yield (PFY) detection of the XAS (PFY-XAS) can be understood as a diagonal cut through the RIXS plane with fixed $\hbar\omega_2$. In PFY the DDSCS reduces to

$$\sigma_\mathrm{PFY} \propto \sum_\mathrm{n} \left|\langle \mathrm{n}\left|T\right|\mathrm{i}\rangle\right|^2 \times \left(\frac{1}{\left(E_\mathrm{i} - E_\mathrm{n} + \hbar\omega_1\right)^2 + \Gamma_\mathrm{n}^2/4}\right)\left(\frac{\Gamma_\mathrm{f}/\pi}{\left(E_\mathrm{n} - E_\mathrm{i} - \hbar\omega_1\right)^2 + \Gamma_\mathrm{f}^2/4}\right), \tag{2.66}$$

with $E_\mathrm{f} + \hbar\omega_2 = E_\mathrm{n}$, thus fixing $\hbar\omega_2$ to the maximum of the fluorescence line. The equation above is a result of replacing the transition operator for excitations in equation (2.65) with T for simplicity and the energy conserving δ-function by a Lorentzian with full width at

half maximum Γ_f to account for the finite lifetime of the final state.
Comparison to the full RIXS equation (2.65) shows that the transition matrix element for the decay $\langle \mathrm{f} \left| T^+ \right| \mathrm{n} \rangle$ is independent of the incident energy and can thus be removed out of the summation over n. Due to the fixed $\hbar\omega_2$ the summation over f can be omitted (only one final state). Since absorption is only possible for suitable unoccupied states $|\mathrm{n}\rangle$, equation (2.66) shows the sensibility of XAS to the unoccupied density of states (uDOS).
To simplify the experimental setup for a XAS experiment even further, the integrated energy over $\hbar\omega_2$ is monitored. In the so called total fluorescence yield (TFY) detection, the probability to excite an electron from an initial to an intermediate state is given by

$$\sigma_\mathrm{TFY}(\omega_1) \propto \sum_\mathrm{n} \left| \langle \mathrm{n} \left| T \right| \mathrm{i} \rangle \right|^2 \frac{(\Gamma_\mathrm{n}/2\pi)}{(E_\mathrm{n} - E_\mathrm{i} - \hbar\omega_1)^2 + \Gamma_\mathrm{n}^2/4} \,, \tag{2.67}$$

with $T = \mathbf{e}_1 \cdot \mathbf{r}$ and after replacing the energy conserving δ-function with a Lorentzian to account for the lifetime of the intermediate state. Although PFY and TFY look very similar, the fact that the lifetime of the intermediate state $\hbar/\Gamma_\mathrm{n}$ is usually smaller than that of the final state $\hbar/\Gamma_\mathrm{f}$, RIXS measurements provide a higher energy resolution than transmission or fluorescence XAS.
Regarding the x-ray absorption as a multiple scattering process yields additional information on the atomic structure of the investigated target [Reh00]. The form of the absorption edge is directly correlated to the surrounding of the absorbing atom. In such an experiment the energy of the incident photon is tuned to measure across a specific absorption edge. As long as the energy $\hbar\omega_1$ is smaller than the binding energy of the core level electron, no absorption occurs. By passing the binding energy, a tightly bound electron can be excited to an unoccupied state. The outgoing photo-electron wave is then backscattered from surrounding atoms causing interference, which modulates the form of the absorption edge. A sketch of such a multiple scattering event is depicted in figure 2.18.

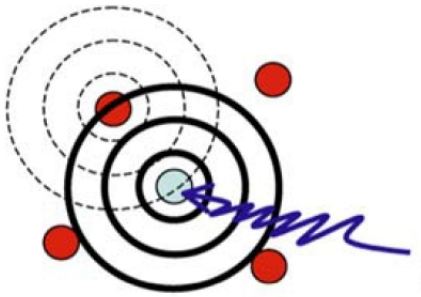

Figure 2.18: Cartoon of an emerging photo-electron wave that scatters off of neighboring atoms. Interference of the emerging and backscattered photo-electron wave modulates the absorption probability. Image taken from [Yan09].

In the region near the absorption edge the kinetic energy of the photo-electrons is small and multiple scattering is strong. The so called XANES region (x-ray absorption near edge structure), which extends to a few 10 eV above the absorption edge is thus sensitive to the shape of the scattering potentials, i.e. coordination chemistry, bond length and bond angles. In the far above region, the so called extended x-ray absorption fine structure (EXAFS), the photo-electrons have higher kinetic energies and single scattering

is dominant. Measurements in the EXAFS region yield information on the next neighbor distances, angles, and coordination numbers [Kon88].

2.4 Oxidation state and unoccupied density of states

Regarding XANES at transition metal L absorption edges, unoccupied states in the d-band yield a pronounced so called "white line" at the absorption edge, which is well known to originate from excitations from a 2p state to md (m=3,4,5) ($L_{2,3}$-edge) [Miy10].
A sketch of these allowed dipole transitions can be found in figure 2.19. The difference between the L_2 and L_3 transitions is the corresponding spin state of the excited electrons, which is J=1/2 and J=3/2, respectively. Since silver has a closed 4d band there is no

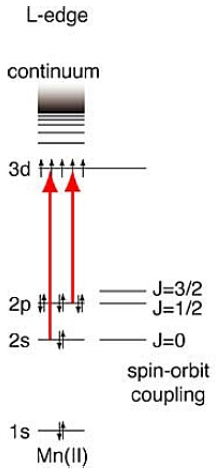

Figure 2.19: Energy level diagram for L-edge (L_1, L_2, L_3) transitions (2s and 2p to 3d) [Yan09]. The L_2 and L_3 transitions differ only in the spin of the excited electron.

significant white line at the Ag L absorption edges. This changes with the oxidation state of silver. For oxidic silver(I) compounds the Ag L_3 spectra exhibit a prominent white line at the rising edge, which can be assigned to transitions from 2p states to final 4d states [Beh92a].
A band structure approach to calculate the XANES spectra for the oxide Ag_2O was used by Czyżyk et al. [Czy89]. Here, the density of states (DOS) was calculated to identify the spectral features of Ag L-edges measured at Ag_2O.
Figure 2.20 shows the split up unoccupied DOS and its tribute to Ag L_1 and L_3 XANES spectra of Ag_2O. Obeying the dipole selection rules the Ag L_1 absorption edge originates from states deriving from p orbitals (allowed 2s→p transitions) while the L_3 spectrum is composed of transitions to s- and d-like orbitals (allowed 2p→s and 2p→d).
As has already been mentioned above it is highly interesting that the closed d-band structure of Ag_2O seems to be broken and unoccupied states occur in the region of the absorption edge (black areas in figure 2.20). This also indicates that Ag 4d states are involved in chemical bonding, which can be explained with a hybridization of the 5s orbital with the $4d_z^2$ orbital as already proposed by Orgel [Org58].
Further investigations on silver oxides with different oxidation states give additional evidence for the existence of the proposed s-d-hybridization [Beh99]. In their presented study of silver compounds with oxidation numbers up to III all investigated compounds show a promoted white line in the onset of the Ag L_3 absorption edge, which can be attributed

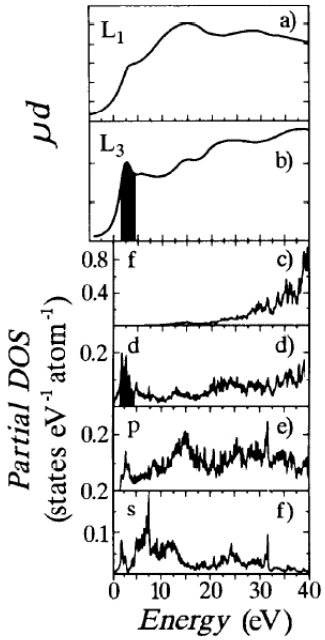

Figure 2.20: Top: XANES spectra of Ag_2O a) Ag L_1 edge, b) Ag L_3 edge. Bottom: Calculated partial density of unoccupied states for Ag_2O with c) f, d) d, e) p, and f) s symmetry (adapted from [Beh92b]).

unambiguously to dipole-allowed $2p_{3/2} \rightarrow$4d transitions. The intensity of the peak rises with increasing oxidation state and degree of covalent bonding and is directly related to the de-occupation of states derived from Ag 4d orbitals.
The Ag L_1 absorption edge measured for different Ag compounds with different oxidation states shifts to higher absorption energies with increasing oxidation number. This is generally interpreted as an increase in ionization energy with increasing positive charge on the atom [Beh99].
Comparison to other transition metals and their oxides such as i.e. copper, which also has a closed-shell configuration ($3d^{10}$) and its oxide Cu_2O shows a similar behaviour [Hul84]. Here also the pure metal copper does not show a white line feature at the $L_{2,3}$ absorption edge while the oxidic compounds such as CuO and Cu_2O do.
Thus, XANES spectra of metal L absorption edges provide suitable information on the oxidation state of the investigated sample and in combination with calculations based on a band structure approach on the partial unoccupied density of states.

2.5 Ab-initio calculations of XAS spectra

The analysis of x-ray absorption spectra is challenging. Especially for measurements of the XANES region the analysis is mostly qualitative by comparison to reference spectra. A more quantitative approach to interpret the data is simulation from first principles. Provided that the computational method gives accurate results, this allows direct access to the structural model of the investigated material. Considering the multiple scattering processes as origin of the fine structure in XAS, a theoretical approach of multiple scattering provides a good basis for ab-initio calculations of XAS spectra. The formalism shown below, which is called real-space multiple scattering (RSMS), is implemented as a routine in the simulation program package FEFF [Reh10]. Introducing the single-particle Green's function G as in

$$(-1/\pi)\,\mathrm{Im}G = \sum_{\mathrm{f}} |\mathrm{f}\rangle\ \langle \mathrm{f}|\,\delta\,(E - E_{\mathrm{f}})\ , \tag{2.68}$$

Fermi's golden rule eq. (2.67) for the case of XAS becomes [Ank98]

$$\sigma\,(E) \propto -\frac{2}{\pi}\mathrm{Im}\,\langle \mathrm{i}\,|\mathbf{e}\cdot\mathbf{r}'G\,(\mathbf{r}',\mathbf{r},E)\,\mathbf{e}\cdot\mathbf{r}|\,\mathrm{i}\rangle\ . \tag{2.69}$$

Since the final state $|\mathrm{f}\rangle$ does not appear in eq. (2.69) the computation is not as challenging as it would be if the final state in the presence of a screened core hole were to be calculated. Calculating final states is very time consuming and can thus only be carried out for small and / or highly symmetrical systems.
The task here is to calculate the one-electron Green's function $G = (E - H + i\Gamma)^{-1}$ with the effective one-electron Hamiltonian $H = H_0 + \sum_n v_n$ and the photo-electron energy E. The Hamiltonian consists of the free electron Hamiltonian H_0 and the sum over the scattering potentials v_n of the surrounding atoms n of the absorbing atom within a cluster of finite size. This accounts for the possibility to use this RSMS formalism to calculate either periodic or aperiodic structures. In the afore mentioned FEFF implementation these potentials are approximated by overlapping muffin-tin potentials, which are calculated self consistently (self consistent field (SCF) method) by iteration of the total electron density, the potential and the Fermi energy [Reh00].
The amplitude for an electron to propagate from a state $|LR\rangle$ into a state $|L'R'\rangle$, with the site R and the angular momentum $L = (l, m)$ can be calculated as

$$G = G^C + G^{SC}\ . \tag{2.70}$$

Here G^C denotes the contribution of the central atom $(-1/\pi)\,\mathrm{Im}G^C = \delta_{R,R'}\delta_{L,L'}$ and G^{SC} describes the scattering from the surrounding atoms, which is given by the functional Dyson equation

$$G^{SC} = G^0tG^0 + G^0tG^0tG^0 + \dots\ , \tag{2.71}$$

using the free propagator G^0 and the scattering matrix t summing up over all single scattering paths (G^0tG^0), the double scattering paths ($G^0tG^0tG^0$), etc. For high energies, i.e. the EXAFS region, this sum usually converges very quickly while for the region, where multiple

scattering is dominating all scattering paths might necessarily have to be included. Thus, the full multiple scattering (FMS) has to be calculated using

$$G^{SC} = \left(1 - G^0 t\right)^{-1} G^0, \tag{2.72}$$

which includes a challenging matrix inversion. Since the mean free path of the photoelectron around the absorption edge is only around 1-5 Å, only relatively small clusters of the order 10^2 have to be taken into account. This will be important for the simulations presented in section 4.4 and particularly for the calculation of larger clusters.

3 Experimental setup and methods

This chapter gives an overview of the preparation process that was used to produce all investigated sample systems as well as a brief introduction of the experimental setups for optical spectroscopy cluster plasmon resonance measurements and XANES measurements. The first section introduces the cluster source with its different chambers and pressure regions followed by a description of the setup for in situ optical transmission spectroscopy measurements of the freshly prepared samples. In the remainder of this chapter the different experimental endstations at synchrotron radiation facilities used for the x-ray absorption near edge spectroscopy measurements performed on the Ag cluster samples will be presented.

3.1 THECLA

All of the samples investigated in the presented experiments were prepared in a THermal CLuster Apparatus (THECLA) [Kre98]. The setup of this vacuum cluster source is depicted in figure 3.1. In the cluster source silver is indirectly heated and vaporized in a graphite oven via a tantalum heater (figure 3.2). By adding argon with a partial pressure of 4.5 bar as an inert carrier gas, which is well known to promote cluster condensation [Hag81, Sch84], the mean free path of the silver atoms becomes very small so that during the acceleration through the supersonic nozzle with the smallest diameter of 0.42 mm and an opening angle of $2\alpha = 10°$ into a region of low pressure numerous collisions take place and cluster condensation starts.
Collisions between silver and argon atoms function to cool the clusters [Hab92] as condensation heat is transferred to the argon atoms. Calculations show that without the addition of the carrier gas metal clusters would be liquid [Gsp86].
Having passed the nozzle, the highly intense cluster beam reaches a heated cone-shaped aperture (namely skimmer), which is suited to cut out the outer regions of the cluster beam, that contain mostly argon atoms. A large amount of the added carrier gas is already pumped in this section before passing the skimmer by the installed roots pump. Leaving the high temperature region of THECLA (approx. 2300 K in the source) the clusters enter the low temperature region where the rest of the argon is pumped by a cryo pump with large copper shields so that only the silver clusters are left over to enter the preparation and measuring chamber.
Having passed the cryo pump, the Ag clusters reach a rotatable aperture, the so called shutter (figure 3.3). By moving the wedge shaped aperture through the cluster beam it is possible to vary the amount of clusters to be deposited on a substrate, which can be installed inside the measuring chamber at one or even both of the depicted sample positions

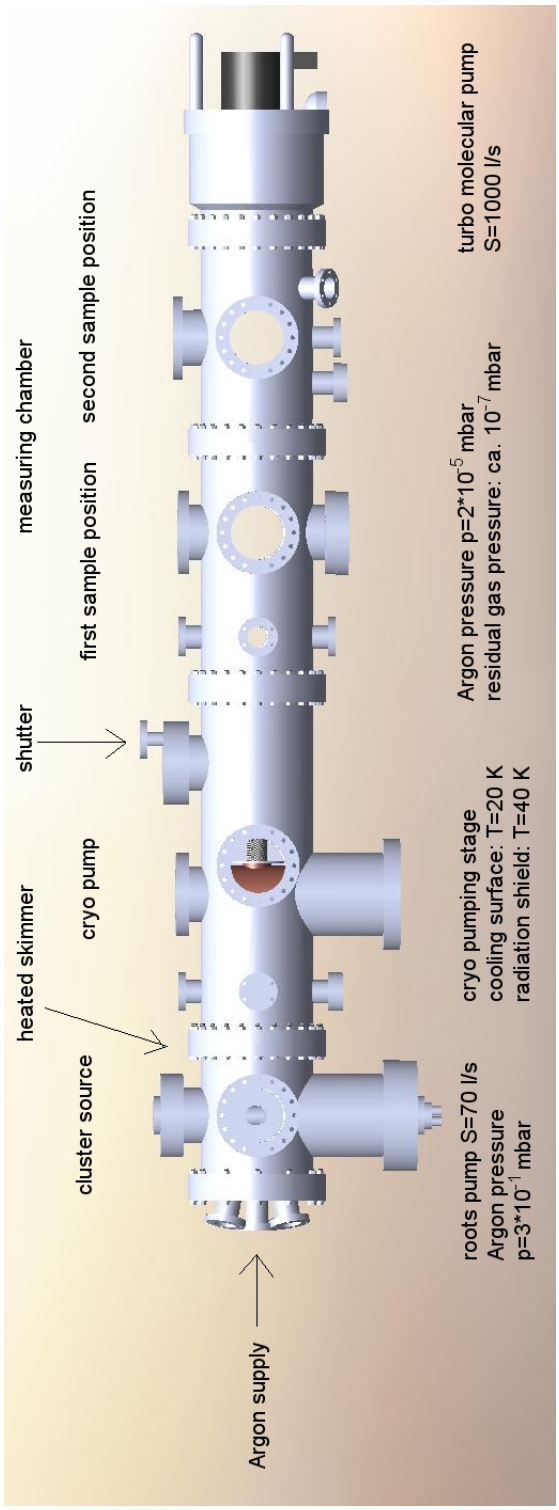

Figure 3.1: Scheme of the THermal CLuster Apparatus (THECLA) used to produce Ag clusters in a supersonic expansion yielding a highly intense cluster beam [Hen09].

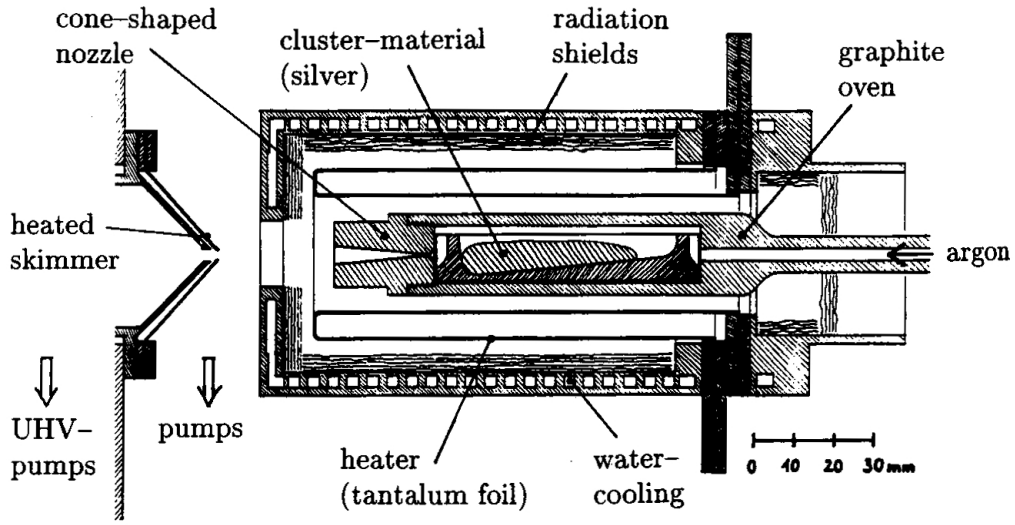

Figure 3.2: Sketch of the cluster source installed in THECLA including the graphite oven and the conical supersonic nozzle [Höv95].

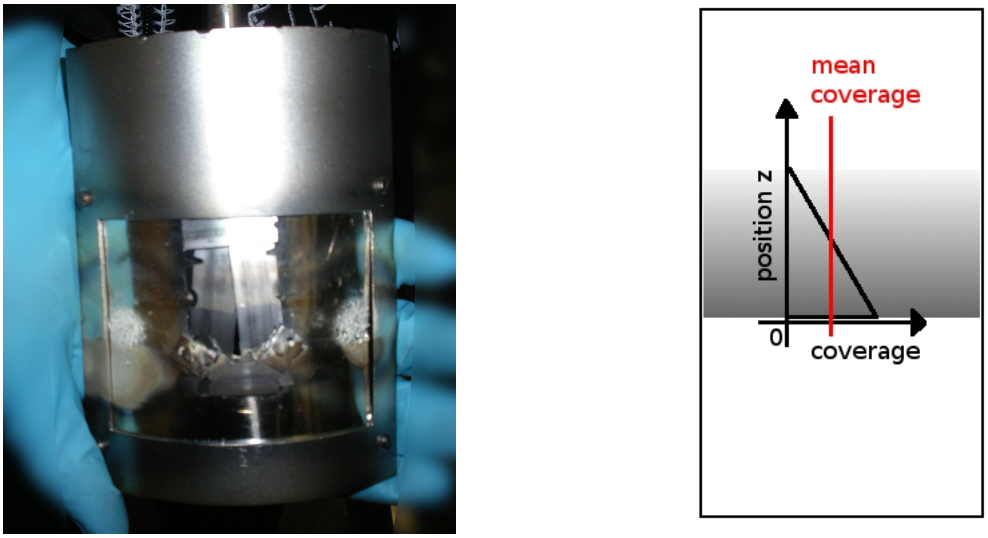

Figure 3.3: Left: Installed wedge shaped aperture in the rotatable shutter, right: Sketch of the deposition spot on a substrate with visible coverage gradient and explanatory sketch of the determination of the cluster coverage relying on the mean coverage as measured with the oscillating crystal.

(figure 3.1).
A sample heater consisting of a water cooled halogen lamp, which can be focused on the sample holder to indirectly heat the substrate prior to deposition, can be installed at the silica glass window of the first sample position [Lat11].
The wedge shaped form of the aperture yields a coverage gradient, which is depicted in figure 3.3. By moving the wedge through the cluster beam deposition time alters with the width of the aperture. The mean deposited amount of clusters can be monitored via an oscillating crystal. Usually, two deposition spots with different mean coverage are deposited onto one substrate. The deposited cluster coverage will further on be denoted as cluster monolayers (ML) with 1 ML $\approx$ 1.2 nm for a hexagonal closed packing of clusters with a mean diameter of 2 nm.

3.2 Optical spectroscopy

After having prepared the cluster samples, measurements of the cluster plasmon resonances are performed in situ using optical absorption spectroscopy. Therefore, the light of a combined halogen and a balanced deep UV deuterium lamp, which provides light in the spectral range from λ =190 nm to 2500 nm (Avantes AvaLight-DH-S-BAL), is focused by a quartz lens through a fused silica window onto the sample inside the vacuum chamber. After having passed the sample, the light is collected by a collimator lens (also fused silica) and guided through a 25 μm slit into a high UV-sensitive back-thinned optical spectrometer (Avantes AvaSpec-2048x14) with a resolution of $\Delta\lambda$ =1.4 nm (see figure 3.4). Since the cluster plasmon resonance of Ag lies in the near UV it is essential to use fused silica glass windows and lenses, which are light-transmissive in the near UV region. Usual window glass is not transmissive in the spectral region of interest. To further enhance the sensitivity of the spectrometer in the near UV region a deep UV coating as well as a UV/VIS collimator lens are installed inside the spectrometer. The transmitted intensity of the light is monitored by the spectrometer with respect to the incident intensity. It is directly correlated to the extinction via equation (2.58). The optical measurements can be used to characterize the samples with respect to the amount of deposited material as well as to the quality of the clusters, i.e. electromagnetic coupling or coalescence. Therefore, the sample is moved in z-direction and spectra are taken in steps of approx. 1 mm to visualize the variation of the cluster coverage with z. The method for approximating the cluster coverage will be explained in section 4.1.

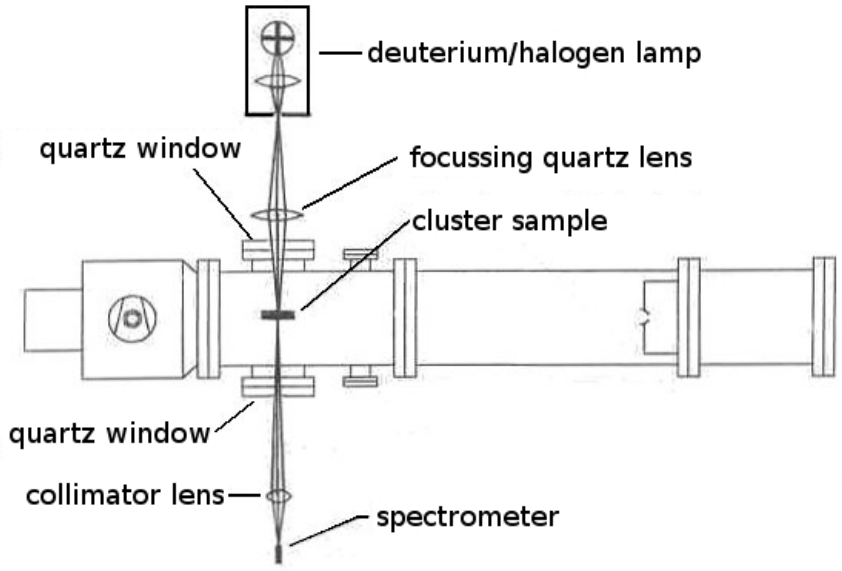

Figure 3.4: Experimental setup for optical absorption spectroscopy of the cluster plasmon resonances.

3.3 X-ray Absorption Near Edges Structure (XANES) spectroscopy

All x-ray absorption spectroscopy experiments were performed in an energy region around 3 keV. Since the prepared cluster samples consist of only small amounts of clusters it is necessary to utilize a highly intense x-ray beam to get a suitable signal to noise ratio. This kind of highly intense x-ray radiation with tunable energy is provided by third generation synchrotron radiation facilities like the Dortmunder Elektronen Speicherring Anlage (DELTA), Dortmund, Germany, and the European Synchrotron Radiation Facility (ESRF), Grenoble, France. In the following subsections the two endstations BL8 at DELTA, Dortmund, and ID26 at ESRF, Grenoble, where the experiments were performed, will be described.

3.3.1 BL8 at DELTA, Dortmund

To investigate the electronic and atomic structure of the pre-characterized cluster samples using XANES spectroscopy, tunable x-ray radiation in the region around the Ag L absorption edges (energies: L_1= 3.805 keV, L_2= 3.524 keV, L_3= 3.351 keV) is needed [Beh99]. The materials science beamline BL8 at the DELTA storage ring, Dortmund, was designed to provide x-ray radiation with a maximum flux of $3{\cdot}10^9$ photons per second in the energy range between 1 keV and 25 keV using the intense radiation emitted by the superconducting 5.3 T asymmetric wiggler [Lüt09]. For achieving the energy range needed for the here presented experiment, a Si(111) monochromator crystal is used.
The monochromatic x-ray beam is then collimated by a slit system and focused by an x-ray mirror to a size of approx. 1×5 mm^2 (vertically $\times$ horizontally) onto the sample, which is installed inside a vacuum chamber. Since the investigated amount of material is small it is necessary to measure the x-ray absorption structure in fluorescence mode. The absorption cross section is proportional to the detected fluorescence via

$$\sigma\left(E\right) \propto \frac{I_\mathrm{f}}{I_0}\,, \tag{3.1}$$

with the incident intensity I_0 and the fluorescence yield I_f. To measure in fluorescence mode the sample is rotated by 45° with respect to the incident beam axis (figure 3.5). At an angle of 90° an Amptek XR-100CR fluorescence detector with an energy resolution of ΔE ≈150 eV is installed to detect the fluorescence radiation emitted by the sample (TFY). The monitor signal is either detected using an ionization chamber or a gold net. The advantage of the Au net is a better signal to noise ratio due to a higher x-ray flux on the sample. With a manipulator in z-direction it is possible to scan positions with different cluster coverage in the deposited cluster spot. At BL8, DELTA, the data for Ag L_3 absorption edges were taken beginning 60 eV below the onset of the absorption edge energy (3.351 keV) and scanning up to 80 eV above the absorption edge onset.

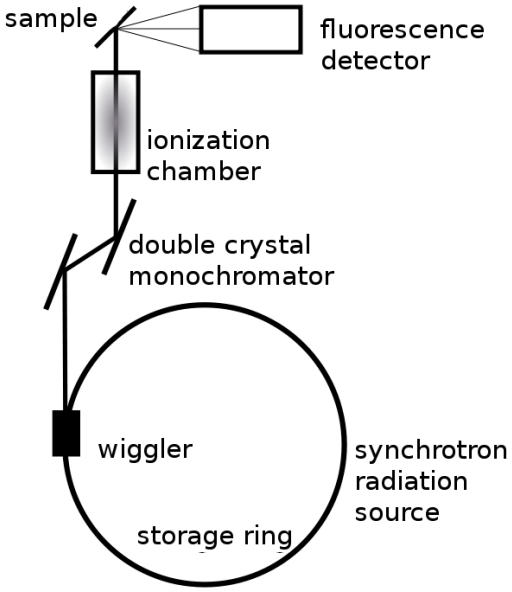

Figure 3.5: Experimental setup for absorption spectroscopy of the Ag L_3 edge used at BL8, DELTA, Dortmund [Sah11].

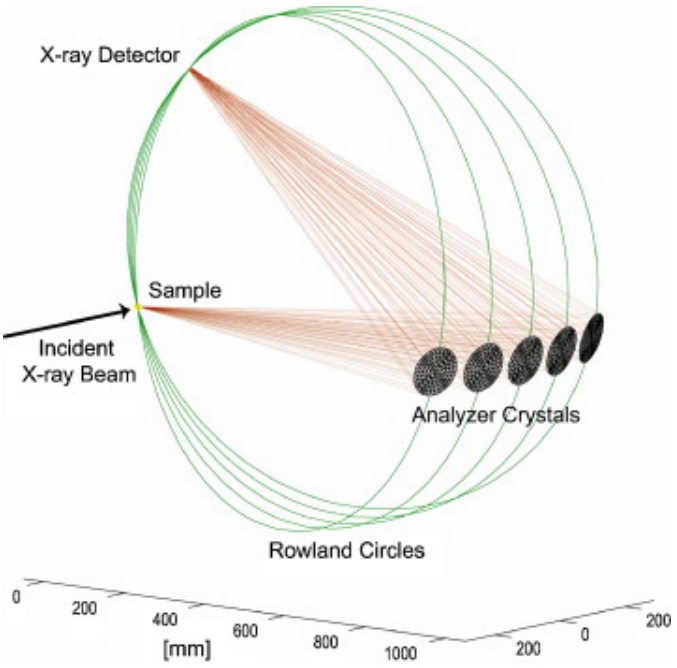

Figure 3.6: 5-analyzer-crystal x-ray emission spectrometer with vertical scattering geometry. Depicted are the focusing Rowland circles [Gla09].

3.3.2 ID26 at ESRF, Grenoble, France

The XAS/XES beamline ID26 at the third generation synchrotron radiation facility ESRF, Grenoble, France, provides synchrotron radiation in the spectral energy range from 2.4-30 keV [Gau99]. The three mechanically independent undulators yield a flux $> 10^{13}$ photons per second at the sample using a Si(111) monochromator. The intensity of the incident monochromatic x-ray beam is determined using an ionization chamber and measuring the photo-ion current. The x-ray beam is focused on the sample at an angle of 45° with respect to the beam axis with a size of approx. 0.15×0.6 mm^2 (vertically $\times$ horizontically). The use of an x-ray emission spectrometer with five analyzer crystals enables an energy resolution of $\Delta E \approx 0.1$ eV (PFY). The analyzers are positioned on a vertical Rowland circle (figure 3.6). Figure 3.7 shows the setup of the experiment with a helium balloon around the analyzer to reduce scattering from air-molecules. To measure the Ag L_1 absorption edge (3.805 keV) the energy was scanned from 3.795-3.882 keV, for the Ag L_2 edge (3.524 keV) the energy range was 3.510-3.600 keV.

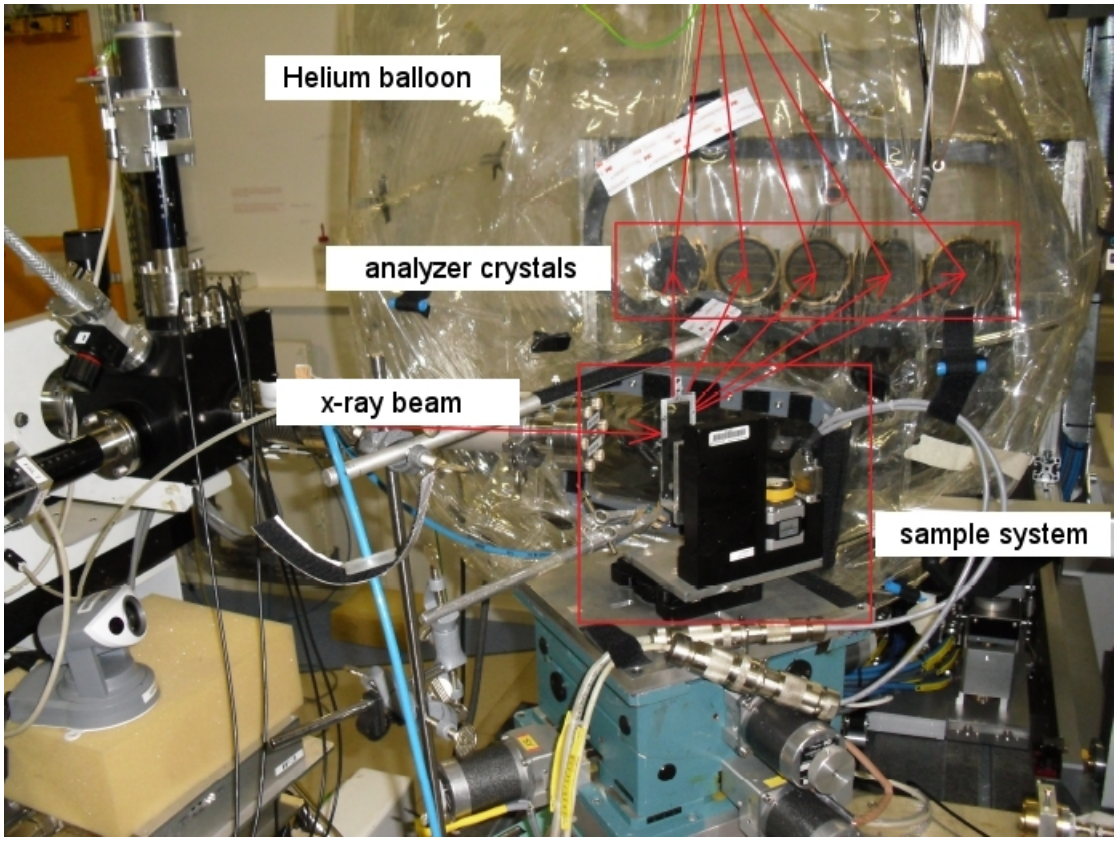

Figure 3.7: Photo of the experimental setup at ID26, ESRF, Grenoble, with the sample system installed and the five-analyzer-crystal x-ray emission spectrometer in a helium balloon to investigate the L absorption edges of Ag clusters in fluorescence mode (PFY).

4 Sample system and results

4.1 Sample system

In the following section the different samples investigated in this work will be described. All of the samples were prepared using the super sonic nozzle expansion in THECLA. The experiments performed on the samples account for the amount of deposited clusters on the surface (SiO_2 silica glass) or in the matrix (polydimethylsiloxane (PDMS) or SiO_2 aerogel). Thus, it is important to determine an approximated coverage gradient for each investigated sample. Therefore, the so called dipole sum rule can be utilized to integrate the surface plasmon resonances with

$$\int_0^\infty \sigma(\omega) d\omega = 2\pi^2 \frac{e^2\hbar^2}{m_e c} \cdot Z \,, \tag{4.1}$$

where ω is the plasmon frequency, m_e is the electron mass and Z is the number of electrons in the collective oscillation and thus, directly correlated to the amount of clusters deposited [Alo05]. By calculating the dipole sums for the data taken in vacuum it is possible to approximate the cluster coverage for the mean deposited amount of clusters, which was determined using an oscillating crystal during the deposition (compare figure 3.3).
Having measured the extinction spectra of the coverage wedge (see figure 3.3) in vacuum the integrated optical absorption is used to determine the cluster coverage corresponding to the extinction measured at a certain position z. Thereby, the absolute scale is directly related to the mean coverage as determined by the oscillating crystal and thus, the coverage at position z can be determined in a linear regression.

4.1.1 Ag clusters on SiO_2 silica glass

The first sample system consists of different Ag cluster deposition spots with varying cluster coverage on silica glass (SiO_2) substrate. Silica glass is especially suited as substrate due to its good transmittance in the near UV region, where the plasmon resonance of silver can be found.
The samples investigated are DO_05 with a coverage gradient of 0.04 - 0.46 cluster monolayers (ML) and a coverage gradient of 0.04 - 0.17 ML (see section 3.1 for definition of ML). The deposition spot with the higher coverage will further on be denoted as "high coverage", the spot with the lower as "low coverage".
The second sample presented is DO_12, which was heated prior to the cluster deposition process to remove possible water monolayers from the substrate. The deposited coverage gradients are 0.01 - 0.95 ML for the high coverage and 0.05 - 0.35 ML for the low

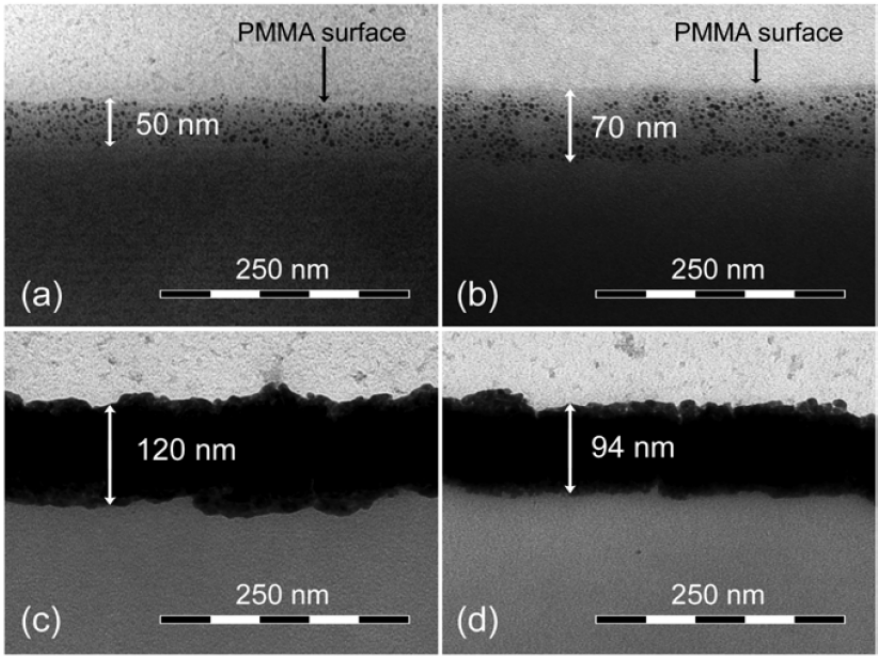

Figure 4.1: TEM micrographs of palladium nanoparticles deposited on PMMA: (a) Nominal film thickness below 1 nm at RT, (b) Nominal film thickness below 1 nm at 95°C, (c) 60 nm nominal film thickness at RT, (d) 50 nm nominal film thickness at 95°C [Rav09].

coverage. For both samples optical spectroscopy measurements were taken directly after the deposition and after venting the vacuum chamber and exposure to air for approx. 60 minutes.

4.1.2 Ag clusters in polydimethylsiloxane (PDMS) on silica glass (SiO_2)

The use of a matrix to embed clusters is a promising approach to achieve a high coverage of clusters, which are clearly separated. Since on a surface the possible amount of deposited clusters to gain information on single cluster properties is limited due to electromagnetic coupling and beginning coalescence two different potential matrix materials were used to prepare samples with significantly more clusters remaining separated.
The ability to deposit clusters into a PDMS film was found by Ravagnan et. al. They produced palladium nanoparticles in a supersonic expansion and deposited them onto poly(methyl methacrylate) (PMMA) [Rav09] and polydimethylsiloxane (PDMS) [Cor11] films to form thin metal layers on the surface. But additionally to the film formation even for the much harder PMMA the clusters penetrated the surface (figure 4.1). The expression nominal film thickness corresponds to the thickness of a film produced with the same amount of palladium nanoparticles deposited on a MgO substrate.
The formation of metal electrodes in PDMS by deposition of palladium nanoparticles into PDMS is shown in [Cor11]. Based on these informations for the second sample system thin PDMS films were produced on SiO_2 silica glass substrates.

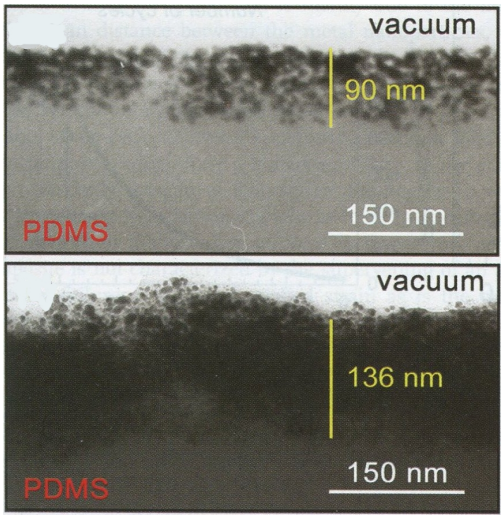

Figure 4.2: TEM images of cross-sections of Au/PDMS nanocomposite samples obtained at room temperature by implanting an equivalent thickness of clusters of 35 nm and 210 nm, respectively [Cor11].

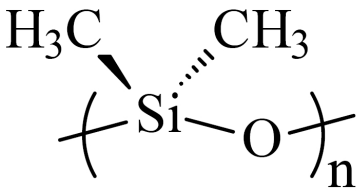

Figure 4.3: Structural unit of PDMS [Rot09]. The here used PDMS matrices are formed by chains of this unit, which are then crosslinked using a curing agent to form a network.

Therefore, the commercial elastomer silicone kit "Sylgard®184" (Dow Corning) was used, which consists of two compounds namely the Base (silicone oil) and the Curing Agent (crosslinker). A 10:1 Base:Curing Agent mixture was diluted with n-Hexane and then spin cast onto the SiO_2 sample holders. With this spin casting method it is possible to produce thin films of a few nanometers up to a few micrometers [Pat06, Lan09].
In the framework of a bachelor's thesis it was possible to determine the thickness of the produced PDMS layers using an interferometry method [Sal11]. The investigated samples DO_10 and DO_11 have PDMS layer thicknesses of (1.2±0.2) μm and (0.5±0.2) μm, respectively.
A descriptive sketch of the structure of PDMS is shown in figure 4.3. The cluster coverage ranges deposited into the PDMS films are 0.18 - 2.24 ML (high coverage) and 0.10 - 0.41 ML (low coverage) for DO_10 and 0.11 - 1.02 ML (high coverage) and 0.04 - 0.21 ML (low coverage) for DO_11, respectively.

4.1.3 Ag clusters in SiO_2 aerogel

Another approach to achieve a large amount of separate clusters is to use a so called aerogel as a matrix, into which the clusters are deposited. An aerogel in general is a highly porous compound that contains up to 99.98% of air per volume. Since the discovery of aerogel in the early 1930s by S.S. Kistler [Kis31] interesting properties were found such as the ultralow thermal conductivity of silica aerogels [Kis34] and different materials were probed such as i.e. inorganic oxides [Tei76], carbon nanotubes [Bry07] or iron [Lev09].
For optical spectroscopy in transmission mode a highly transparent aerogel is needed. Thus, SiO_2 aerogel was chosen as a matrix material. With a dielectric constant of approx. 1.1 at a density of 0.1 g/cm^3 and particle sizes of 2-5 nm as well as pore sizes of 20-50 nm [Law] possible light scattering in the UV/VIS region is smaller than the total extinction. By measuring the pure aerogel sample's extinction before cluster deposition it is possible to later subtract the extinction resulting from the aerogel from the measured cluster sample signal (background correction).
The investigated sample DO_14 was planned to be a direct comparison between clusters of the same coverage deposited on a SiO_2 substrate as well as into a SiO_2 aerogel. Due to a problem during the deposition it was not possible to achieve the same coverage gradient in aerogel as on the SiO_2 substrate. The cluster coverage gradients for DO_14 are 0.81 - 1.74 ML (aerogel) and 0.11 - 2.38 ML (SiO_2 substrate).
As a second aerogel sample two aerogel "drops" were mounted onto a sample holder and two different coverage gradients were deposited. These are for sample DO_15 1.60 - 8.34 ML (high coverage) and 1.07 - 3.93 ML (low coverage), respectively.

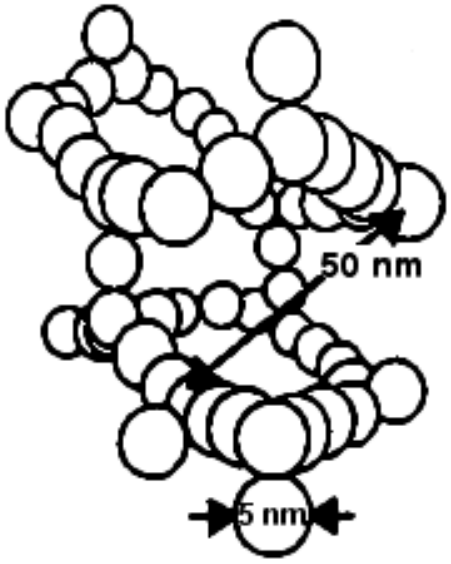

Figure 4.4: Structure of SiO_2 aerogel [Höv95].

4.2 Results - Optical spectroscopy

In the following section the results of the optical spectroscopy measurements will be presented. The outline of a typical optical absorption spectroscopy experiment performed for this thesis is as follows.
Before the sample preparation the extinctions of the empty substrates (SiO_2 silica glass for DO_12 previously heated, PDMS on SiO_2 and SiO_2 aerogel) are measured to be able to subtract the background signal from the cluster signal in the sample measurements. Therefore, the substrates are moved in z-direction through the focused beam of the deuterium-halogen lamp and transmission spectra are taken approx. every 1 mm (compare section 3.2). As reference the pure lamp emission spectrum is taken.
As a first step after the deposition process extinction spectra of the deposition spots are taken in vacuum at the same positions as the background measurements. To achieve a suitable accuracy the z-position is adjusted using a digital caliper with a step width of 0.1 mm. Multiple reference measurements of the lamp emission spectrum are taken and averaged to account for possible thermally induced changes over the measurement period.
After these measurements in vacuum (approx. 10^{-6} mbar) the cryo pump is switched off and warmed up. At a certain temperature of the cryo cold face the carrier gas argon desorbs and has to be pumped away by the remaining pumping stations. To achieve a better thermal conduction inside the vacuum chamber (to accelerate the warm up process) the chamber is subsequently filled with argon up to a few mbar.
At room temperature THECLA is vented with air for approx. 60 minutes. Afterwards, the chamber is pumped again and another data set is taken, which will further on be referred to as "in air" although the actual measurements are taken at a pressure of approx. 10^{-5} mbar. These measurements are of great interest not only with respect to future applications using small noble metal clusters i.e. in miniaturized electric devices, which would then be exposed to air, but particularly for comparison reasons, since the prepared cluster samples are transferred to the synchrotron radiation facilities in air to perform XANES measurements.
Table 4.1 gives an overview of the investigated samples and the important sample properties.

Sample name	Sample system	cluster coverage [ML]	high or low coverage
DO_05	SiO_2	0.04 - 0.46	high
DO_05	SiO_2	0.04 - 0.17	low
DO_10	PDMS	0.18 - 2.24	high
DO_10	PDMS	0.13 - 0.41	low
DO_11	PDMS	0.11 - 1.02	high
DO_11	PDMS	0.04 - 0.21	low
DO_12	SiO_2 heated	0.01 - 0.95	high
DO_12	SiO_2 heated	0.05 - 0.35	low
DO_14	aerogel	0.81 - 1.74	
DO_14	SiO_2	0.11 - 2.38	
DO_15	aerogel	1.60 - 8.34	high
DO_15	aerogel	1.07 - 3.93	low

Table 4.1: Summary of the investigated samples together with information on the used substrate or matrix material and the approximated cluster coverage in cluster monolayers [ML].

4.2.1 Clusters on SiO_2 silica glass

Deposition of noble metal clusters with a mean diameter of approx. 2 nm on the surface of a substrate such as SiO_2 silica glass yields separate almost spherical clusters for coverage <0.1 cluster monolayers. For coverage of approx. 0.1 ML and above, for which the cluster distances are smaller than 5R, the clusters start to couple electromagnetically and for even higher coverage coalescence sets in and the clusters form larger islands. As sketched in figure 4.5 the axial ratio of the clusters $c/a = x$ stays stable for coverage below 0.1 ML. Here c and a denote the short and long semiaxes of a rotational ellipsoid, respectively. Above this limit the clusters start to coalesce yielding a change of the axial ratio $c/a < x$. This is different for metal islands grown by metal evaporation - here the axial ratio continuously varies with coverage [Yos71]. The changing axial ratio can be seen as a shift of the plasmon resonances in the extinction spectra of the clusters. Hubenthal [Hub09] has recently shown that the form and thus the axial ratio of a rotational ellipsoidal cluster on a substrate can be tuned by intense laser irradiation resulting in the shift of the cluster plasmon resonance (figure 4.6).
Figures 4.7 and 4.9 show extinction spectra taken at low coverage of sample DO_05 in vacuum and after 60 minutes exposure to air, respectively. For this lower coverage there is a visible but small red shift of the plasmon resonance energy with increasing coverage. This can be attributed to beginning electromagnetic coupling above 0.1 ML as well as changes in the axial ratio of the clusters. In addition to the coverage dependent shift of the cluster plasmon resonance there is a visible shift to lower energies after exposure to air.
Comparison to the high coverage of DO_05, which is shown in figures 4.8 (vacuum) and 4.10 (after 60 minutes exposure to air) confirms the trend already seen for the low coverage.

Taking a closer look at the position of the maximum energy of the plasmon resonances, there is a clearly visible shift to lower energies with increasing cluster coverage, which has already been reported before for similar experiments [Höv95, Hen09]. Comparison between the two datasets taken at the same sample positions shows an additional shift to lower energies as well as a reduction in the intensity of the cluster plasmon after exposure to air. This shift can be explained with formation of an adsorption layer on the cluster surface, which results in the change of the dielectric function ϵ_m. A different ϵ_m may also lead to changes in the plasmon damping.
Another influence is chemical interface damping, which can occur for interface electronic states of the cluster and an adsorbate [Höv93]. It is also possible that the clusters are slightly deformed by the formation of an adsorbate layer resulting in a change of the axial ratio and thus, in a change of the plasmon resonance energies [Yan92].
For the preparation of the second sample DO_12 with Ag clusters on SiO_2 the silica glass substrate was heated prior to the deposition to desorb possible water monolayers from the surface [Lat11] and then the clusters were deposited as explained before. Figures 4.11 and 4.13 show the extinction spectra for the low coverage in vacuum and after exposure to air, respectively. The measured extinction spectra for the high coverage are shown in figure 4.12 (in vacuum) and in figure 4.14 (after exposure to air). Similar coverage dependent changes in the peak positions are visible as for DO_05.
A comparison between the peak positions of the high and low coverage of DO_05 and

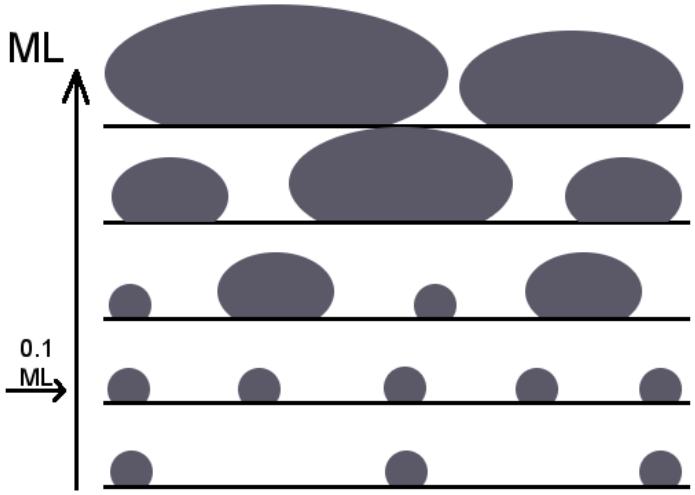

Figure 4.5: Scheme of cluster coalescence, which sets in at a coverage of approx. 0.1 ML.

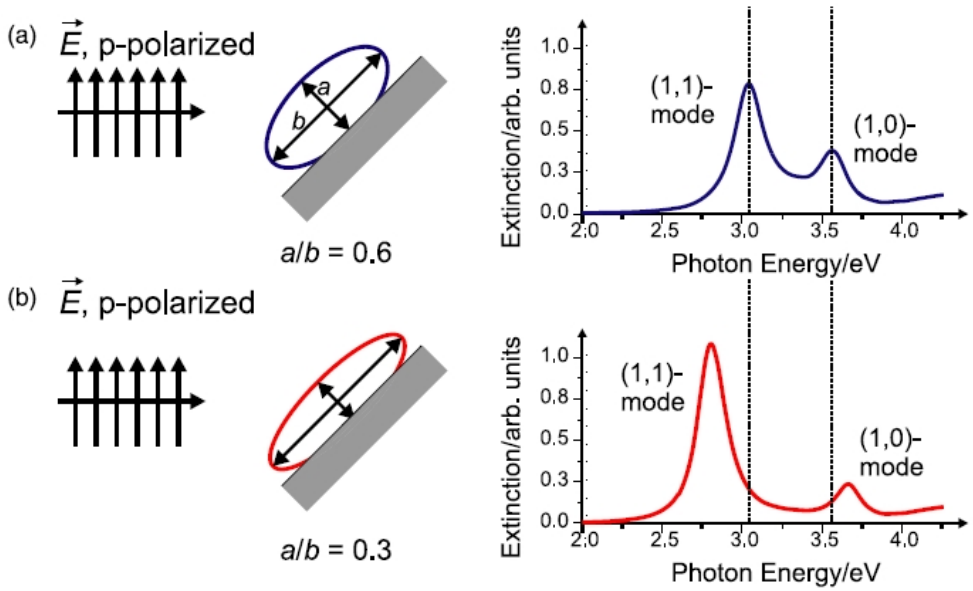

Figure 4.6: Schematic of a silver nanoparticle with different axial ratios on a substrate and calculated extinction spectra [Hub09]. For s-polarized light (as utilized in this thesis) only the (1,1) mode can be excited. Clearly visible is the shift of the plasmon resonance to lower energies with decreasing axial ratio.

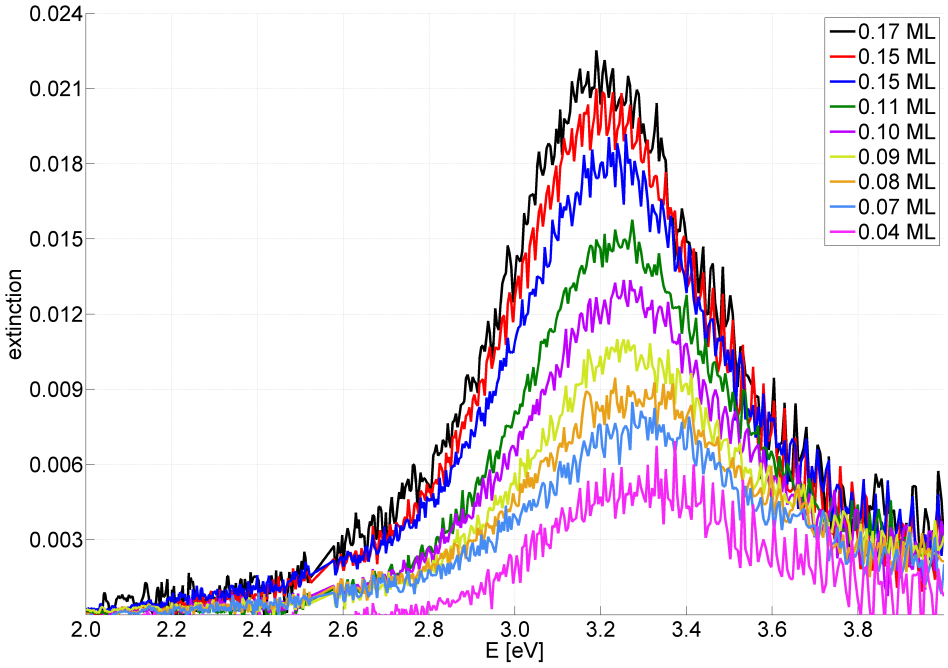

Figure 4.7: Cluster plasmon resonances measured with optical spectroscopy for low coverage at sample DO_05 (on SiO_2 silica glass) in vacuum.

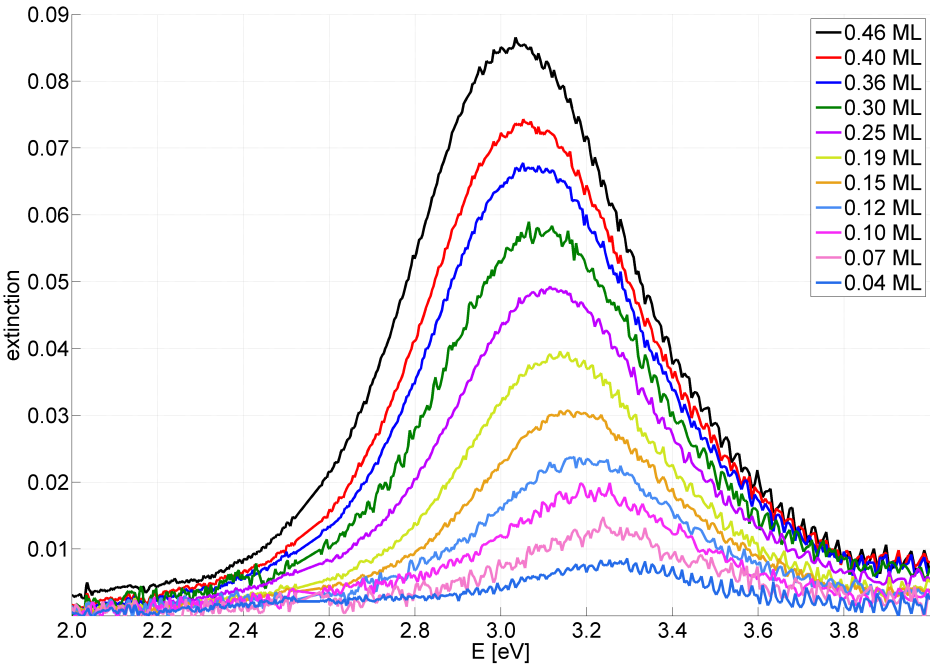

Figure 4.8: Cluster plasmon resonances measured with optical spectroscopy for high coverage at sample DO_05 (on SiO_2 silica glass) in vacuum.

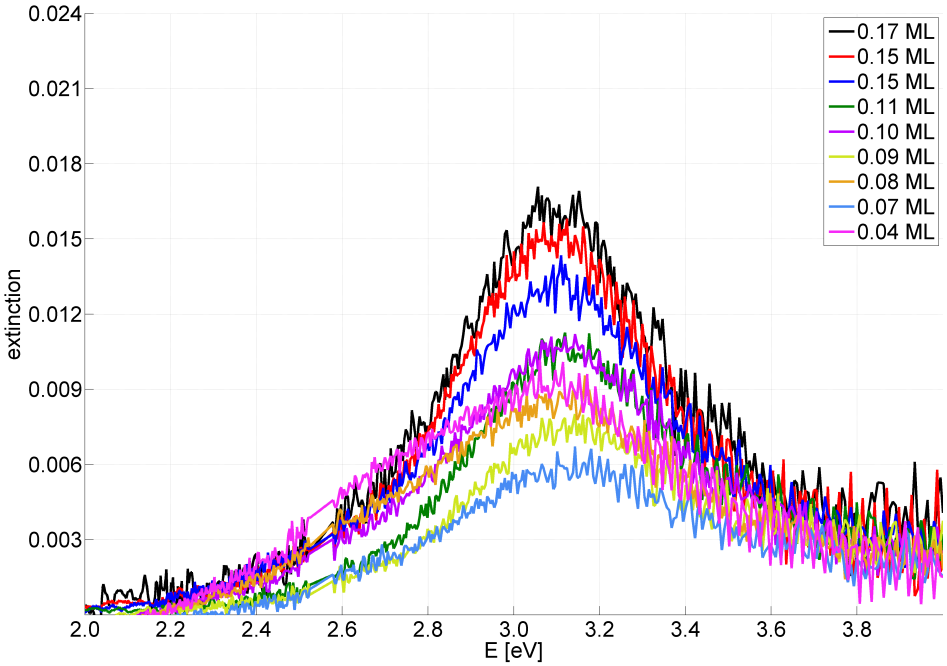

Figure 4.9: Cluster plasmon resonances measured with optical spectroscopy for low coverage at sample DO_05 (on SiO_2 silica glass) after exposure to air.

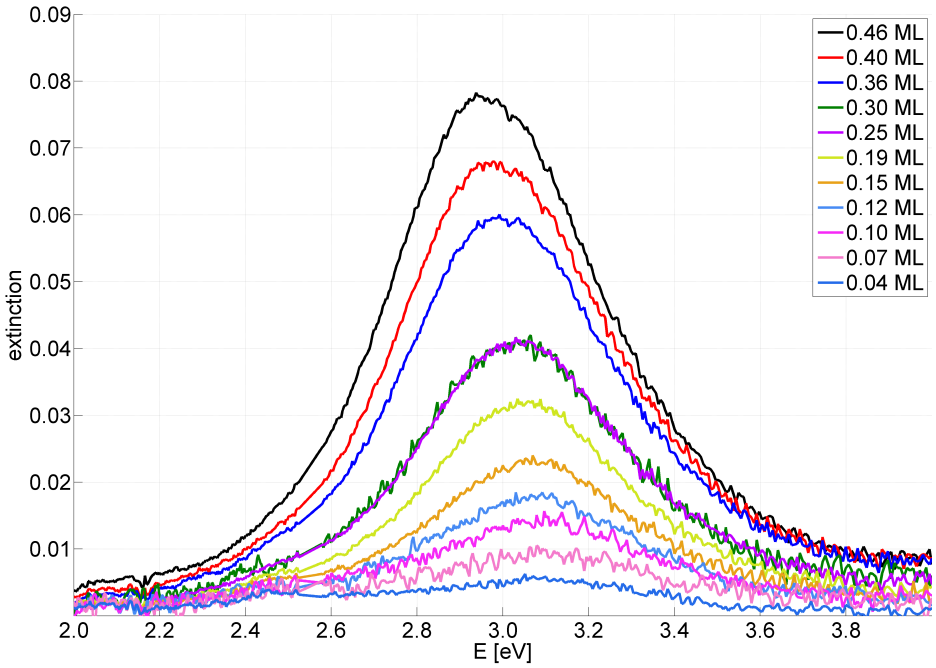

Figure 4.10: Cluster plasmon resonances measured with optical spectroscopy for high coverage at sample DO_05 (on SiO_2 silica glass) after exposure to air.

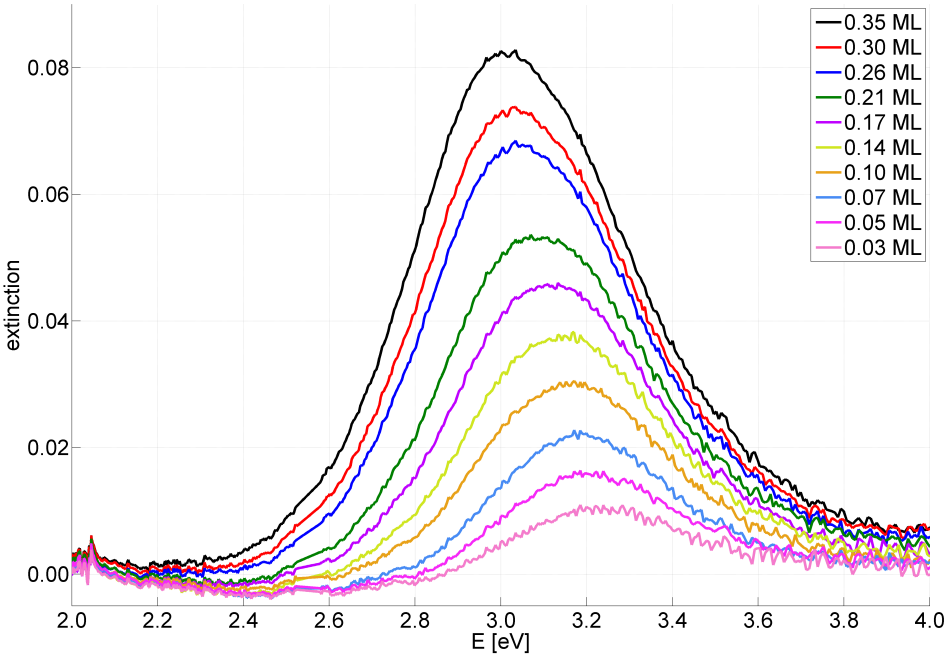

Figure 4.11: Cluster plasmon resonances measured with optical spectroscopy for low coverage at sample DO_12 (previously heated, on SiO_2 silica glass) in vacuum.

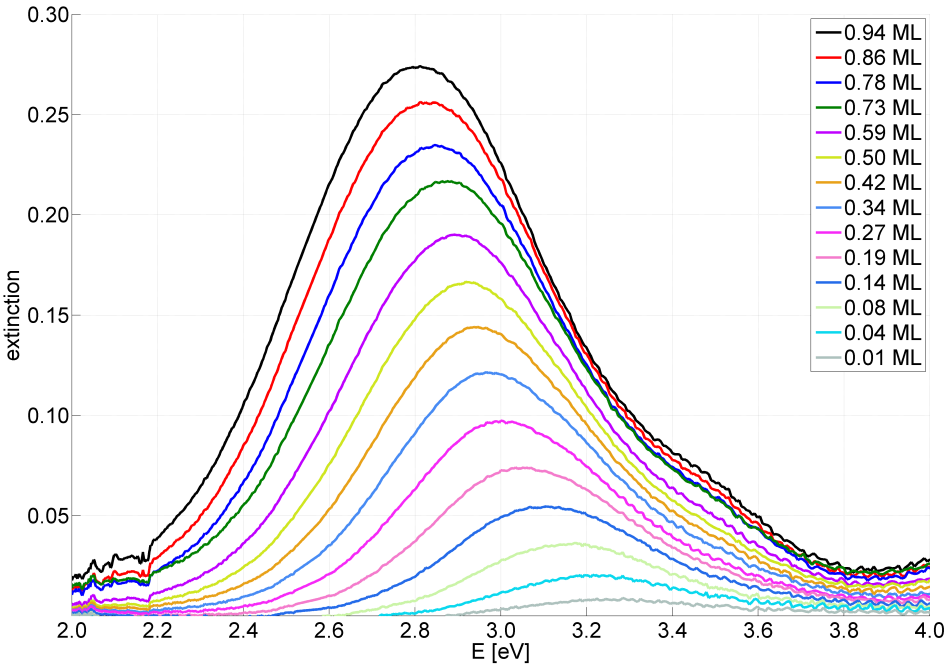

Figure 4.12: Cluster plasmon resonances measured with optical spectroscopy for high coverage at sample DO_12 (previously heated, on SiO_2 silica glass) in vacuum.

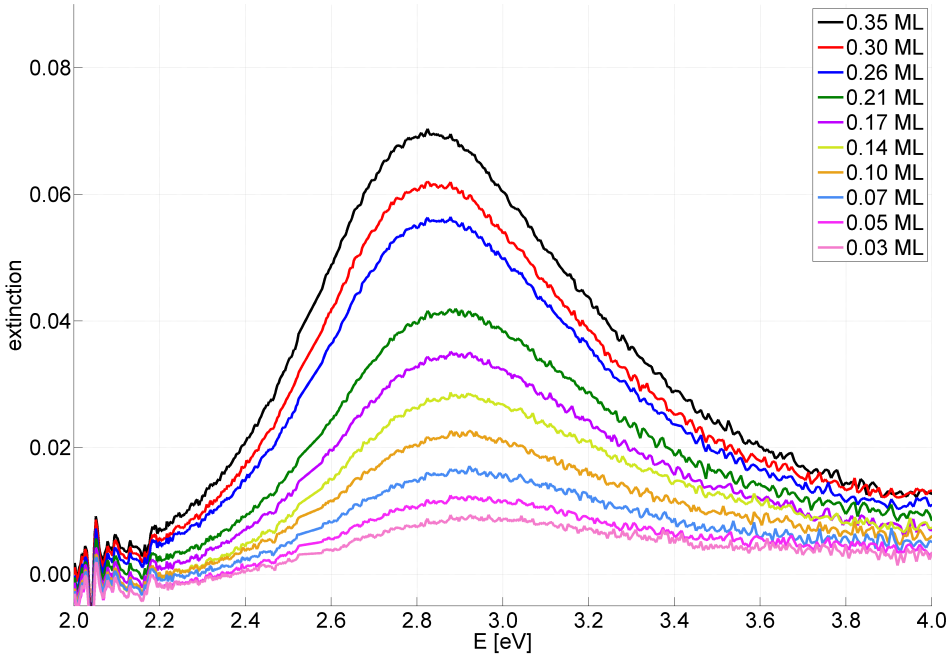

Figure 4.13: Cluster plasmon resonances measured with optical spectroscopy for low coverage at sample DO_12 (previously heated, on SiO_2 silica glass) after exposure to air.

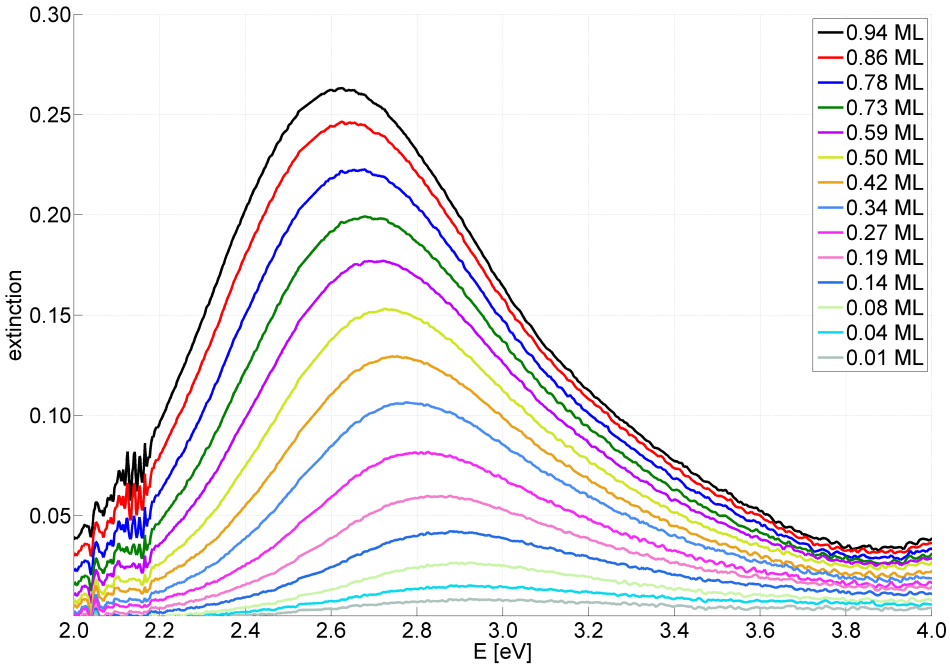

Figure 4.14: Cluster plasmon resonances measured with optical spectroscopy for high coverage at sample DO_12 (previously heated, on SiO_2 silica glass) after exposure to air.

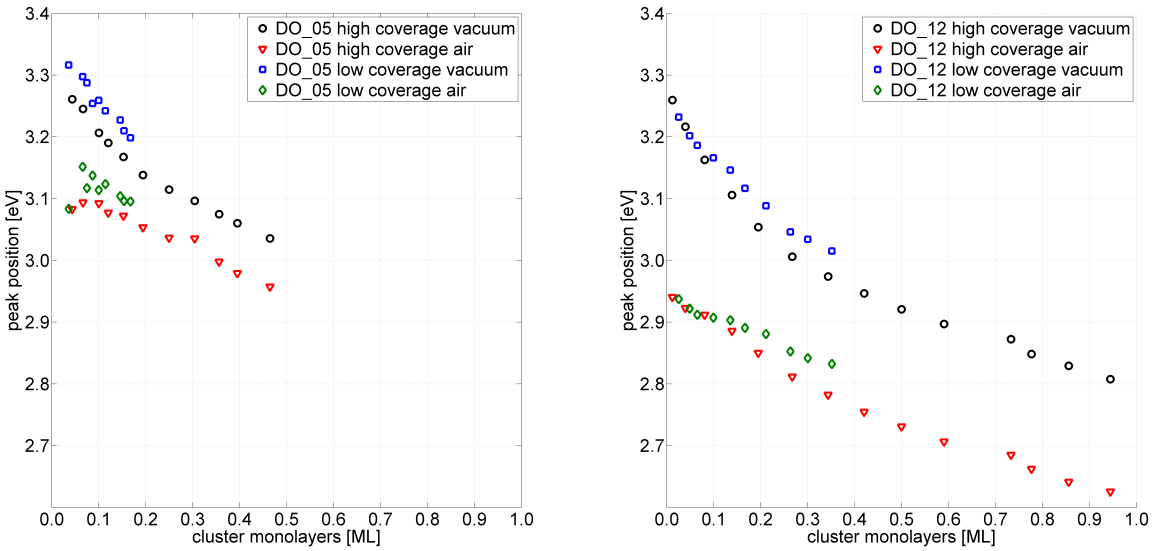

Figure 4.15: Left: Peak positions of DO_05 (on SiO_2 silica glass), right: Peak positions of DO_12 (on SiO_2 silica glass)

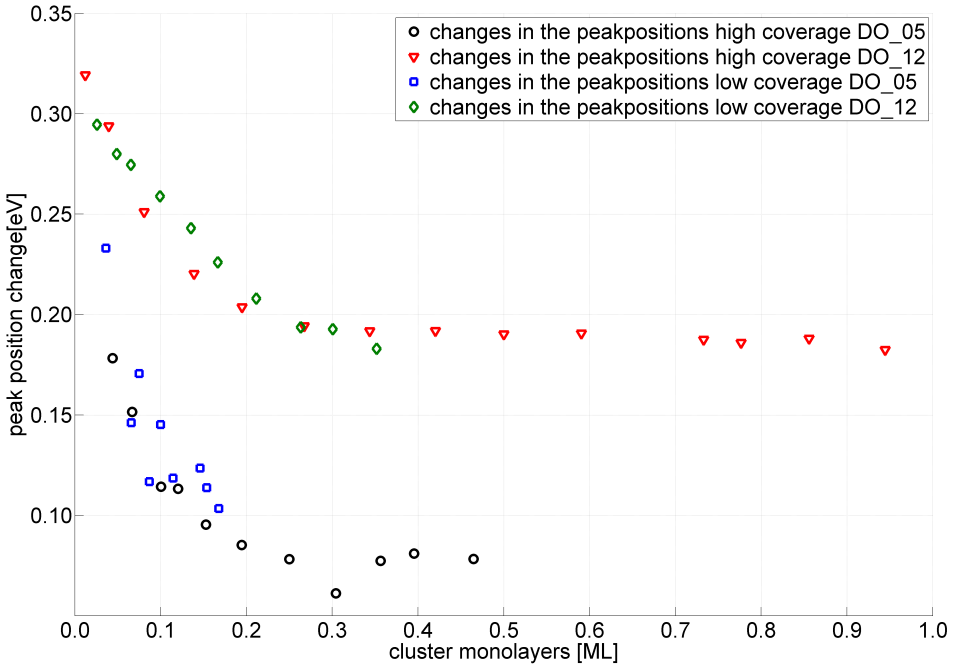

Figure 4.16: Peak positions shifts of DO_05 and DO_12 (on SiO_2 silica glass) after exposure to air.

DO_12 is shown in figure 4.15.
There is a significant offset between the energies of DO_05 and DO_12 in particular after exposure to air while the positions of the high and low coverage of one sample (DO_05 or DO_12, respectively) are similar for similar coverage.
An even better overview of the peak position changes after exposure to air gives figure 4.16. It is clearly visible, that the shift to smaller energies after exposure to air of DO_12 with a maximum of $\Delta E_{12\mathrm{max}} \approx 0.32$ eV for the lowest coverage is much larger than that of DO_05, for which the maximum shift at the lowest coverage is $\Delta E_{05\mathrm{max}} \approx 0.23$ eV. This hints on the existence of water monolayers on the SiO_2 substrate of DO_05, into which the clusters were deposited.
This partly water embedding yields not only a slight difference in the resonance position due to a change in the dielectric function of the environment ϵ_m and a change in the axial ratio of the ellipsoidal clusters, but could also protect the clusters against outer influences. This protection can be an explanation for the slightly higher energies of the plasmon resonances of DO_05 measured in vacuum compared to the peak positions of DO_12 (see figure 4.15) and results in a smaller peak shift after exposure to air.
Regarding the absolute positions of the plasmon resonances it is noticeable that for DO_05 the plasmon resonance energy is pretty stable for coverage <0.2 ML after exposure to air (figure 4.15). Although an overall offset of the resonances can be seen between the two deposition spots even for similar cluster monolayers, the gradient looks alike.
The two deposition spots of DO_12 are in even better agreement than the DO_05 resonances. Other than for sample DO_05 the cluster plasmon energies of the low and high coverage are in good agreement particularly in the region around 0.1 ML and below.
This difference could be explained with locally inhomogeneous water layers on the not heated SiO_2 substrate of DO_05, into which the clusters were deposited during the preparation in comparison to the previously heated substrate for DO_12. Such inhomogeneities could lead to an energy shift due to different effective dielectric functions of the cluster environment ϵ_m. This could then be a result of differently separated or partly coupling clusters. In that sense the heated substrate of DO_12 is a more well-defined sample system. The peak shift from vacuum to the measurements after exposure to air depends on the cluster coverage. For coverage below 0.2 ML the shift decreases with increasing coverage while above 0.2 ML the shift reaches an almost stable value of $\Delta E_{\mathrm{DO\_05}} = (0.075 \pm 0.004)$ eV and $\Delta E_{\mathrm{DO\_12}} = (0.194 \pm 0.005)$ eV, respectively. Here, it is remarkable that for the heated sample the shift stays comparably larger even for high cluster coverage than for the not heated sample DO_05.

After having discussed the energy position of the cluster plasmon resonance the full width at half maximum (FWHM) of the plasmon resonance will be discussed. Therefore, the FWHM is calculated by determining the half maximum of the lower energy flank of the measured extinction and doubling the half width (measured only for the lower energy half of the peak) at half maximum. Thus, the influence of interband transitions on the FWHM, which affect the form of the high energy flank of the extinction, is suppressed for the further investigations.
As has been mentioned before, the full width at half maximum (FWHM) of the measured extinction is directly influenced by the so called chemical interface damping (compare section 2.2.5). The calculated FWHM of the extinction spectra of DO_05 and DO_12 are

shown in figure 4.17. A remarkable trend can be seen for sample DO_12, for which the FWHM of the sample measured in vacuum increases with increasing cluster coverage while for DO_05 the width decreases with increasing coverage. This hints on a pronounced surface wetting of the previously heated SiO_2 substrate with the deposited silver and thus, with an increase of the contact area and the influence of the substrate's ϵ_m [Hil01]. Combined with the slight rise of the extinction in the low energy region with increasing coverage the increase of the FWHM for sample DO_12 could well be a sign for larger coupled cluster agglomerates on the surface. Nevertheless, this should be investigated further. For the samples measured after exposure to air the FWHM stays almost stable for DO_12 while for DO_05 the width decreases with increasing cluster coverage.
A comparison between the FWHM of DO_05 and DO_12 in vacuum and after exposure to air can be found in figure 4.18. Here is $\Delta\Gamma = \Gamma_{\text{air}} - \Gamma_{\text{vac}}$, which makes it clearly visible that for both samples the exposure to air results in an increase of the full width at half maximum. The difference decreases with increasing cluster coverage for both investigated samples but for the previously heated sample DO_12 the data of the two deposition spots are in better agreement than the data of DO_05. Regarding the lowest coverage of DO_05 the change in the width seems to be overestimated compared to the results for higher coverage. This could be an effect resulting from background signals in the lower energy flank, which tend to broaden the spectra but have no physical meaning (see low signal in low energy regime in figure 4.9). Assuming there is no background problem in the determination of the FWHM the pronounced change in the width could hint on a highly disproportionate reduction of the silver "core" underneath the adsorption layer and thus a decrease in the number of oscillating electrons.

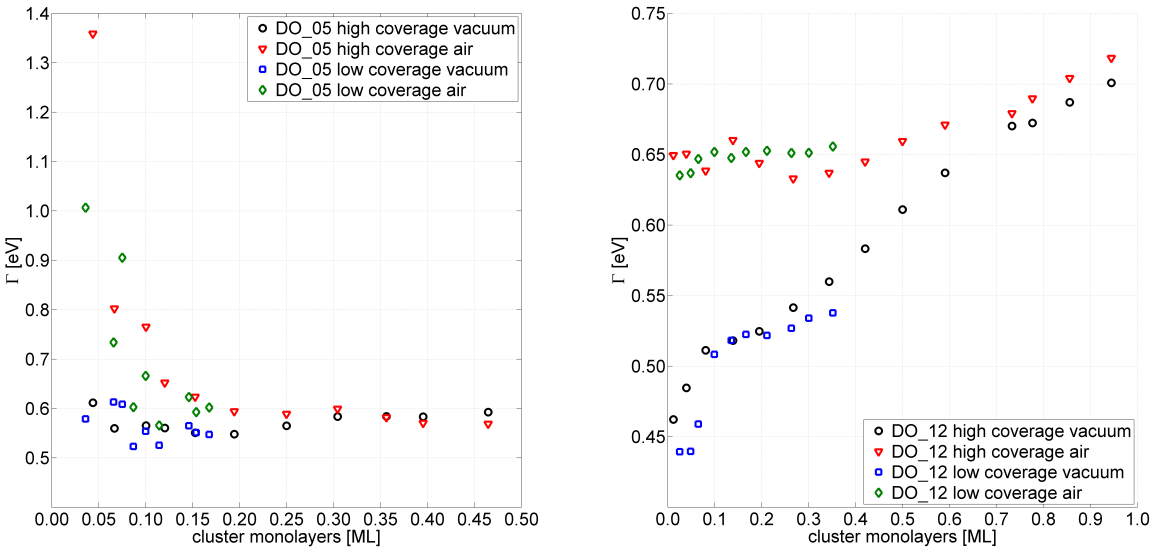

Figure 4.17: Left: Full width at half maximum Γ of DO_05 (on SiO_2 silica glass) in vacuum and after exposure to air, right: Full width at half maximum Γ of DO_12 (on SiO_2 silica glass) in vacuum and after exposure to air. Please notice the different scales on the y-axes.

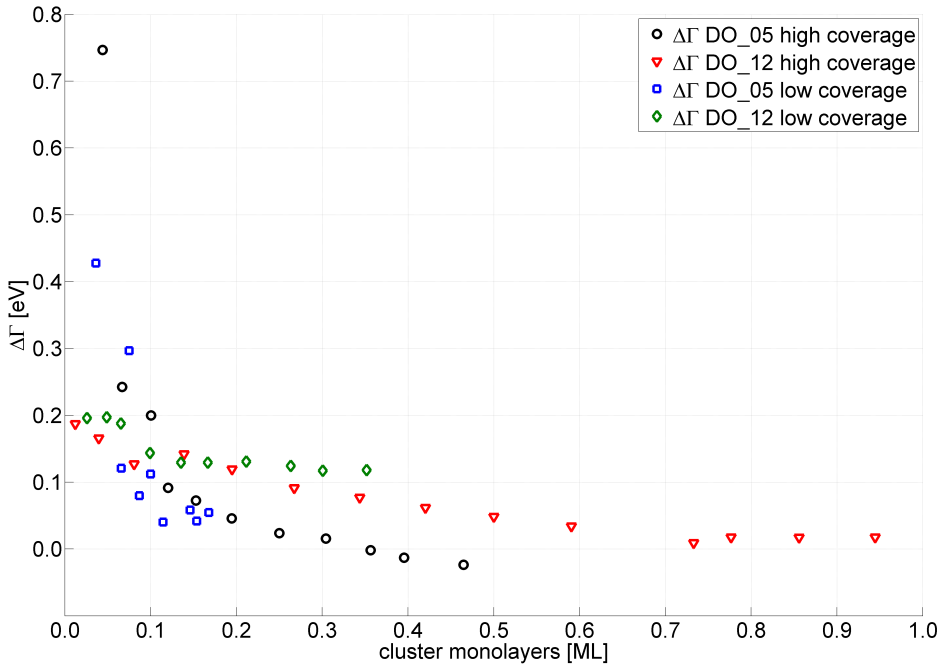

Figure 4.18: Change of the full width at half maximum from DO_05 and DO_12 (on SiO_2 silica glass) after exposure to air.

4.2.2 Clusters in PDMS on SiO_2 silica glass

The second sample system investigated is Ag clusters deposited into a polydimethylsiloxane (PDMS) film that was previously prepared on a SiO_2 substrate using spin cast. The purpose of the PDMS is to keep the clusters separated even for higher coverage than on the surface of a SiO_2 substrate.
Figures 4.19 and 4.22 show the extinctions measured in vacuum at the low coverage of samples DO_10 and DO_11, respectively. The first remarkable difference to the extinctions measured on the samples on SiO_2 substrates is a smaller shift to lower energies. While the peak position of the cluster plasmons measured on sample DO_12 for coverage between 0.04 - 0.25 ML shifts approx. 0.21 eV, the energy in a comparable interval of coverage for DO_11 changes only approx. 0.10 eV. This is a clear sign for a better separation of the clusters in the PDMS matrix in a range up to 0.25 ML.
The pronounced second peak, which is visible in the extinction spectra of the low coverage of DO_11 (see figure 4.22) could be a sign for a possible formation of larger particles on the PDMS surface (see figure 4.2). Another possible explanation is the formation of larger particles on the interface between PDMS and SiO_2 substrate. It is possible that a part of the deposited clusters was able to reach the bottom of the PDMS layer and started to nucleate on the SiO_2 surface. The reason why such a double peak is visible for DO_11 but not for DO_10 would then be the fact, that the PDMS layer of sample DO_11 is with (0.5±0.2) μm only half as thick as the layer on DO_10, which is (1.2±0.2) μm.
An additional fact that has to be accounted for is the effective dielectric function at the PDMS-SiO_2 interface, which is a mixture of the dielectric function of PDMS $\epsilon_{\mathrm{PDMS}} = 2.65$ and the dielectric function of silica glass $\epsilon_{\mathrm{SiO_2}} = 1.45$.
Recent unpublished experiments performed by D. Engemann (TU Dortmund) of clusters in a PDMS film of 30 μm also show a double peak structure similar to the features seen in figure 4.22 making this explanation less probable. Another influence can be a change of the axial ratio of clusters on the PDMS surface or at the PDSM-SiO_2 interface, which yields an energy shift as has been previously explained by Hövel [Höv97] and Hubenthal [Hub09]. Thus, the superposition of the two extinction maxima could be the result of nearly spherical clusters inside the PDMS layer and deformed clusters on the PDMS surface or at the PDMS-SiO_2 interface.
Figures 4.20 and 4.23 show the extinctions measured in vacuum at the high coverage of DO_10 and DO_11, respectively. It is clearly visible, that there is a pronounced red shift of the plasmon resonances with increasing cluster coverage, which is similar to the red shift on silica glass.

Regarding the total energies of the plasmon resonances there is a shift to lower energies after exposure to air. The extinction spectra taken after exposure to air can be seen in figure 4.21 for the high coverage of DO_10 and 4.24 and 4.25 for the low and high coverage of DO_11, respectively. A better overview on the peak positions of the plasmon resonances gives figure 4.26. Clearly visible is that for similar coverage below 0.5 ML the plasmon energy of sample DO_11 is higher than for DO_10. For both samples the peak positions of the low and high coverage fit very well. Regarding the additional peak shift resulting from exposure to air for both investigated samples the shift decreases with increasing cluster

coverage. This is in good agreement with the findings for clusters on SiO_2 silica glass.
A comparison between the peak shifts of both investigated PDMS samples after exposure to air is given in figure 4.27. Despite the visible difference in total peak position of the plasmon resonances for low coverage the energy shift after exposure to air looks very similar for the compared samples Do_10 and DO_11. Thus, the influence of an adsorption layer on the clusters' surface seems to be independent of the layer thickness, especially for lower coverage.
Other than for clusters on SiO_2 silica glass the peak changes do not seem to reach a stable value for higher coverage but decrease with increasing coverage. For sample DO_10 the maximum shift for low coverage amounts to $\Delta E_{10\mathrm{max}} \approx 0.31$ eV and for sample DO_11 to $\Delta E_{11\mathrm{max}} \approx 0.32$ eV, which is in very good agreement and thus, comparable to the maximum shift of the previously heated sample DO_12 with Ag clusters on SiO_2. For the highest coverage of approx. 2.24 ML the energy shift after exposure to air of DO_10 amounts to $\Delta E_{10} \approx 0.06$ eV and for the highest coverage of approx. 1.02 ML the shift for DO_11 reaches as value of $\Delta E_{11} \approx 0.09$ eV.

The full width at half maximum (FWHM) of the investigated samples in PDMS are shown in figure 4.28 and their changes after exposure to air can be found in figure 4.29. It is visible that for both samples the FWHM first decreases with increasing coverage up to a coverage of approx. 0.5 ML for DO_10 and approx. 0.3 ML for DO_11.
Above this threshold the FWHM increases with increasing cluster coverage. Especially the behavior in the region of low coverage is different from the previously investigated sample system clusters on SiO_2 silica glass (compare section 4.2.1).
Due to the afore mentioned problems with changes of the axial ratio of parts of the deposited clusters on the PDMS surface or at the PDMS-SiO_2 interface or even beginning coalescence the FWHM of the low coverage in particular is not really reliable. This is a subject, which has to be investigated further.
For both investigated samples the exposure to air yields an increase in FWHM. The value of the increase decreases for higher coverage, which is the same behavior as already seen for clusters on SiO_2 silica glass.

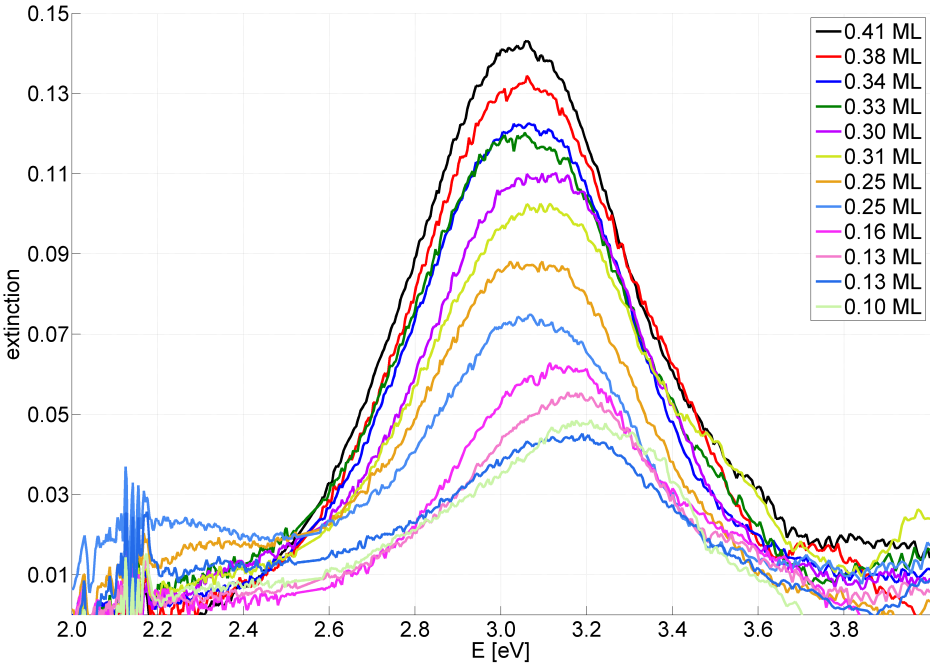

Figure 4.19: Cluster plasmon resonances measured with optical spectroscopy for low coverage at sample DO_10 (in PDMS) in vacuum.

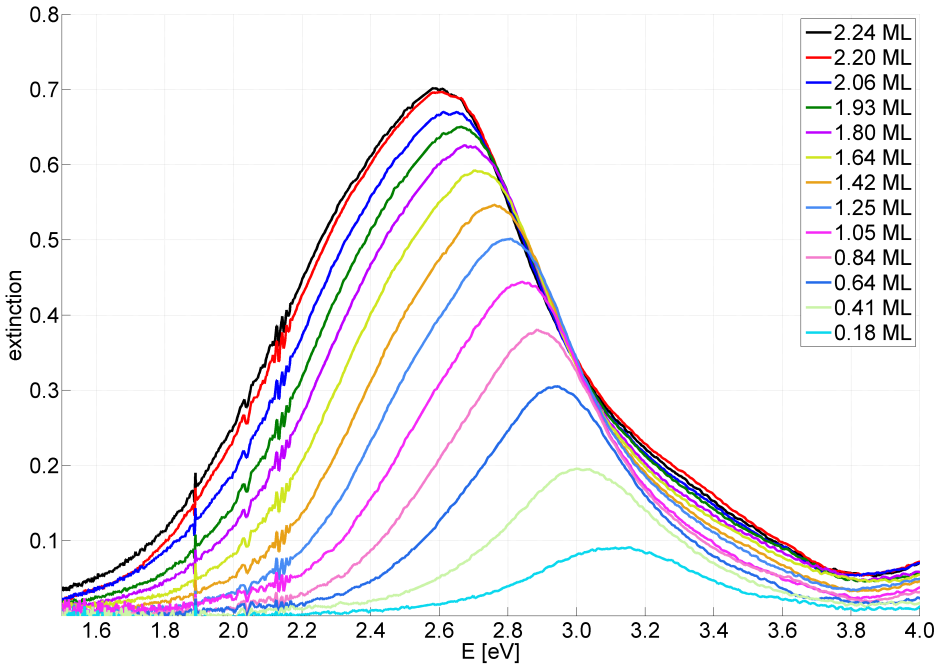

Figure 4.20: Cluster plasmon resonances measured with optical spectroscopy for high coverage at sample DO_10 (in PDMS) in vacuum.

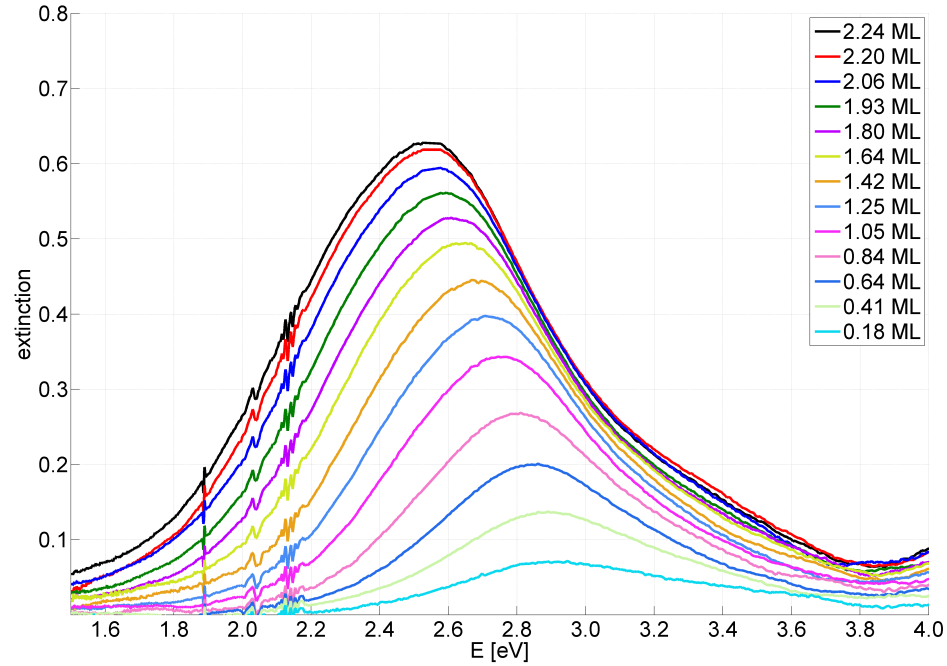

Figure 4.21: Cluster plasmon resonances measured with optical spectroscopy for high coverage at sample DO_10 (in PDMS) after exposure to air.

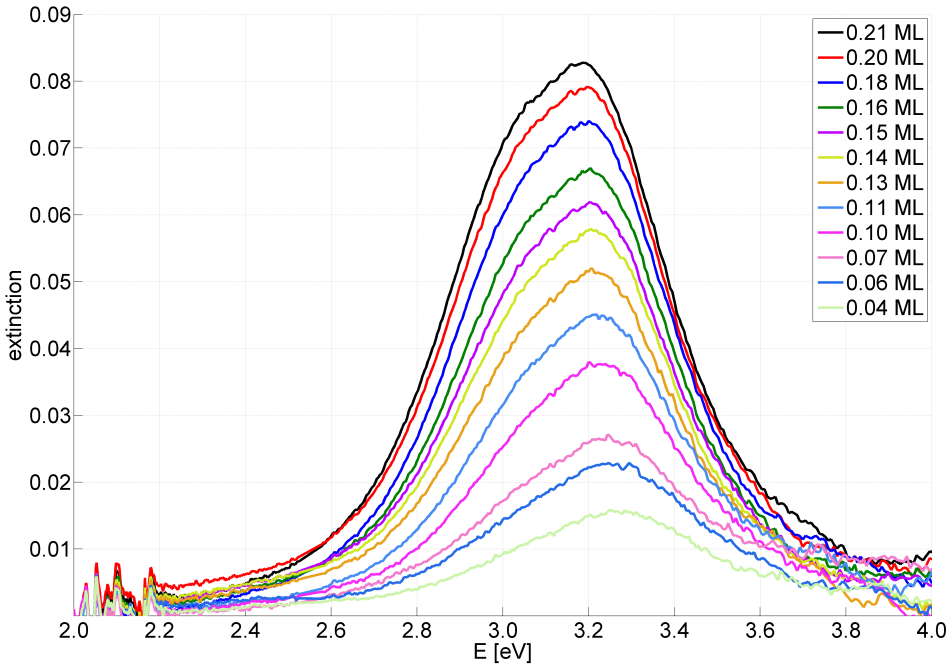

Figure 4.22: Cluster plasmon resonances measured with optical spectroscopy for low coverage at sample DO_11 (in PDMS) in vacuum.

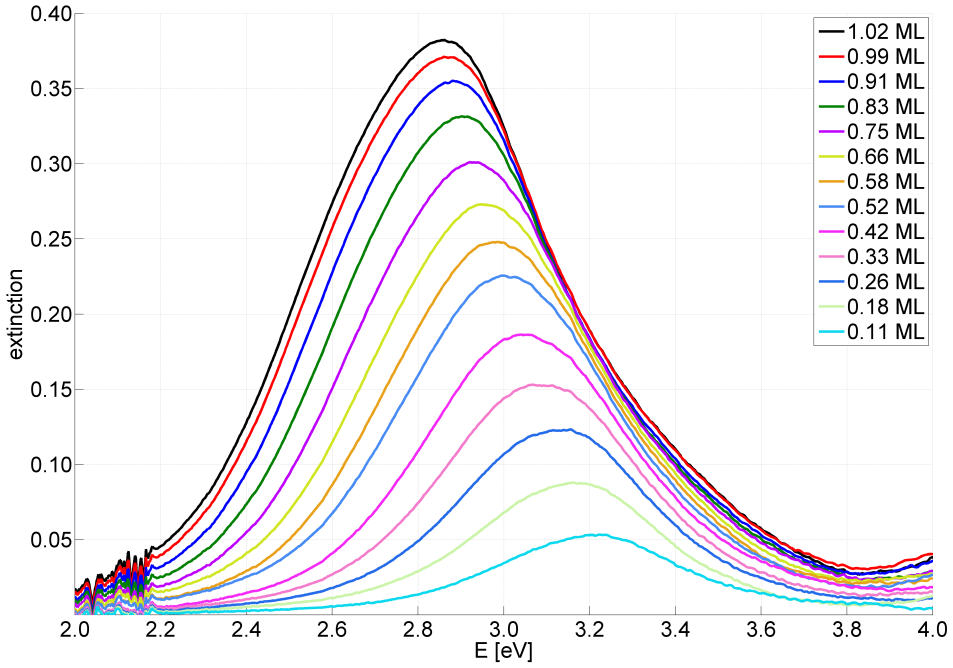

Figure 4.23: Cluster plasmon resonances measured with optical spectroscopy for high coverage at sample DO_11 (in PDMS) in vacuum.

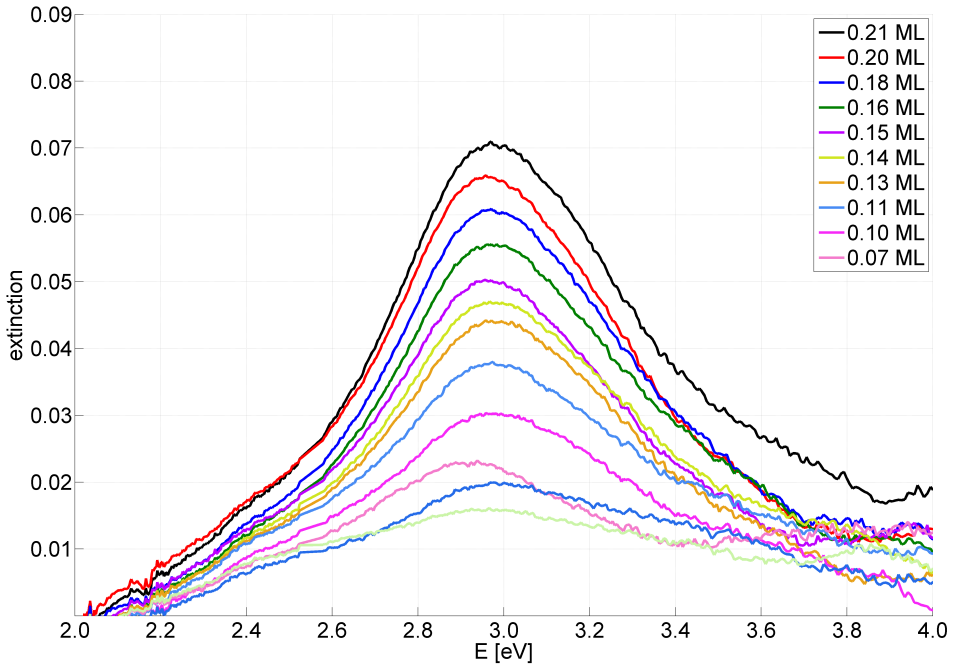

Figure 4.24: Cluster plasmon resonances measured with optical spectroscopy for low coverage at sample DO_11 (in PDMS) after exposure to air.

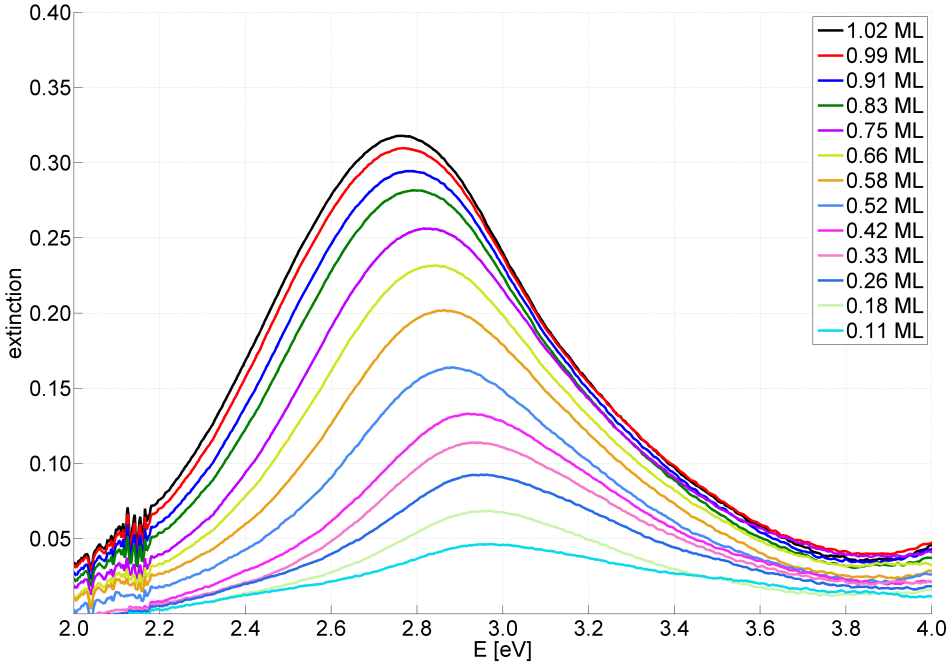

Figure 4.25: Cluster plasmon resonances measured with optical spectroscopy for high coverage at sample DO_11 (in PDMS) after exposure to air.

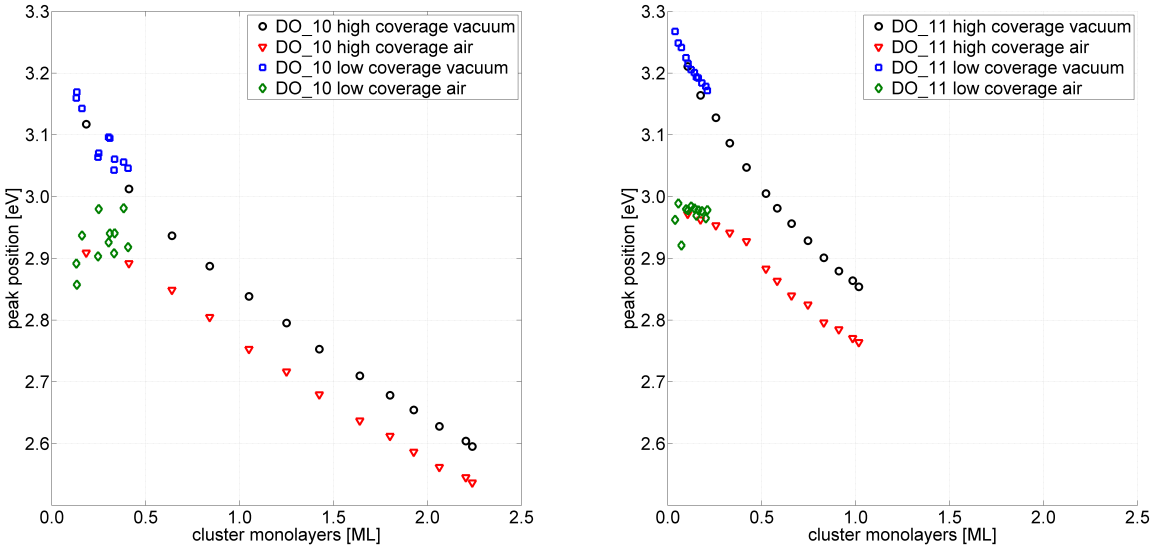

Figure 4.26: Left: Peak positions of DO_10 (in PDMS), right: Peak positions of DO_11 (in PDMS)

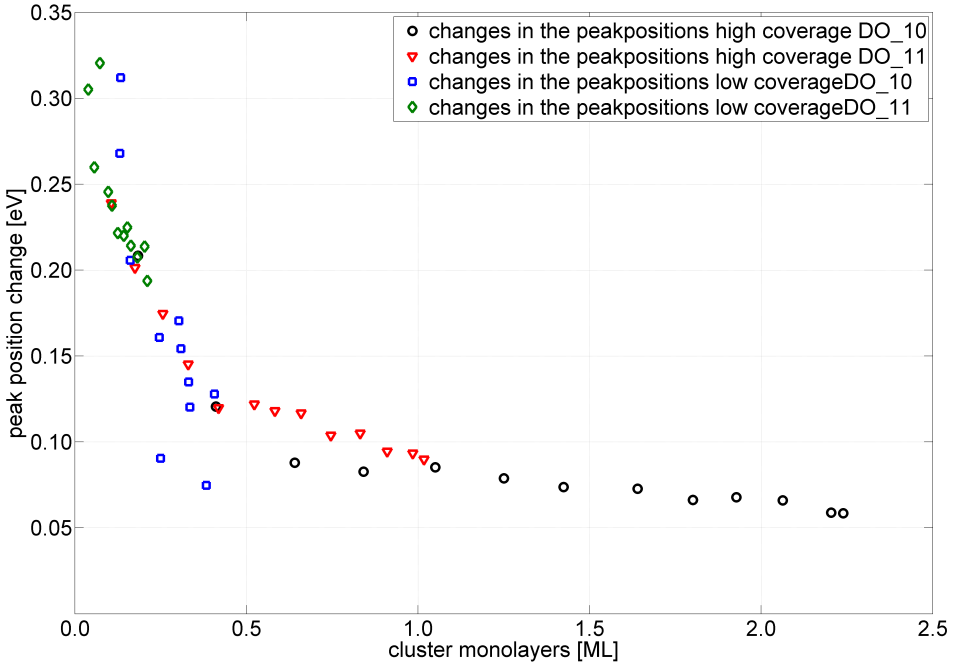

Figure 4.27: Shifts of the plasmon resonances of samples DO_10 and DO_11 (in PDMS) after exposure to air.

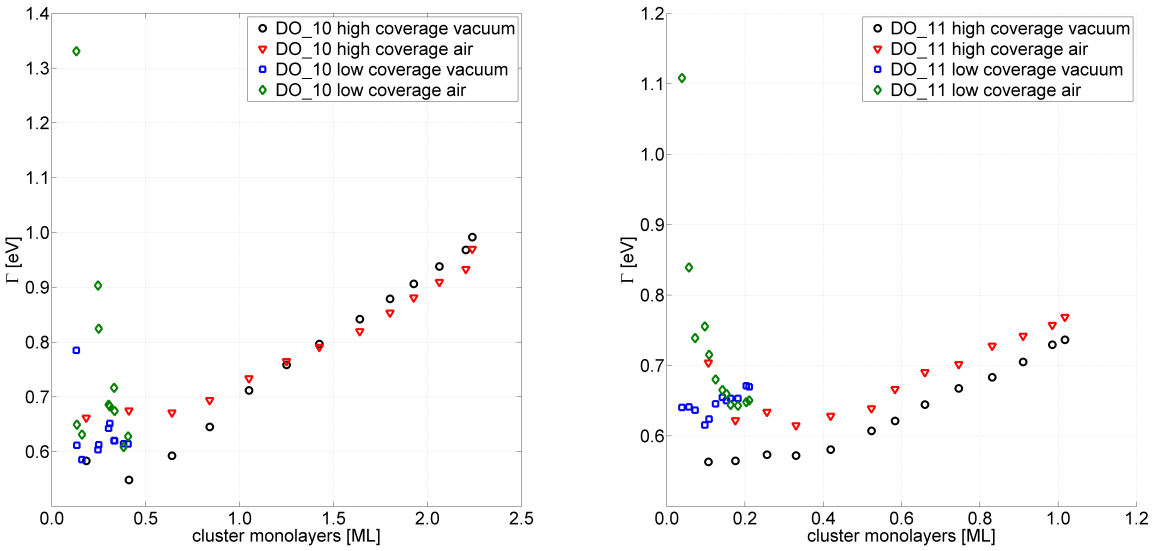

Figure 4.28: Left: Full width at half maximum Γ of DO_10 (in PDMS) in vacuum and after exposure to air, right: Full width at half maximum Γ of DO_11 (in PDMS) in vacuum and after exposure to air. Please notice the different scales on the y-axes.

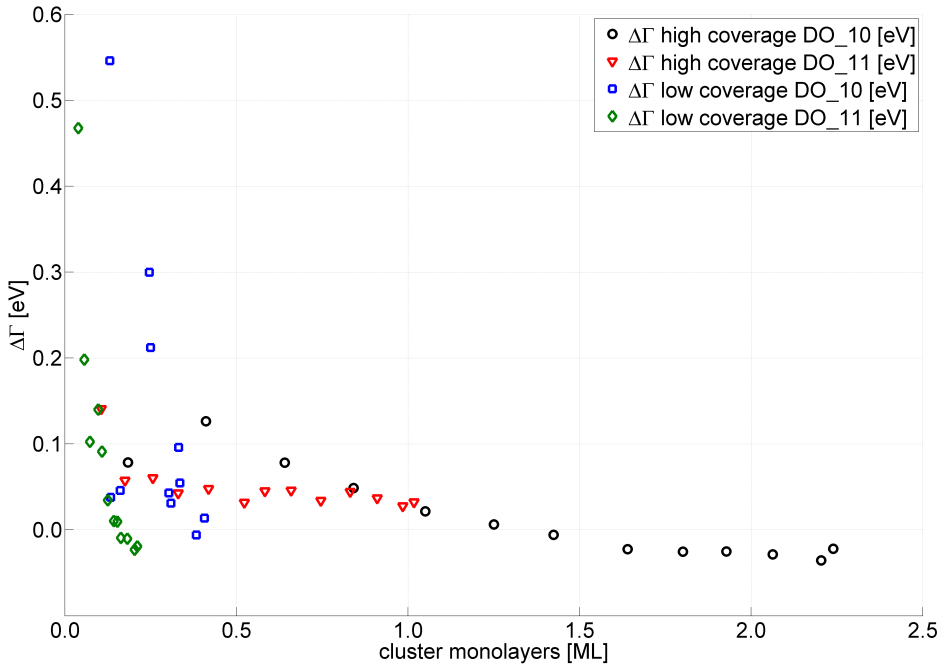

Figure 4.29: Change of the full width at half maximum from DO_10 and DO_11 (in PDMS) after exposure to air.

4.2.3 Clusters in SiO_2 aerogel

Another matrix material, which was used in the frame of this work is SiO_2 aerogel. As a first sample with this material DO_14 was prepared by depositing a certain cluster coverage into a SiO_2 aerogel "drops" (diameter $\approx$ 20 mm, height $\approx$ 5 mm) and the same coverage on a SiO_2 silica glass surface.
Thus, it is possible to directly compare the effects of electromagnetic coupling and beginning coalescence on the substrate and in the aerogel network.
Figures 4.30 and 4.31 show the plasmon resonances measured in vacuum at the aerogel deposition spot and the SiO_2 deposition spot, respectively. Since there was a problem during the deposition of the clusters it was not possible to achieve similar coverage for the two deposition spots. Despite these circumstances it is clearly visible that the total plasmon energy is much higher for the DO_14 aerogel sample (around 3.3 eV) than for the SiO_2 silica glass sample (maximum around 3 eV for lowest coverage).

Although impurities in the aerogel caused deformations of the spectra (see e.g. black curve for 1.74 ML in figure 4.30) the total plasmon energy stays almost stable up to a coverage of approx. 1.74 ML in the SiO_2 aerogel, while the clusters on SiO_2 silica glass show the well known behavior of electromagnetic coupling and beginning coalescence above a coverage of approx. 0.1 ML (compare section 4.2.1). There is a pronounced red shift of the plasmon resonances for the clusters on SiO_2 silica glass of DO_14.
The cluster plasmon resonances measured at the same clusters of sample DO_14 after exposure to air are given in figures 4.32 and 4.33 for clusters in SiO_2 aerogel and on SiO_2 silica glass, respectively. There is a broadening of the spectra taken for the clusters embedded in SiO_2 aerogel. The cluster plasmon resonances measured for the clusters on SiO_2 silica glass after exposure to air look very similar to the spectra taken in vacuum. This will be discussed in detail later in this section.
As a second sample DO_15 was prepared with two deposition spots of Ag clusters in SiO_2 aerogel with different cluster coverage. Plasmon resonances measured in vacuum at DO_15 are shown in figures 4.34 and 4.35 for low coverage and high coverage, respectively.
As can be seen at the low coverage the cluster plasmon resonance energy stays almost stable at energies around 3.5 eV up to a coverage of approx. 3.93 ML. This hints on a good separation of the clusters in the aerogel matrix.
For even higher coverage (figure 4.35) the energy stays stable as well, but there is an increase in the extinction at the low energy flank of the plasmon resonance. This increase and thus, the broadening of the resonance, hints on the formation of islands and is a result of the transition to a conducting metal film. For coverage above 7 ML the height of the extinction does not further increase.
The visible structure in the energy range between 2.8 - 3.2 eV is an artifact of a spectral shift of the combined deuterium halogen lamp due to generation of heat and thus, no feature of the cluster plasmon resonance.
Figures 4.36 and 4.37 show the extinction spectra measured for DO_15 after exposure to air at the low coverage and high coverage, respectively. For both deposition spots there is a pronounced broadening of the spectra, which can be a result of chemical interface damping due to the formation of an adsorption layer on the clusters' surface.

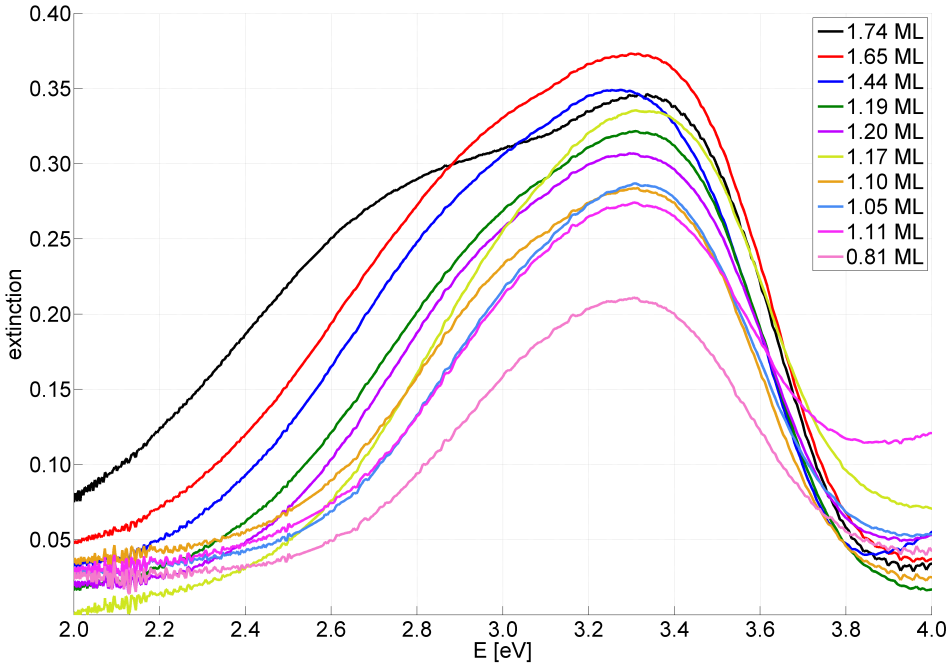

Figure 4.30: Cluster plasmon resonances in SiO_2 aerogel measured with optical spectroscopy at sample DO_14 in vacuum.

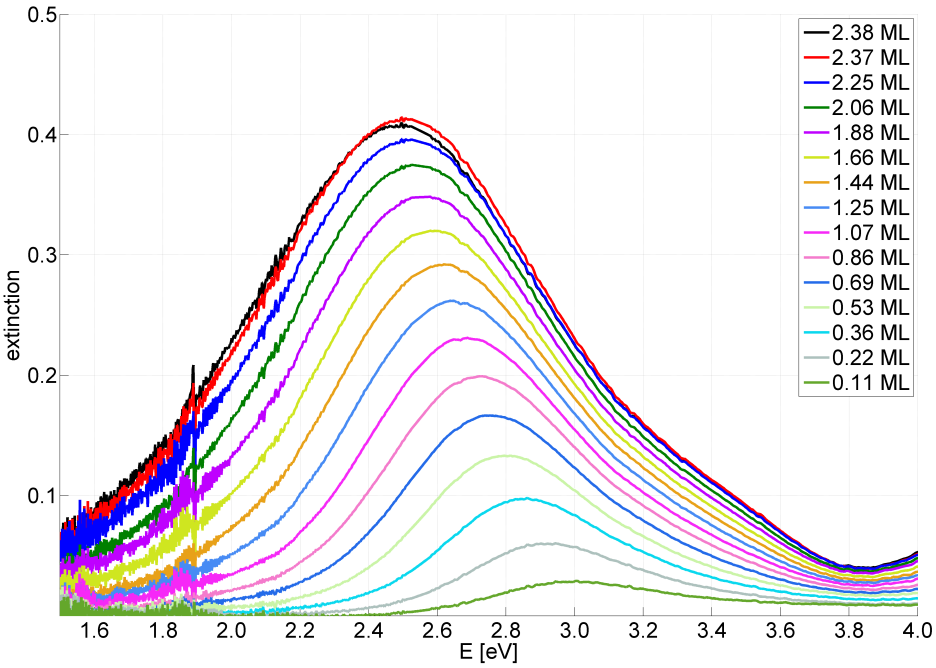

Figure 4.31: Cluster plasmon resonances on SiO_2 silica glass measured with optical spectroscopy at sample DO_14 in vacuum.

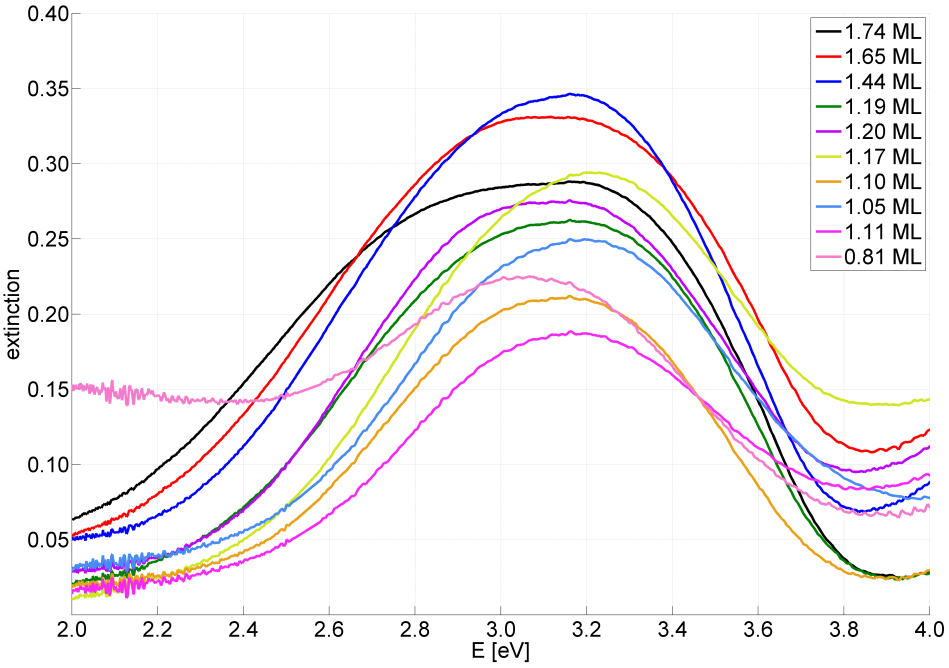

Figure 4.32: Cluster plasmon resonances in SiO_2 aerogel measured with optical spectroscopy at sample DO_14 after exposure to air.

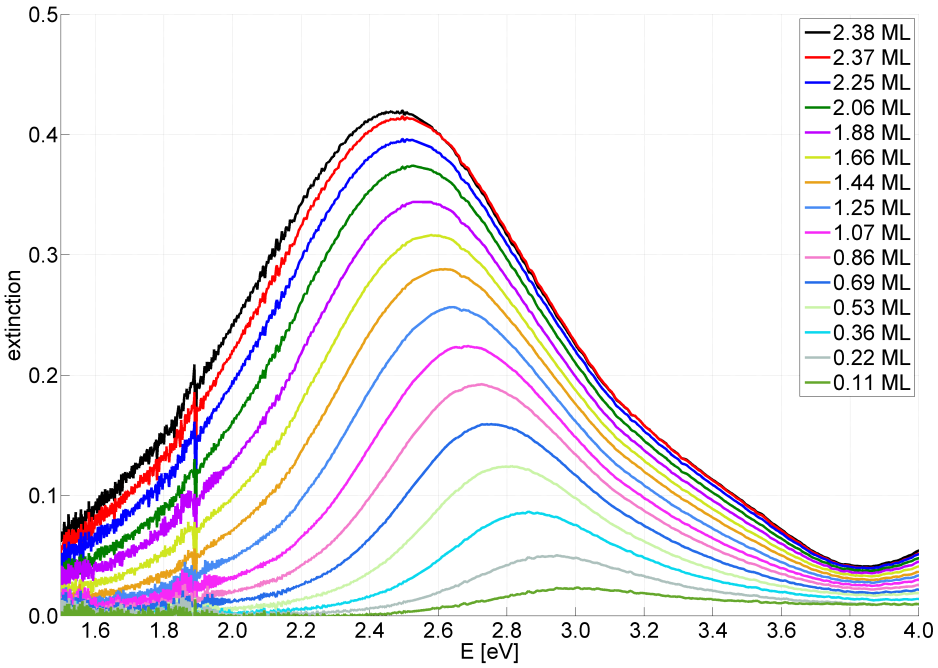

Figure 4.33: Cluster plasmon resonances on SiO_2 silica glass measured with optical spectroscopy at sample DO_14 after exposure to air.

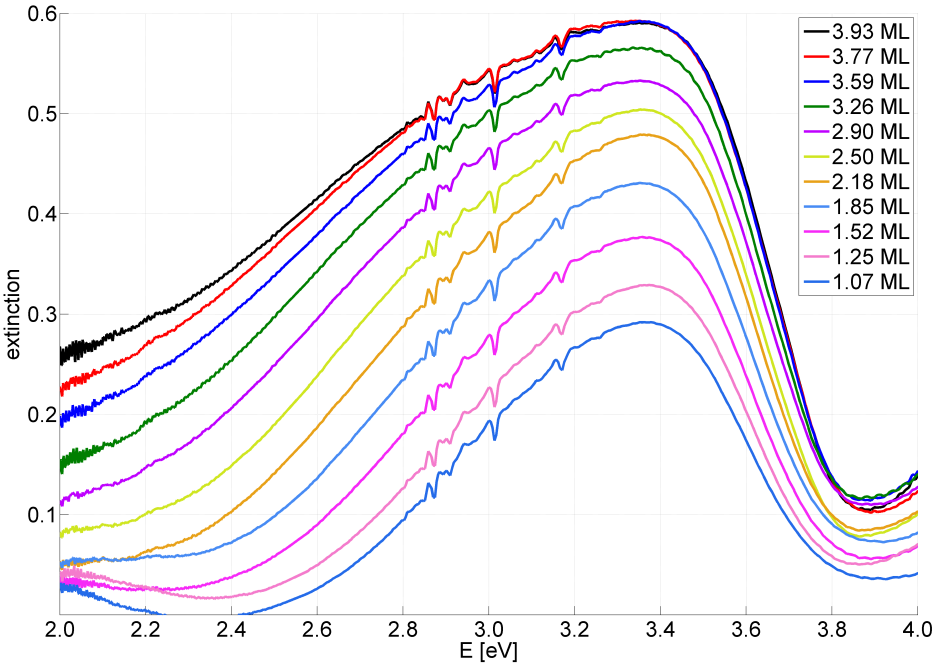

Figure 4.34: Cluster plasmon resonances in SiO_2 aerogel measured with optical spectroscopy at low coverage of sample DO_15 in vacuum.

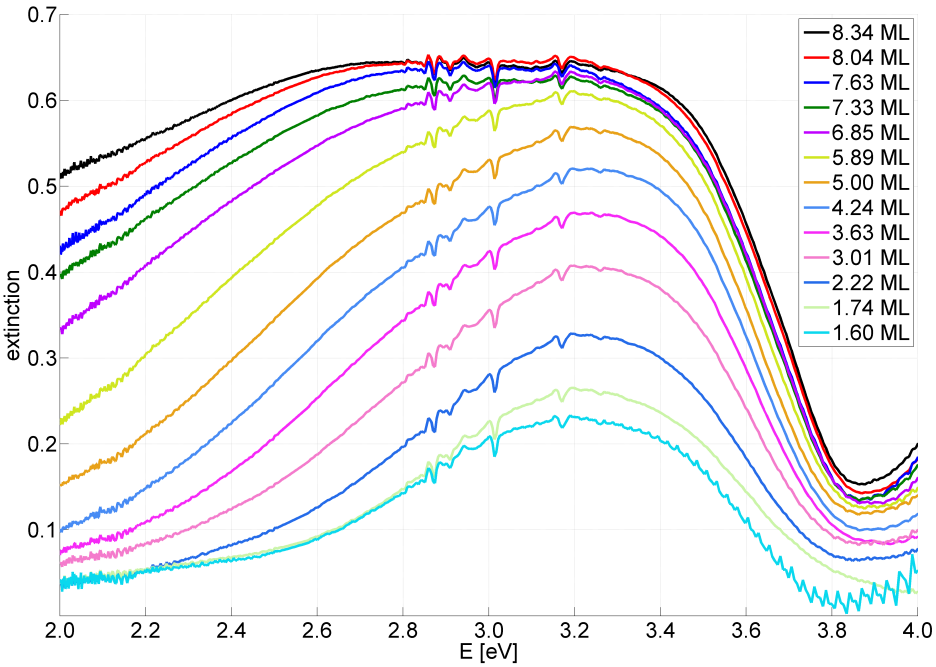

Figure 4.35: Cluster plasmon resonances in SiO_2 aerogel measured with optical spectroscopy at high coverage of sample DO_15 in vacuum.

Figure 4.38 shows the plasmon energy peak positions for the investigated samples DO_14 and DO_15 in vacuum and after exposure to air.
Regarding DO_14 first and particularly the Ag clusters on SiO_2 silica glass, there is a remarkable difference to the afore discussed samples DO_05 and DO_12 with clusters on SiO_2 silica glass. Here, the cluster plasmon resonances of clusters of sample DO_14 exhibit almost no red shift after exposure to air. In both cases the plasmon resonance decreases with increasing cluster coverage starting around 3.0 eV for the lowest coverage of approx. 0.11 ML and ending with 2.5 eV for approx. 2.38 ML.
The optical absorption spectra of the Ag clusters deposited into the SiO_2 aerogel exhibit clearly visible deformations originating from impurities in the aerogel (compare figure 4.30). Though, remarkably, the plasmon energy lies around 3.3 eV in vacuum and around 3.15 eV after exposure to air hinting on good cluster separation in the aerogel matrix.
For sample DO_15 the low coverage in vacuum shows the highest plasmon energy around 3.34 eV with only slight changes. The higher coverage shows an unstable behavior with slight fluctuations around 3.25 eV. The highest coverage above a threshold of approx. 7 ML there is a visible decrease in the plasmon resonance energy. This decrease can be explained with the pronounced development of bulk-like properties and thus, difficulties to determine the peak position (compare figure 4.35).
Figure 4.39 shows the changes of the peak positions after exposure to air. Here, it is clearly visible that the clusters on SiO_2 silica glass of DO_14 show no significant shift after exposure to air. This is in total disagreement to the findings not only on previously discussed samples DO_05 and DO_12 but also with findings reported by Hövel [Höv93, Hen09]. This behavior can not be explained by any of the afore mentioned mechanisms. It could be a result of problems with the determination of the position on the sample during the optical measurements. Problems with the digital caliper, with which the z-positions on the sample can be precisely determined (compare section 4.2), yielded the necessity to reconstruct the z-positions. Possible errors in the reconstruction could thus be the origin of this odd behavior.
The peak positions of sample DO_15 show a mean peak shift after exposure to air of $\Delta E_{15\text{high}} = (0.08 \pm 0.02)$ eV for the high coverage and a mean peak shift of $\Delta E_{15\text{low}} = (0.167 \pm 0.005)$ eV for the low coverage. The shift of the low coverage is thus only half the value of the peak shift determined for the lowest coverage of clusters in PDMS (compare section 4.2.2) hinting on a better shielding of the clusters against the formation of an adsorbate layer during exposure to air.

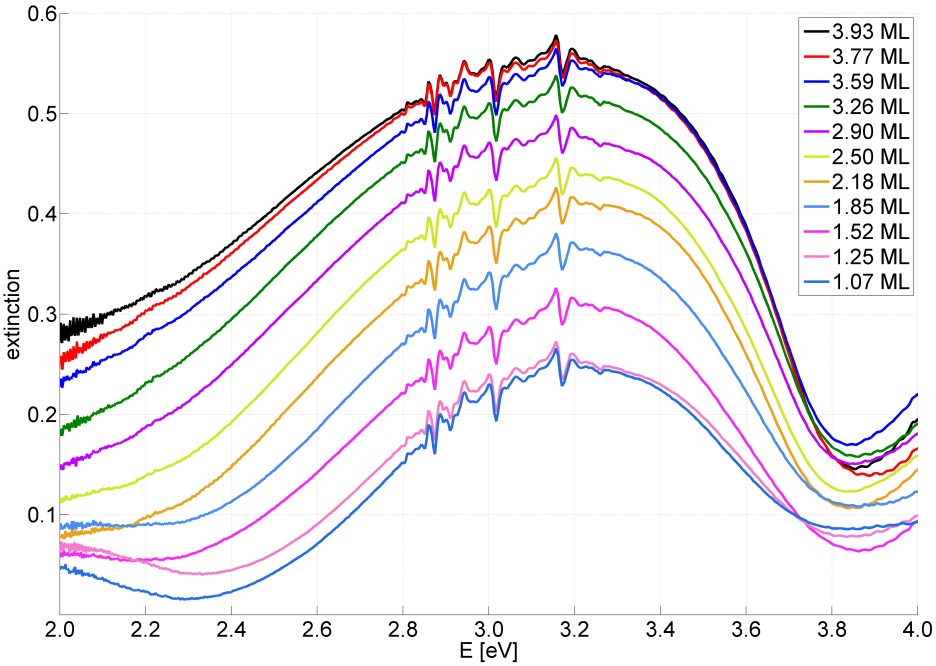

Figure 4.36: Cluster plasmon resonances in SiO_2 aerogel measured with optical spectroscopy at low coverage of sample DO_15 after exposure to air.

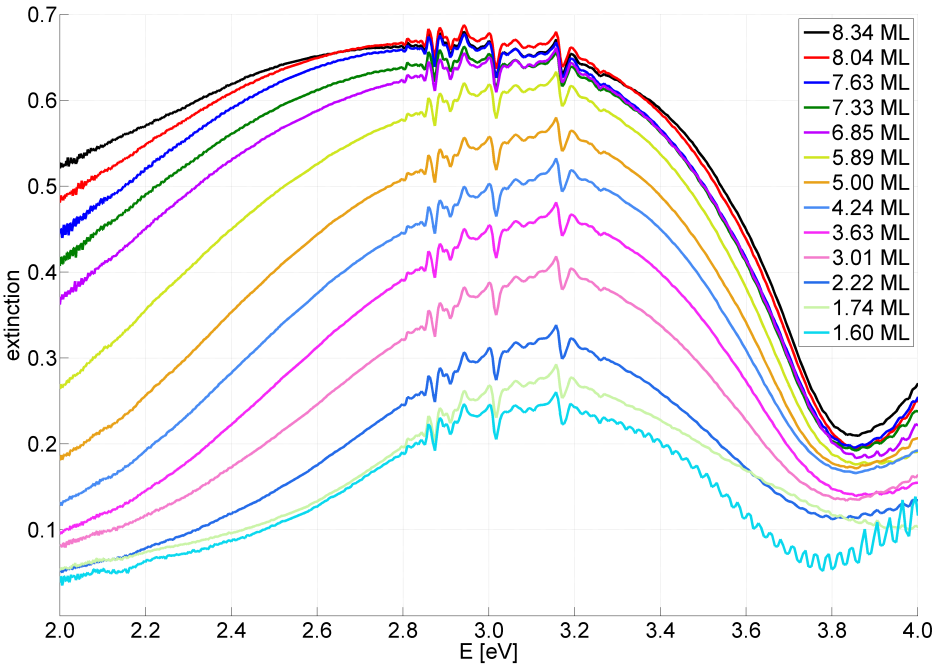

Figure 4.37: Cluster plasmon resonances in SiO_2 aerogel measured with optical spectroscopy at high coverage of sample DO_15 after exposure to air.

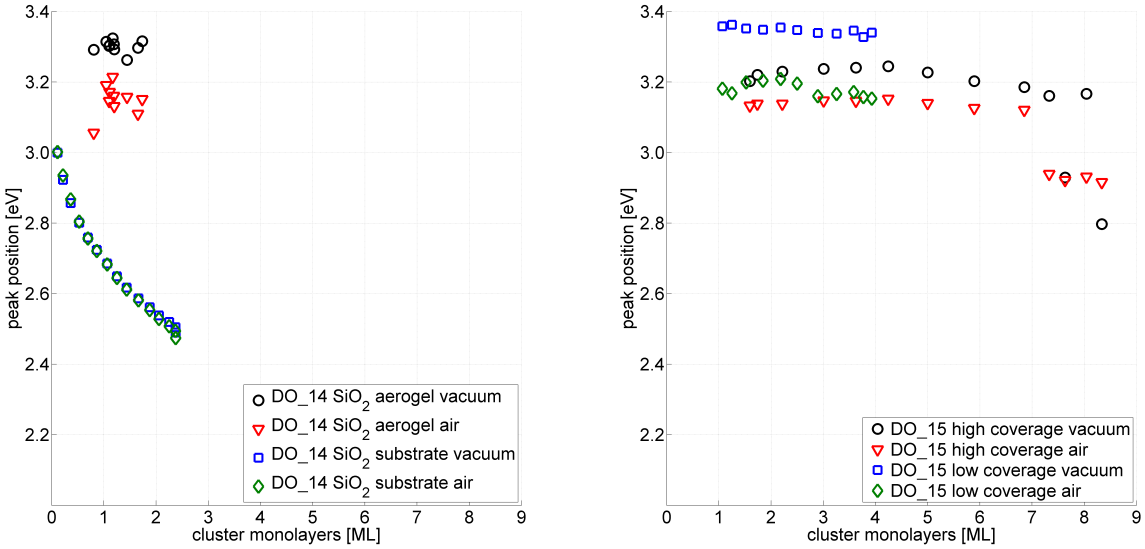

Figure 4.38: Left: Peak positions of DO_14 (in SiO_2 aerogel and on SiO_2 silica glass), right: Peak positions of DO_15 (in SiO_2 aerogel)

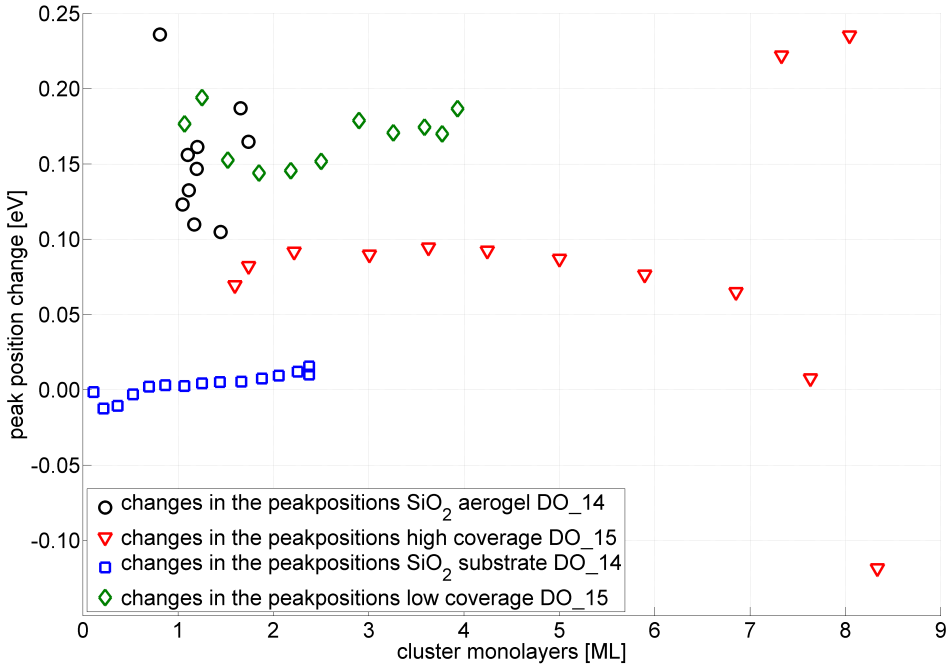

Figure 4.39: Shifts of the plasmon resonances of samples DO_14 (in SiO_2 aerogel and on SiO_2 silica glass) and DO_15 (in SiO_2 aerogel) after exposure to air.

4.2.4 Conclusions

Optical spectroscopy measurements of the plasmon resonance energy of Ag clusters on SiO_2 silica glass, in polydimethylsiloxane (PDMS) and in SiO_2 aerogel were presented in the last sections.
The data taken for sample DO_05, for which Ag clusters were deposited onto a SiO_2 silica glass substrate, show a pronounced red shift of the plasmon energy with increasing cluster coverage above 0.1 ML. This red shift is a well known consequence of electromagnetic coupling and for higher coverage the beginning cluster coalescence with a change of the axial ratio of the oblate clusters [Höv95].
Sample DO_12, which was heated prior to depositing Ag clusters onto SiO_2 silica glass to clean the surface from water monolayers, shows a similar behavior with increasing cluster coverage. As has been mentioned before, this is exactly the effect to be found for cluster distances smaller than 5R.
Comparison between the optical spectra taken in vacuum and after 60 minutes exposure to air reveals an additional red shift for both investigated samples. This additional shift can be explained with a change of the dielectric function ϵ_m of the surrounding material. Here it is clearly visible, that the cluster plasmon energies of the Ag clusters on the previously heated sample DO_12 move to significantly lower energies than for sample DO_05 ($\Delta E_{12\mathrm{max}} \approx, 0.32$ eV and $\Delta E_{05\mathrm{max}} \approx 0.23$ eV for the lowest coverage of both samples, see figure 4.16). This could be the result of partial embedding of the Ag clusters of sample DO_05 in a water matrix. Thus, the clusters are protected from the influence of the environment, in particular they are shielded against the air while the clusters are exposed to air for a period of 60 minutes, yielding a suppressed adsorption on the cluster surface compared to the clusters on the clean substrate (DO_12). The pronounced adsorption is thus the origin of the larger energy shift.
The additional energy shift after exposure to air decreases with increasing cluster coverage for both investigated samples and reaches an almost stable value above 0.2 ML of $\Delta E_{\mathrm{DO\_05}} = (0.075 \pm 0.004)$ eV and $\Delta E_{\mathrm{DO\_12}} = (0.194 \pm 0.005)$ eV, respectively.

The cluster plasmon resonance energies measured for samples DO_10 and DO_11 with Ag clusters deposited into a polydimethysiloxane (PDMS) matrix exhibit a smaller shift to lower energies with increasing cluster coverage than the previously discussed clusters on a SiO_2 substrate. This smaller peak shift is a first hint on a better separation of the clusters in the PDMS matrix compared to clusters on a flat surface such as SiO_2 silica glass. Another influence on the position of the cluster plasmon energy is the axial ratio of the investigated clusters [Höv97, Hub09].
The extinction spectra of DO_11 show a pronounced double peak structure (compare figure 4.22), which could be the result of fairly separated clusters inside the PDMS matrix and beginning coalescence of Ag clusters on the PDMS surface or at the interface of the PDMS and the SiO_2 substrate. Another aspect, which has to be accounted for, is the fact that the clusters experience an effective dielectric function ϵ_m of the surrounding material, which is a combination of PDMS (ϵ_{PDMS}=2.65) and silica glass ($\epsilon_{\mathrm{SiO_2}}$=3.75) or PDMS and vacuum. Thus, the influence of ϵ_m alters from the clusters on SiO_2 silica glass.
The resulting different axial ratios of the clusters inside the matrix, which are expected to

be nearly spherical, and on the surface could also be the source of the superposition of two extinction peaks.
Since the PDMS layers for the samples DO_10 and DO_11 have different layer thickness ((1.2±0.2)μm for DO_10 and (0.5±0.2)μm for DO_11) one could have expected differences in the additional red shift of the plasmon energy after exposure to air. But there are no significant differences with a maximum peak shift for lowest coverage of $\Delta E_{10\mathrm{max}} \approx 0.31$ eV and $\Delta E_{11\mathrm{max}} \approx 0.32$ eV for samples DO_10 and DO_11, respectively (figure 4.27). Compared to the samples on SiO_2 silica glass DO_05 and DO_12, the energy change does not reach a stable value for the Ag clusters in PDMS as seen for the clusters on the SiO_2 surface.

Ag clusters deposited into SiO_2 aerogel (samples DO_14 and DO_15) are expected to be even better separated for higher coverage than clusters in PDMS. Comparison between the extinction spectra of clusters in SiO_2 aerogel and on SiO_2 silica glass shows significant differences. In SiO_2 aerogel, the plasmon energy is positioned around approx. 3.3 eV and stays almost stable up to a coverage of approx. 1.74 ML, while for the clusters on SiO_2 silica glass a pronounced red shift can be seen for similar coverage (sample DO_14, figures 4.30 and 4.31, respectively) with a decrease of the plasmon energy from around 3.0 eV to 2.5 eV for the highest coverage of approx. 2.38 ML.
After exposure to air the cluster plasmon resonances measured for the clusters in SiO_2 aerogel are visibly broadened and the peak maximum is shifted to approx. 3.15 eV.
For the second sample DO_15 Ag clusters of even higher coverage were deposited into SiO_2 aerogel. Here, the plasmon energy stays pretty stable around 3.5 eV up to a coverage of approx. 3.93 ML (figure 4.34). For coverage above 4 ML the peak maximum stays stable as well, but there is a pronounced rise in the extinction at the low energy flank of the plasmon resonance (figure 4.35), which originates from the transition to a conducting metal film (compare figure 2.9).
After exposure to air the cluster plasmon resonance is positioned around 3.34 eV for the low coverage and around 3.25 eV for the high coverage. This stability of the plasmon energy with differing cluster coverage hints on a fairly good cluster separation up to very high coverage.

The full width at half maximum (FWHM) of the extinction spectra is directly influenced by chemical interface damping. For the samples with Ag clusters on SiO_2 silica glass an increase of the FWHM after exposure to air can be seen for both samples (DO_05 and DO_12, figure 4.18). With increasing cluster coverage the influence of the chemical interface damping decreases. Thus, the change in the FWHM decreases with increasing cluster coverage.
The full width at half maximum of the extinction measured for clusters in PDMS (samples DO_10 and DO_11) decreases with increasing coverage (figure 4.28). But, other than for the clusters on SiO_2 silica glass, it increases again above a particular threshold, which seems to depend on the PDMS layer thickness. This could be a result of the superposition of clusters with different ratio and has to be investigated further to determine the origin of the double peak structure. For both investigated samples exposure to air yields an increase of the FWHM (figure 4.29).
For the investigated SiO_2 aerogel samples the determination of the FWHM is difficult due to impurities resulting in deformed extinction spectra for sample DO_14 (figure 4.30) and

the transition to a conducting metal for high coverage of sample DO_15 resulting in a pronounced increase of the extinction in the region of the low energy flank. Thus, it should only be stated that a slight broadening of the spectra taken for Ag clusters in SiO_2 aerogel after exposure to air is visible and subject to further investigations.

4.3 Results - X-ray Absorption Near Edge Structure Spectroscopy (XANES)

X-ray absorption near edge structure spectroscopy provides interesting information in particular on the electronic structure and the oxidation state of the element under investigation. Due to the element specific absorption it is well suited to determine whether there is an oxide forming at the surface of the cluster or not. An oxide formation could explain the additional red shift of the cluster plasmon resonances after exposure to air as previously explained in section 4.2. The samples investigated in the framework of this thesis are very dilute due to the fact that the point of interest is the electronic structure of well separated clusters. Thus, on a SiO_2 silica glass substrate only cluster coverage up to approx. 0.1 ML yields the absorption spectra of separate small clusters.
In the following sections all presented x-ray absorption spectra are convolved with a Gaussian function with a FWHM of 1 eV. In the diploma thesis of Kamil Latussek could be shown, that the errors originating from such a convolution are negligible [Lat11]. Additionally, the shown errorbars function as an instrument to determine "true" structural features in the spectra (since they could also well be a result of the convolution).

4.3.1 Proof of principles and Ag L_3 absorption edge

In very first measurements at BL8, DELTA, Dortmund, XANES spectra at the Ag L_3 absorption edge were taken for Ag clusters deposited on SiO_2 silica glass, Ag clusters deposited into PDMS and Ag clusters deposited into SiO_2 aerogel. During this first experiment it was important to determine the feasibility of an x-ray absorption near edge structure spectroscopy experiment on a dilute sample such as separate Ag clusters on a SiO_2 silica glass surface. Therefore, the previously discussed cluster sample DO_05 (on SiO_2 silica glass) and two samples, which were not previously discussed in this thesis, one of which is Ag clusters in PDMS and the other one is Ag clusters in SiO_2 aerogel were investigated. These two samples with clusters in matrices were very first samples prepared as proof of principles for the possibility to deposit a higher amount of separate clusters than on SiO_2 silica glass. Figure 4.40 shows first XANES spectra of the Ag L_3 edge measured for a high and a low coverage in SiO_2 aerogel, for Ag clusters in PDMS and for the reference samples Ag (100 nm film) and Ag_2O (powder). Therefore, the Ag_2O powder was spread on sticky tape and then positioned on the sample holder. The high sensitivity of XANES to changes in the oxidation state of the investigated element is clearly visible in the comparison between the two reference samples.
The pronounced white line of the Ag_2O XANES signal at the onset of the absorption edge is a result of transitions to free final d states [Beh92a] as has been previously explained.
Regarding the cluster signals it is clearly visible that neither the clusters in SiO_2 aerogel nor the clusters in PDMS show a considerable amount of silver oxide. A comparison between the silver reference signal and the cluster measurements shows significant differences, which can thus be assigned to a size effect or particularly, a change of the axial ratio of the oblate clusters. With increasing cluster coverage the L_3 absorption edge becomes more similar to the Ag reference measurement.

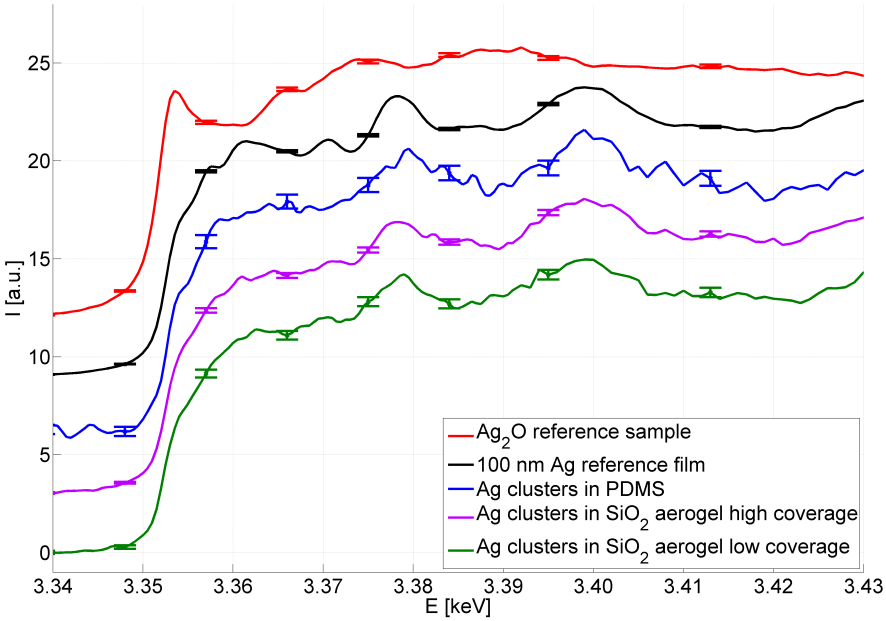

Figure 4.40: Ag L_3 edge measured at a high and low coverage of a sample with clusters in SiO_2 aerogel, at Ag clusters in PDMS, a 100 nm Ag reference film and a Ag_2O reference sample (powder) measured at BL8, DELTA, Dortmund.

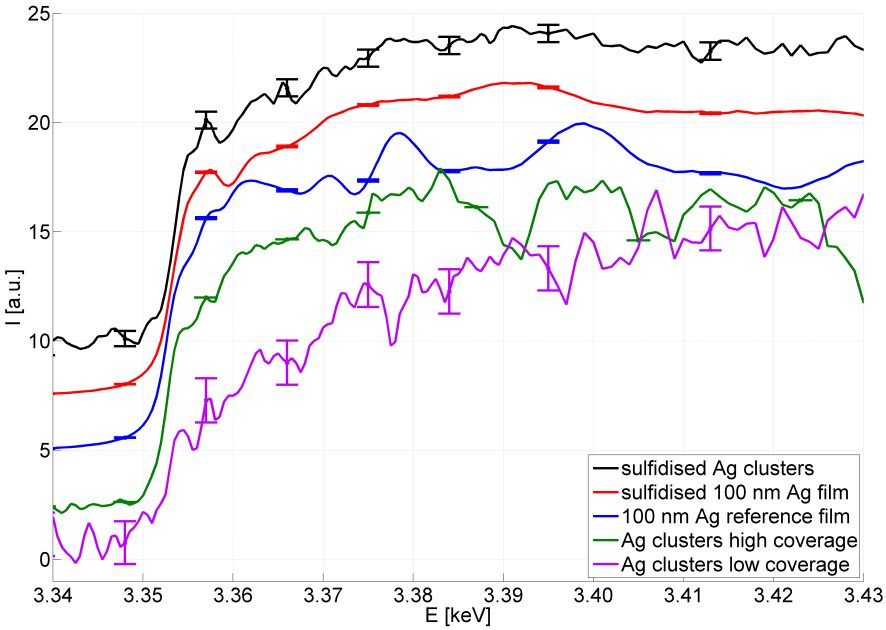

Figure 4.41: Ag L_3 edge of a high and low coverage of a sample with clusters in SiO_2 aerogel, of a 100 nm Ag reference film, a sulfidised 100 nm Ag reference film and sulfidised Ag clusters measured at BL8, DELTA, Dortmund.

In another experiment a cluster sample with Ag clusters on SiO_2 silica glass was transformed to silver sulfide by exposure to H_2S gas. As has been shown via optical spectroscopy in previous experiments Ag clusters react with sulfur very quickly and the cluster plasmon resonance vanishes after a short exposure time [Höv95]. Additionally a 100 nm Ag film was sulfidised to be able to compare the absorption edge of a bulk reference to the cluster signal.
Figure 4.41 shows the XANES measurements of a high and a low Ag cluster coverage on a SiO_2 substrate, a 100 nm Ag reference film and a sulfidised 100 nm Ag reference film as well as a sulfidised cluster sample.
A comparison of the Ag reference film and the sulfidised Ag film shows remarkable changes with a small white line appearing at the onset of the absorption edge of the sulfidised Ag film. The Ag clusters exhibit the above mentioned size dependent changes in the absorption edge features. The Ag L_3 absorption edge measured at the sulfidised Ag clusters shows significant similarities to the sulfidised Ag reference film in particular in the region around the white line of the sulfidised Ag film.
Thus, it is possible to determine a change of the oxidation state for a Ag cluster sample and a partial oxidation should be detectable.
After being able to prove the feasibility of XANES experiments on the dilute cluster samples investigated in the framework of this thesis in further experiments the previously discussed cluster samples DO_11 (Ag clusters in PDMS) and DO_15 (Ag clusters in SiO_2 aerogel) were investigated at BL8, DELTA, Dortmund, by measuring the Ag L_3 absorption edge. For these samples with a comparably high cluster coverage the signal to noise ratio was enhanced compared to Ag clusters on SiO_2 silica glass. Thus, possible changes in the oxidation state of the clusters should be detectable.
Figure 4.42 shows Ag L_3 edges measured at two different coverages of DO_11 and a 100 nm Ag reference film.
While the high coverage of approx. 1.12 cluster monolayers in PDMS resembles the reference signal measured at a 100 nm Ag film, there are small visible changes in the spectrum for the lower coverage of 0.73 ML in the energy region directly above the absorption edge (3.36-3.37 keV). In particular the structure at approx. 3.369 keV disappears. This hints at the fact that the clusters in PDMS are better separated than on a SiO_2 silica glass surface even for higher coverage.
Figure 4.43 shows x-ray absorption near edge spectra of the Ag L_3 absorption edge taken at sample DO_15 for three different amounts of Ag clusters in SiO_2 aerogel compared to a 100 nm Ag reference film.
For the lowest coverage of approx. 1.85 ML the features around the onset of the absorption edge are visibly flattened (approx. 3.36-3.37 keV), in particular the structure at approx. 3.369 keV. Yet, no detectable amount of oxide formation can be seen. For increasing coverage up to 3.93 ML the absorption spectra of the Ag clusters in aerogel become more similar to the Ag reference film signal. A direct comparison to Ag clusters in PDMS (see figure 4.42) clearly shows, that by using SiO_2 aerogel as matrix material it is possible to separate even more clusters than in the PDMS matrix.
These first experimental results served as a foundation for XANES measurements of the Ag L_2 and Ag L_1 absorption edges performed at beamline ID26, ESRF, Grenoble, France for clusters on SiO_2 silica glass and in PDMS. The results are presented in the following section.

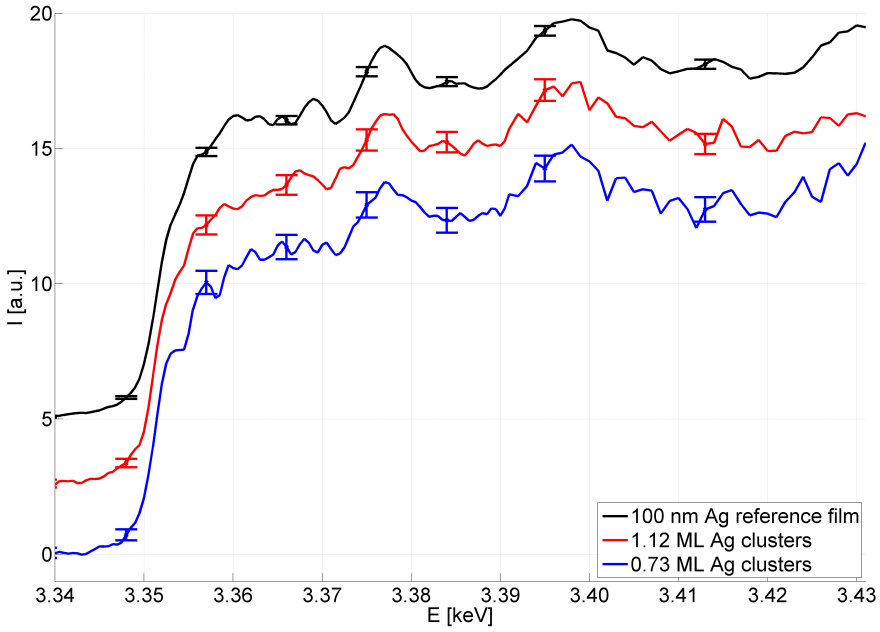

Figure 4.42: Ag L_3 edge of a high and low coverage of DO_11 with clusters in PDMS and a 100 nm Ag reference film measured at BL8, DELTA, Dortmund.

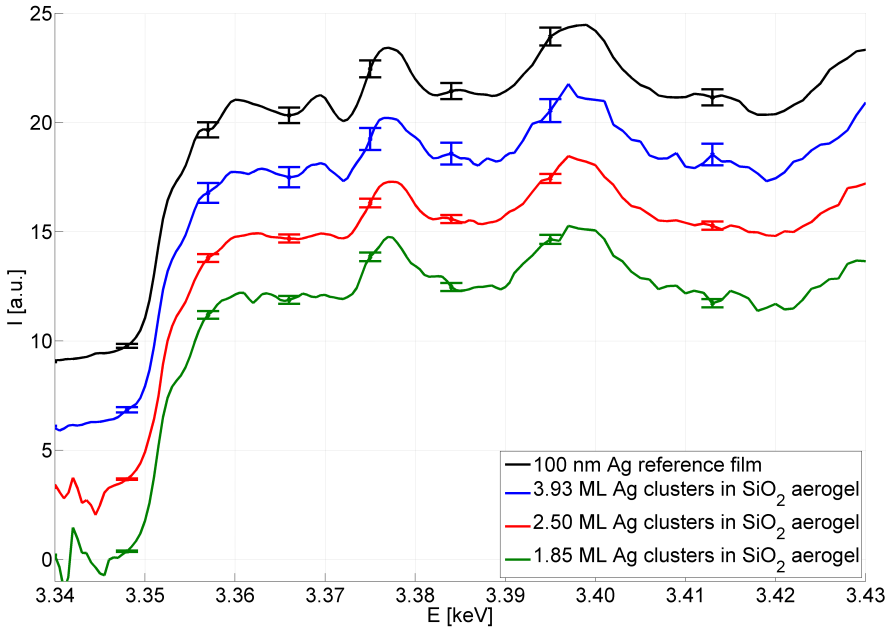

Figure 4.43: Ag L_3 edge of three different coverages of DO_15 with clusters in SiO_2 aerogel and a 100 nm Ag reference film measured at BL8, DELTA, Dortmund.

4.3.2 Ag L_2 absorption edge

In the framework of a diploma thesis the previously discussed samples DO_05 with Ag clusters on SiO_2 silica glass as well as DO_10 and DO_11 with Ag clusters in a PDMS matrix were investigated at beamline ID26, ESRF, Grenoble, France, using x-ray absorption near edge structure spectroscopy (XANES) [Lat11]. The cluster samples were transported to the European Synchroton Radiation Facilities in a vacuumized desiccator and then measured in air.
The presented reference samples are 100 nm Ag films on SiO_2 silica glass as well as Ag_2O and AgO pellets, which were produced by mixing the oxidic powders with cellulose in a ratio of 1:1 and pressing them in a hydraulic press.
During the first measurements of the Ag L_2 absorption edge of Ag clusters on SiO_2 silica glass (sample DO_05) with a scan time of approx. 5 minutes a clearly visible energy shift of the absorption edge combined with the formation of a white line at the onset of the absorption edge could be observed (see figure 4.44). Comparison of these radiation damage induced changes to reference spectra taken at a Ag_2O and a AgO pellet shows, that after 3 scans of 5 minutes each at a coverage of approx. 0.8 cluster monolayers on SiO_2 substrate the absorption energy and thus, the edge position is already shifted to lower energy resembling the absorption spectrum of the AgO pellet. Here, the clusters obviously react with the oxygen in the surrounding air. A reduction of scan time to 60 seconds per scan yielded a decrease of radiation damage induced by the x-ray beam as can be seen in figure 4.45, but still an oxide formation could be detected for a coverage of approx. 0.9 cluster monolayers. Here, the energy shift seems to be smaller within the limits of the error than for scan time of 5 minutes and the resulting spectrum after 3 scans shows significant similarities to the Ag L_2 absorption edge of the Ag_2O pellet.
Regarding the findings on the cluster sample, additional 5 minute scans were taken on the 100 nm Ag reference film to determine possible radiation damage even on the bulk-like silver. The spectra taken at the reference sample are shown in figure 4.46. A clear oxidation can be seen after 3 scans, 5 minutes each, which manifests in a shift of the absorption energy to slightly lower energies. A subsequently installed device to flush the sample with nitrogen (N_2) did not yield remarkable reduction of the damage.
The embedded clusters in the PDMS matrix of samples DO_10 and DO_11 did not show any oxidation induced by the illumination and possible heat up process induced by the highly intense x-ray beam. This fact can be explained with the PDMS matrix surrounding the Ag clusters. It seems to be a good protection against possible reaction partners such as oxygen in the surrounding air.
After these findings the scanning procedure was modified such that not only the scan time was reduced, but for each investigated sample position the x-ray beam and thus the focus on the sample was moved horizontally on a straight line. Within this scanning line the cluster coverage changes only slightly. Vertically the focus was moved about 2 mm maximum. Thus, the change in cluster coverage of the investigated region still stays negligible.

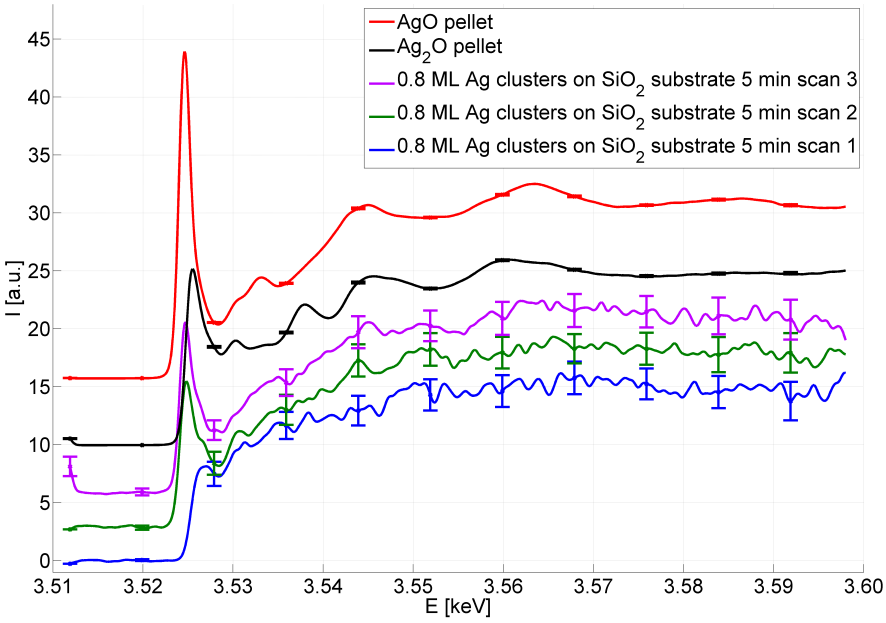

Figure 4.44: Radiation damage of approx. 0.8 ML Ag clusters on SiO_2 silica glass. Each of the shown spectra had a scanning time of 5 minutes.

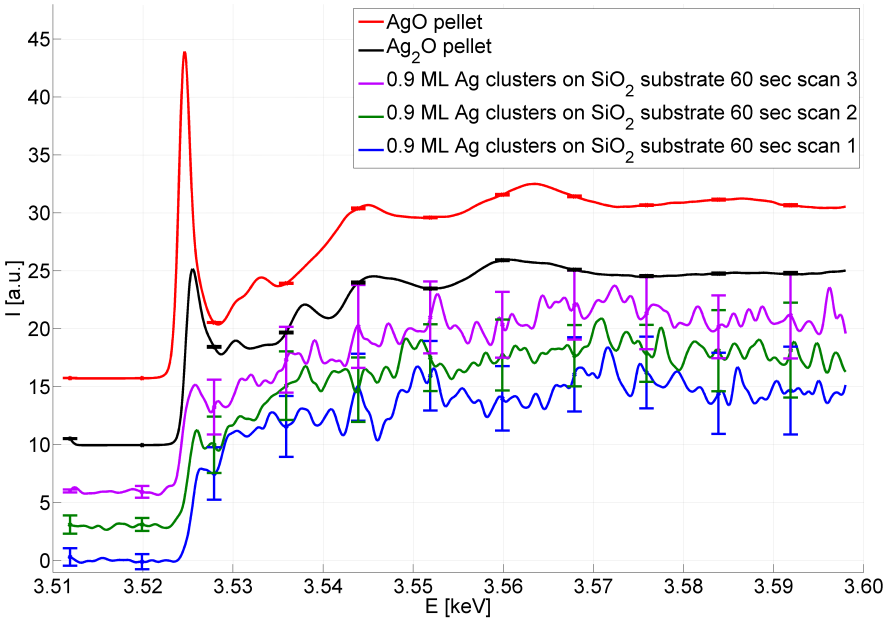

Figure 4.45: Radiation damage of approx. 0.8 ML Ag clusters on SiO_2 silica glass. Each of the shown spectra had a scanning time of 60 seconds.

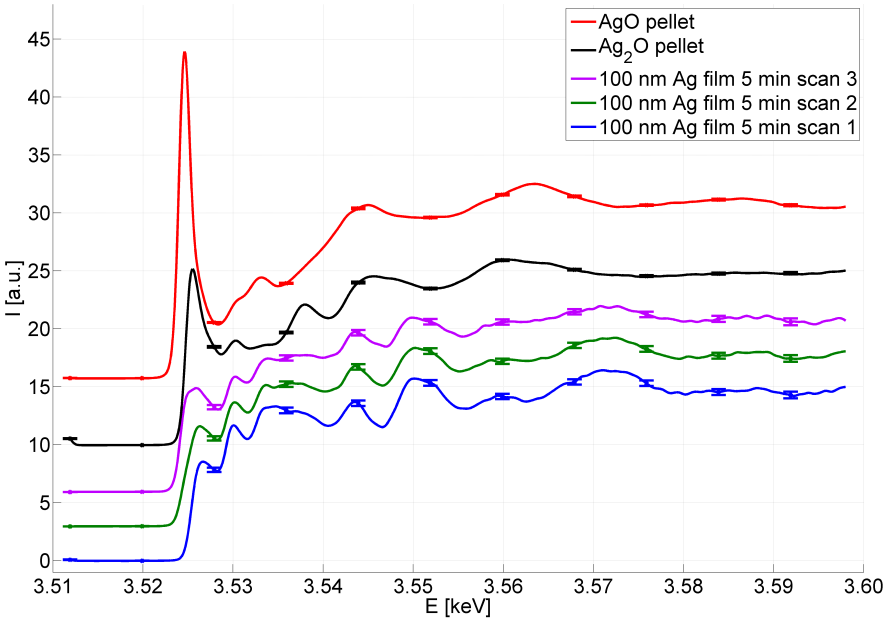

Figure 4.46: Radiation damage of the 100 nm Ag reference film. Each of the shown spectra had a scanning time of 5 minutes.

X-ray absorption spectra of the Ag L_2 absorption edge of Ag clusters on SiO_2 silica glass taken for different cluster coverages are shown in figure 4.47 compared to the Ag_2O pellet reference scan and in figure 4.48 compared to the 100 nm Ag reference film data. First thing to notice is, that there are no similarities between the Ag L_2 signal of the Ag clusters and the oxide reference sample independent of the cluster coverage. Thus, within the limits of the error there is no significant amount of oxide on the cluster surface as could be assumed by a red shift of the plasmon resonance after exposure to air (compare section 4.1.1). Comparison to the 100 nm Ag reference film with a bulk-like crystal structure shows a clear size effect (figure 4.48). While the absorption spectrum of a cluster coverage of approx. 1.0 cluster monolayers shows most of the features, which can be found in the reference spectrum, the absorption edge of a much lower coverage of approx. 0.17 ML shows significant differences.
For the higher coverage on SiO_2 silica glass there is a pronounced formation of larger islands on the surface, which results in the bulk similar absorption edge. This is in good agreement with the red shift of the plasmon energy for such high coverage. Although the here investigated lowest coverage of 0.17 ML already showed a red shift in the optical spectroscopy measurements, there are distinct differences to the absorption of bulk-like silver. This difference in the energy density is likely related to the different structure and next-neighbor distances in the small clusters. With increasing coverage, the absorption edge structure becomes more similar to the Ag reference spectrum, which clearly hints on cluster aggregation and island formation for the highest coverage.

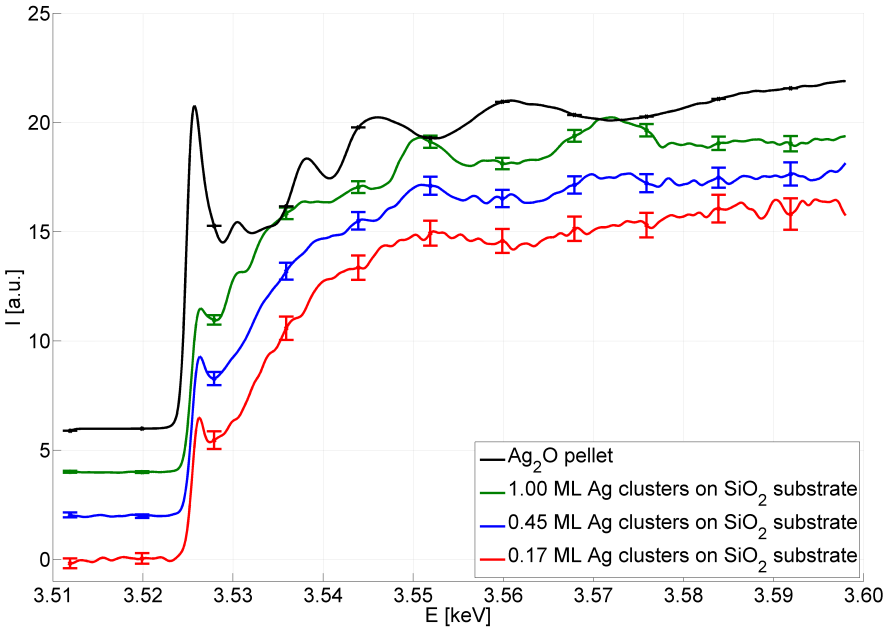

Figure 4.47: Ag L_2 absorption edge measured for different cluster coverage of Ag clusters on SiO_2 silica glass (sample DO_05) compared to Ag L_2 absorption edge of a Ag_2O pellet measured ad ID26, ESRF, Grenoble, France.

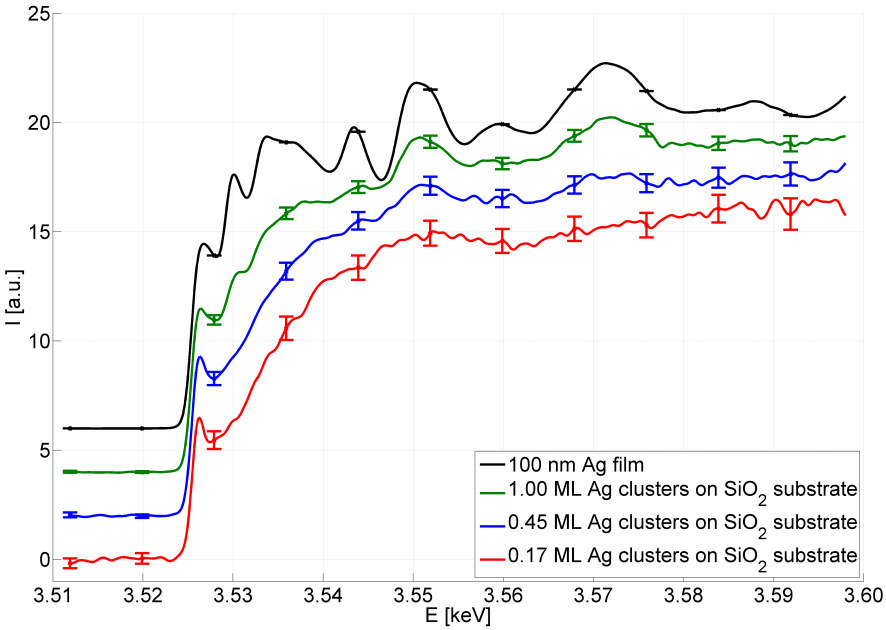

Figure 4.48: Ag L_2 absorption edge measured for different cluster coverage of Ag clusters on SiO_2 silica glass (sample DO_05) compared to Ag L_2 absorption edge of a 100 nm Ag film measured at ID26, ESRF, Grenoble, France.

The second sample system investigated at the ESRF, Grenoble, France, is Ag clusters embedded in a PDMS matrix. The measured XANES spectra of the Ag L_2 absorption edge for different cluster coverages compared to the Ag_2O pellet reference measurement and the 100 nm Ag film reference measurement are shown in figures 4.49 and 4.50, respectively.
Directly obvious is the absence of oxide on the cluster surface. The Ag L_2 absorption edge spectra taken for Ag clusters of different coverage in the PDMS matrix show no similarities to the Ag L_2 reference spectrum measured at the Ag_2O pellet. The size dependent differences in the cluster spectra are more definite by comparison to the Ag reference measurement in figure 4.50.
Here, the effect of cluster coalescence with increasing cluster coverage is showing in the formation of silver bulk-like structures especially in the energy region between the onset of the absorption edge and approx. 3.55 keV. For very low coverage such as 0.09 ML and 0.20 ML there is a peak forming at an energy of approx. 3.533 keV, which is not showing in the absorption spectra of clusters on SiO_2 silica glass (see figure 4.48). Even for the lowest coverage of 0.17 ML clusters on SiO_2 silica glass there is no such peak forming. This feature could be a result of the different shape of the clusters in PDMS compared to clusters on SiO_2, where the clusters are expected to be oblate. Another explanation could be the influence of the PDMS matrix. The matrix material could change the unoccupied density of states and thus, the form of the absorption spectrum.
Nevertheless, there are remarkable differences between the Ag reference sample's Ag L_2 absorption edge and the cluster sample at a comparably high coverage of approx. 1.20 ML and even 2.00 ML. The clusters seem to be better separated inside the PDMS matrix than on the SiO_2 silica glass surface, which is the proposed effect of embedding clusters into a matrix.
The growing similarities to the Ag reference signal with increasing cluster coverage can directly be assigned to coalescence of the Ag clusters to bigger agglomerates and thus, to the development of bulk-like structures.

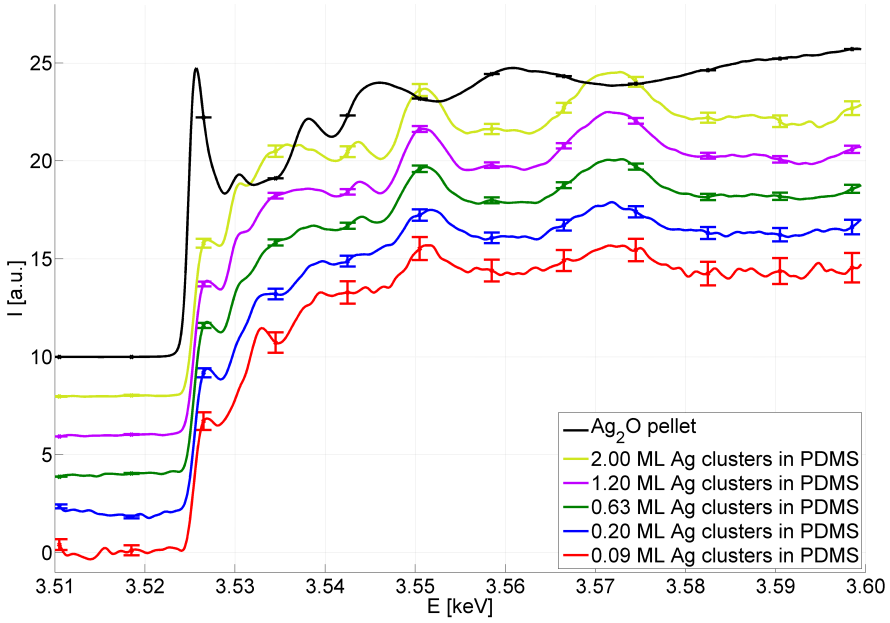

Figure 4.49: Ag L_2 absorption edge measured for different cluster coverage of Ag clusters in PDMS (sample DO_11) compared to Ag L_2 absorption edge of a Ag_2O pellet.

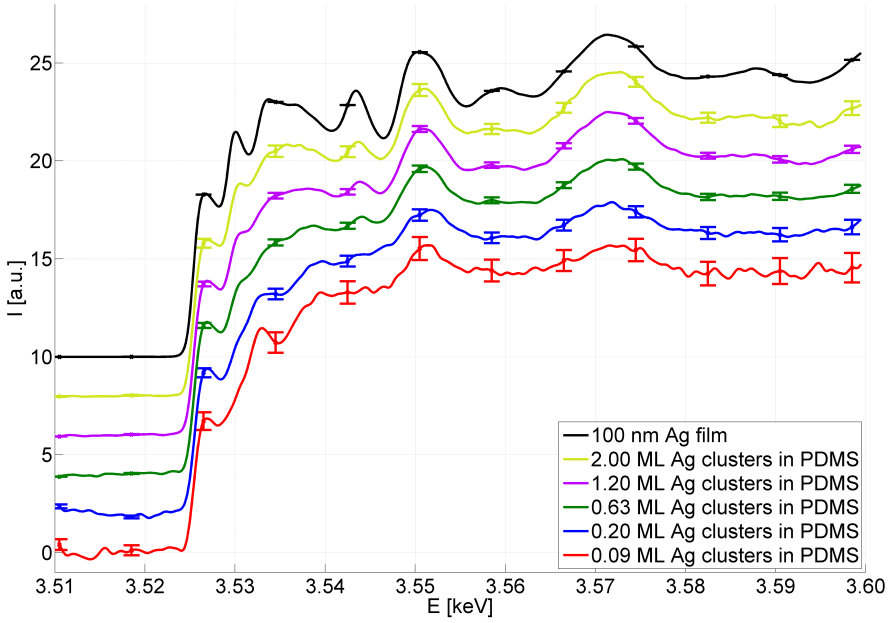

Figure 4.50: Ag L_2 absorption edge measured for different cluster coverage of Ag clusters in PDMS (sample DO_11) compared to Ag L_2 absorption edge of a 100 nm Ag film.

4.3.3 Ag L_1 absorption edge

Other than for the L_2 and L_3 absorption edges, the L_1 absorption edge does not result from excitations of 2p electrons but from excitations of 2s electrons to unoccupied states. Since the absorption probability is much lower than for the 2p electrons, a certain amount of cluster material is essential to gain a suitable signal to noise ratio.
Thus, only measurements of the cluster samples DO_10 and DO_11 with Ag clusters in a PDMS matrix were successful. The measured x-ray absorption near edge spectra compared to the Ag_2O reference and the Ag reference spectra are presented in figures 4.51 and 4.52, respectively.
Despite the relatively large error, there are obviously no similarities to the Ag_2O pellet's Ag L_1 absorption edge. Comparison to the Ag L_1 reference spectrum measured at a 100 nm Ag film with bulk crystal structure hints on a present size effect. The absorption spectrum of the lowest coverage of approx. 0.2 cluster monolayers exhibits slight differences in the energy region directly above the absorption edge and up to approx. 3.83 keV. Here, the pronounced structures of the Ag reference signal are flattened. However, due to the large error bars the differences are at the detection limit.
With increasing coverage the observed structural details of the Ag bulk absorption edge start to develop.
In the energy region above 3.83 keV there seems to be no size dependent change at all. This is in contrast to the behavior for the L_2 and L_3 absorption edge (compare sections 4.3.2 and 4.3.1).

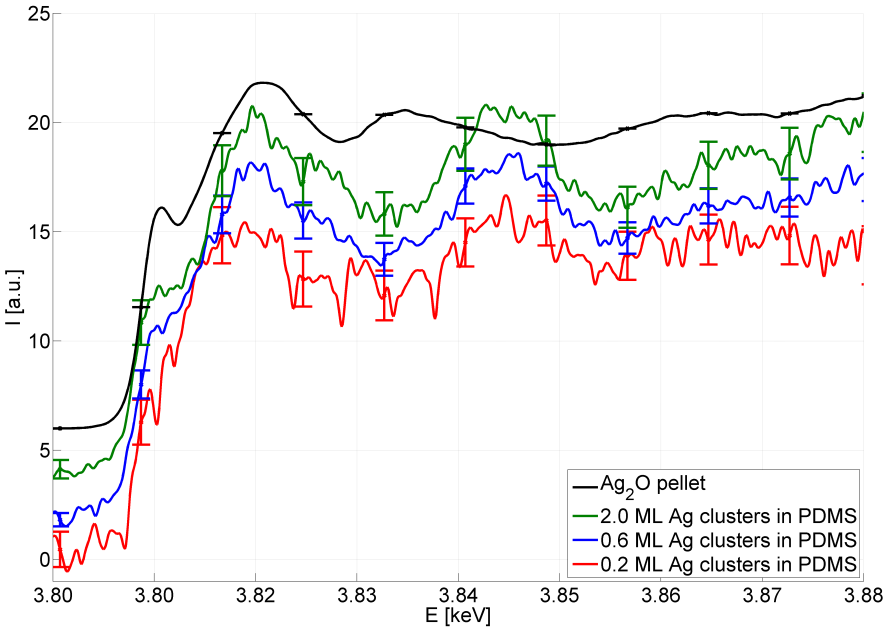

Figure 4.51: Ag L_1 absorption edge measured for different cluster coverage of Ag clusters in PDMS (sample DO_11) compared to Ag L_1 absorption edge of a Ag_2O pellet.

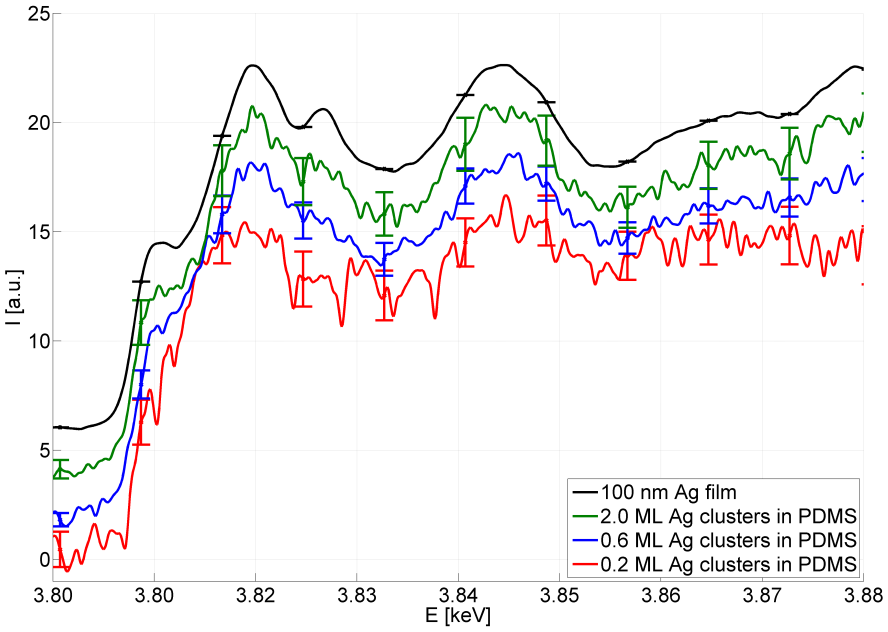

Figure 4.52: Ag L_1 absorption edge measured for different cluster coverage of Ag clusters in PDMS (sample DO_11) compared to Ag L_1 absorption edge of a 100 nm Ag film.

4.4 Calculations with FEFF

In the previous sections the x-ray absorption near edge structure (XANES) spectroscopy measurements of the Ag L absorption edges of Ag clusters on SiO_2 silica glass, in a polydimethylsiloxane (PDMS) matrix and in SiO_2 aerogel were compared to reference spectra taken at bulk silver (100 nm Ag film), different oxides (AgO pellet and Ag_2O pellet) and a silver sulfide (Ag_2S). To further investigate how structural differences between the clusters' structure and silver bulk crystal structure, such as number of next neighbors and next-neighbor distance influence the shape of the L absorption edge, first ab-initio calculations were performed utilizing the software package FEFF9 [Reh00, Reh10].
For the performed calculations cluster structures determined by Huang et al. for Ag clusters with 141 to 310 atoms were used [Hua11]. In their approach the interaction between the silver atoms was modeled by the Gupta potential [Gup81]. The thus calculated cluster structure was then transformed into coordinate files for the different cluster sizes.
The necessary parameters for calculations with FEFF9 are not only the coordinates of the cluster's atoms but also the absorbing atom has to be defined as well as the region around the absorbing atom, in which full multiple scattering (FMS) should be considered. In principle, to determine the absorption spectrum of a whole cluster calculations for each atom of the cluster have to be performed. The cluster absorption edge is then a superposition of all single spectra for each absorbing atom in the cluster. For a cluster with approx. 250 silver atoms as investigated in the framework of this thesis it would thus be inevitable to calculate 250 single spectra, each of them highly demanding with respect to CPU time.

In a first approach to calculate the Ag L XANES spectra for a certain cluster the highly symmetric so called geometrically magic Ag_{147} cluster was chosen. This cluster with 147 atoms arranges in a Mackay icosahedral form [Mac62]. A visualization of the cluster can be found in figure 4.53. Each of the so called coordination shells consists of atoms, which differ from each other with respect to the number of next neighbors and the next-neighbor distance.
In the framework of a bachelor's thesis first considerations were made about reducing the number of calculations to be performed for a cluster [Mül12]. By determining the distances of one atom in the cluster to every other atom it was possible to group the atoms of the cluster according to their number of next neighbors and distances. The coordinate files of [Hua11] do not assume a strictly symmetrical geometry for the 147 atom clusters, but resemble the calculated ground state. However, it could be confirmed, that atoms with equal neighbor distances and number of next neighbors have the same XANES spectra (figure 4.54). Thus, by determining the amount of atoms with equal distance distribution it is possible to minimize the calculation time. For the highly symmetric Ag_{147} cluster the number of atoms, for which single absorption spectra have to be calculated, can be reduced from 147 to 7. In figure 4.53 atoms with similar next-neighbor distances and thus, similar absorption spectra are visualized by the use of matching colors. In the following sections the calculated absorption spectra are colored corresponding to the color of the absorbing atom in figure 4.53.
Figure 4.55 shows the distances as determined for the innermost atom 1 to all other atoms in the Ag_{147} cluster. Clearly visible the atoms can be divided into three coordination shells

around the central atom containing 12, 42 and 92 atoms, respectively.
For clusters with lower symmetry grouping the atoms by neighbor distances only is not sufficient enough to really reduce calculation time. For comparison the axially symmetric cluster Ag_{192} was also examined. The distances of the central atom (atom 1) to all other atoms of the cluster are depicted in form of a histogram in figure 4.56. For this histogram distances, which are accurate to two decimal places (0.01 Å) are considered equal. This is due to visualization limitations. To determine the number of atoms, for which to calculate single absorption spectra, distances accurate to three decimal places are considered equal. By taking the distance to the central atom as sole filter attribute the number of calculations to be performed can be reduced to 21 individual atoms. A picture of the axially symmetric Ag_{192} cluster can be found in figure 4.57. Here, equally colored atoms represent atoms with equal distance from the central atom.
Figure 4.58 shows the absorption spectra as calculated for the 21 different atoms in the Ag_{192} cluster. It displays the spectra from the innermost atom 1 at the bottom up to the outermost atom on the edges of the surface (atom 21) at the top. Regarding the structural features directly above the absorption edge (3.52-3.54 keV), there are spectra belonging to atoms with differing distances to the central atom, which nevertheless look quite similar. It would be of great advantage to be able to sort these similar looking spectra in advance to further reduce CPU time needed to calculate the XANES absorption spectrum of this Ag_{192} and asymmetric clusters. In contrast to the icosahedral Ag_{147} cluster, for which it is easy to distinguish between different coordination shells, additional filter attributes such as e.g. coordination angles to next-neighbors could help to further reduce calculation time.
Figure 4.59 shows a direct comparison of the calculated x-ray absorption near edge structure of the Ag L_2 absorption of the icosahedral Ag_{147} cluster and the axially symmetric Ag_{192} cluster. Both were calculated by adding up the 7 (21) spectra for Ag_{147} (Ag_{192}) weighted according to their frequency in the cluster. The pronounced similarities between these two clusters are not surprising, since the size of the clusters and the fraction surface atoms to inner atoms of the cluster do not alter significantly. The influence of the surface atoms on the shape of the absorption edge will be discussed in detail in section 4.4.2.

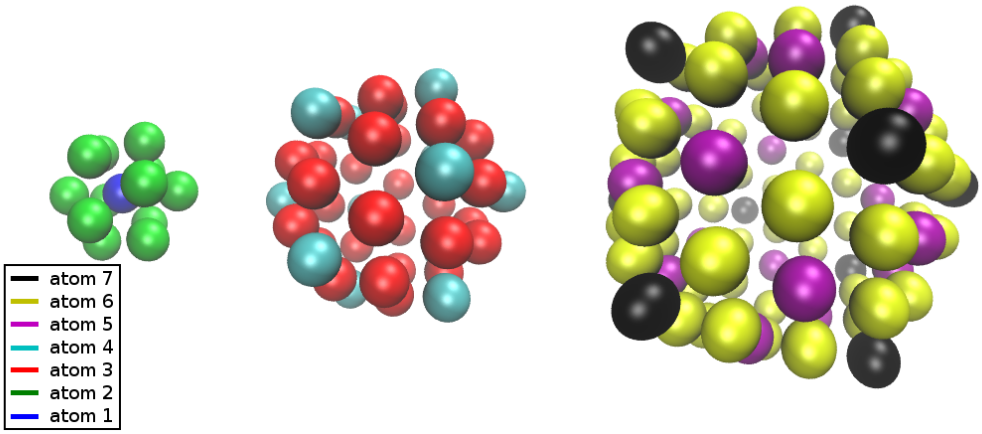

Figure 4.53: Structure of the highly symmetric icosahedral Ag_{147} cluster. Left: Inner atom and first shell, middle: Second shell, right: Third shell. Visualization with VMD [Hum96].

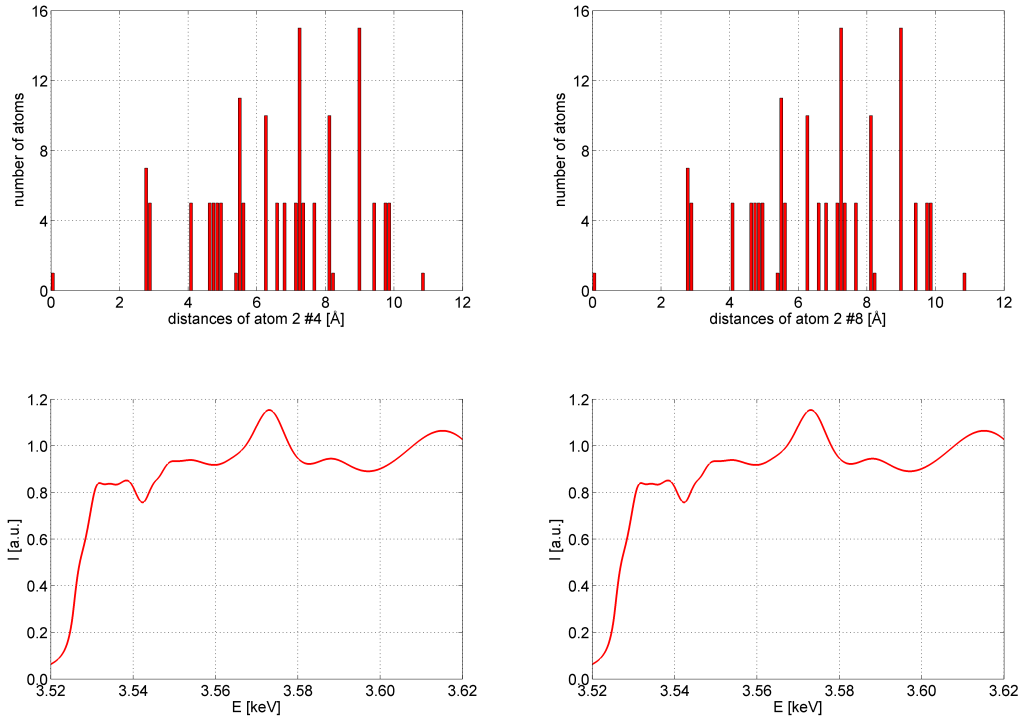

Figure 4.54: Comparison between two different atoms in the first shell (atom 2). Top: Histograms of the distances of atom 2 to every other atom in the cluster, bottom: Calculated XANES spectra of the two atoms (atom 2) in the first shell.

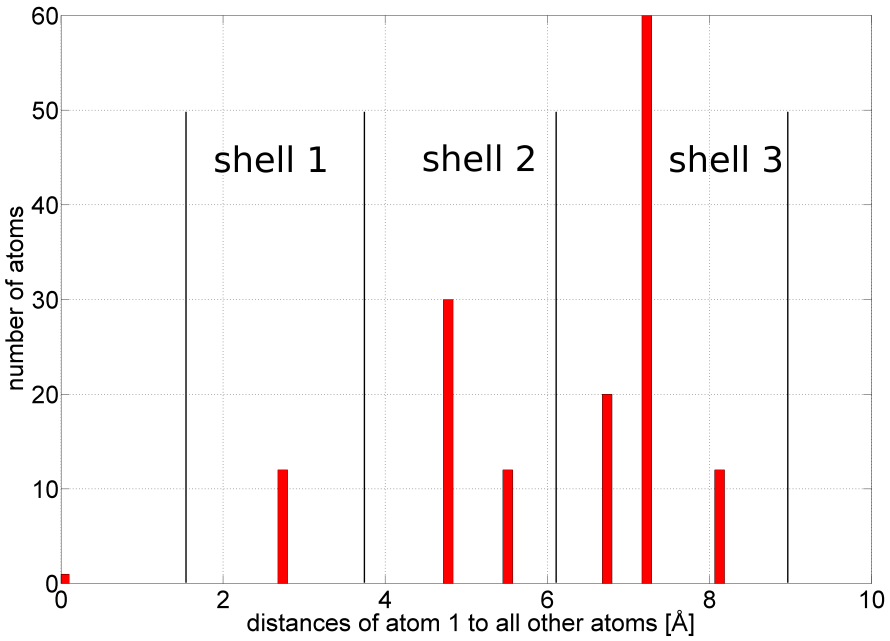

Figure 4.55: Distances of the central atom (atom 1) of the highly symmetric icosahedral Ag_{147} cluster to all other atoms of the cluster. Additionally, the corresponding coordination shells are depicted.

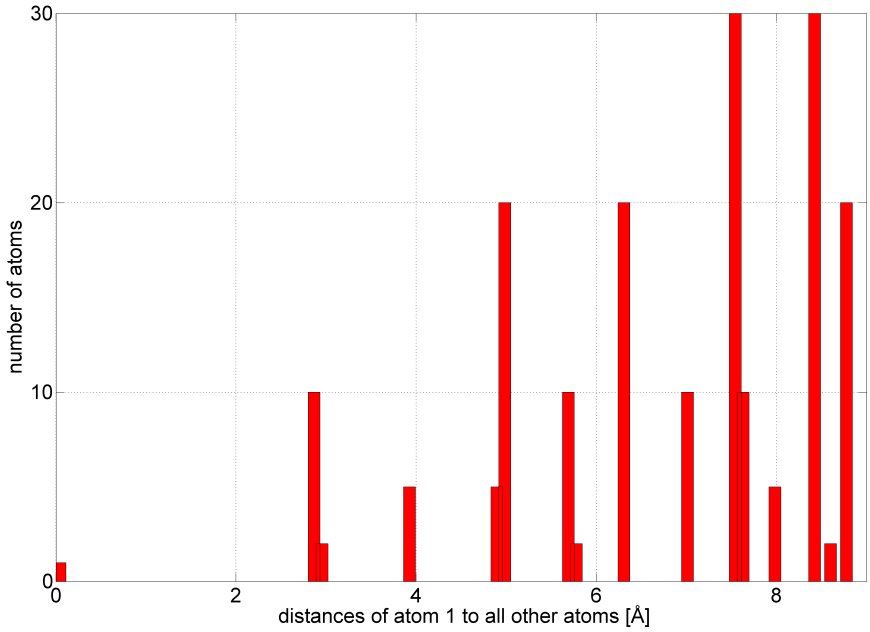

Figure 4.56: Distances of the central atom (atom 1) of the Ag_{192} cluster to all other atoms of the cluster.

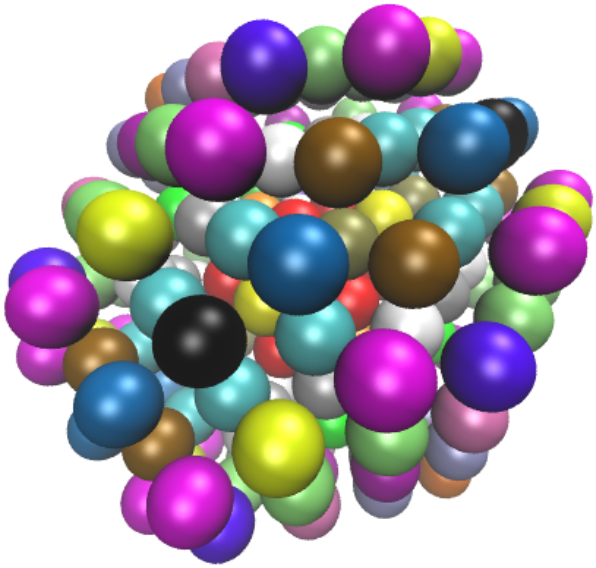

Figure 4.57: Structure of the axially symmetric Ag_{192} cluster visualized with VMD [Hum96].

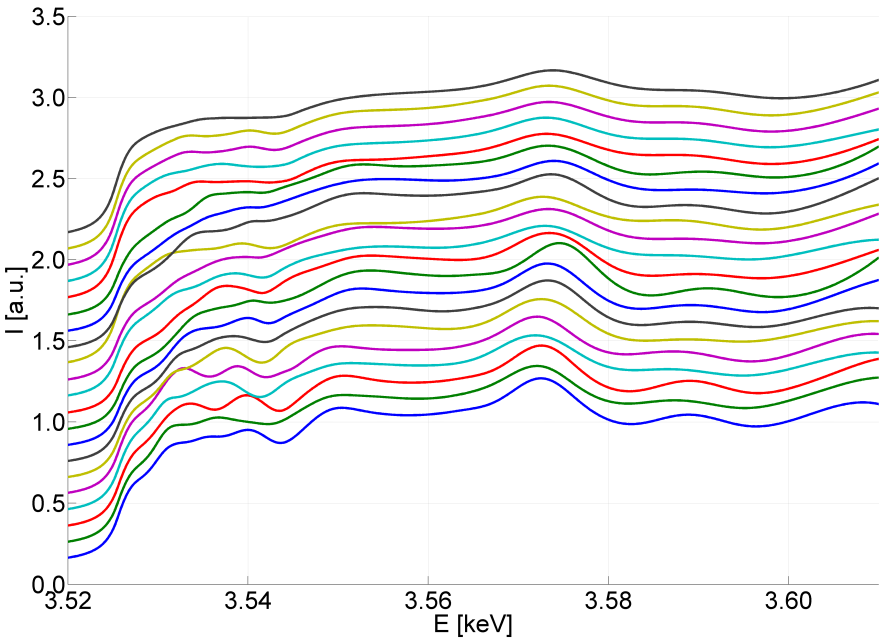

Figure 4.58: Calculated XANES Ag L_2 absorption spectra for each of the 21 atoms with different distance to the central atom. It displays the absorption of atom 1 to atom 21 from bottom to top.

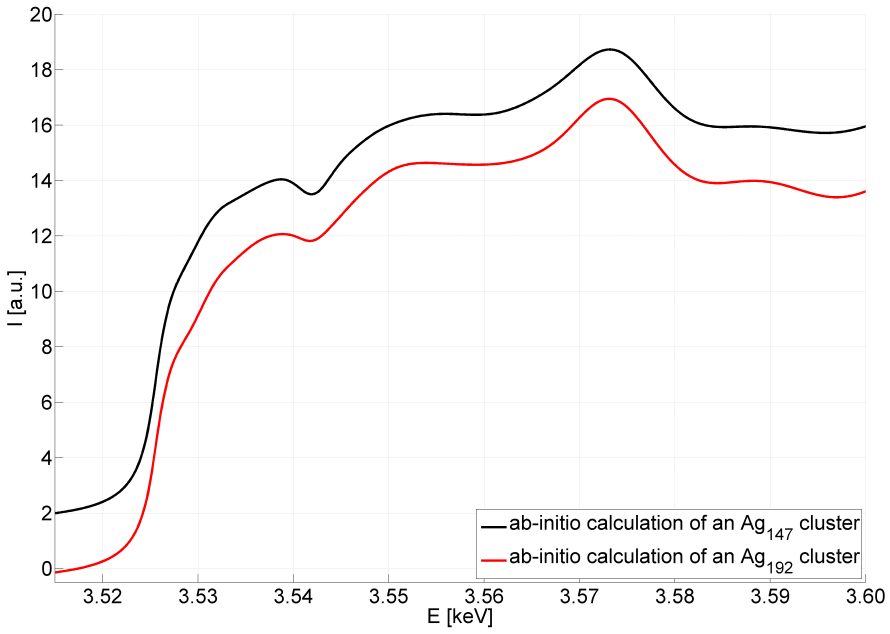

Figure 4.59: Calculated XANES Ag L_2 absorption spectra for the icosahedral Ag_{147} cluster compared to the calculated XANES Ag L_2 absorption edge of the axially symmetric Ag_{192} cluster.

4.4.1 Ag L_3 absorption edge

The Ag L_3 XANES spectra as calculated for the highly symmetric Ag_{147} cluster are depicted in figure 4.60. Most pronounced are the structural changes from the spectrum of the innermost atom (atom 1) to the atoms in the outer shell (atom 5, atom 6, atom 7). The numerous structural features of the absorption spectrum of atom 1 can be explained with the comparably large number of next neighbors (12 next neighbors) and a relatively small next-neighbor distance of 2.73 Å. Here, the structures are quite similar to the structural features found for the 100 nm Ag reference film (see figure 4.40 and the following figure 4.62). Obviously, the number of structural features, being a direct result of full multiple scattering processes, decreases with decreasing number of neighbors and thus, the number of possible scatterers. Here, not only next neighbors count but also the associated coordination shell. Remarkably, the spectra of all atoms, which form one shell show the same structural features. This hints on a possibility to approximate the calculated spectra particularly for asymmetric clusters yielding a reduction of CPU time.
While the spectra for different coordination shells alter significantly right above the Ag L_3 absorption edge, the peak around 3.4 keV changes only slightly. There is some broadening for the outer shell atoms and a shift, which can be assigned to slight changes in the mean next-neighbor distances of the absorbing atom, which can be found in table 4.2 and in figure 4.61. Particularly the next-neighbor distance of the innermost atom is significantly altered with respect to the next-neighbor distance of 2.89 Å found for bulk Ag.
A comparison between the calculated Ag L_3 absorption edge of the Ag_{147} cluster, the calculated Ag L_3 absorption edge of bulk silver and XANES measurements of the Ag L_3 absorption edge taken at a 100 nm Ag film and Ag clusters of different coverage in PDMS can be seen in figure 4.62. For the Ag_{147} cluster signal the single spectra are added up weighted with their frequency in the cluster. Although the calculations do not match the measurements precisely, there are remarkable similarities. Where the structures of the Ag reference signals are numerous especially between approx. 3.355-3.700 keV, the structures in this energy region directly above the absorption edge of the ab-initio calculation of the cluster are flattened. This is in good agreement with the measured XANES signal for the clusters in PDMS.
Since the investigated clusters at a coverage of 0.73 ML or even 1.12 ML in PDMS already show a tendency to coalesce, the differences between the measured cluster spectra and the calculated Ag L_3 XANES signal for the Ag_{147} are not surprising. This subject will be investigated further in the following section.
A closer look on the peak around 3.4 keV in figure 4.62 shows a remarkable trend. While the peak structure of the calculated cluster signal lies slightly above 3.4 keV, this structure is found below 3.4 keV for the calculated and measured Ag bulk signal as well as for the measured cluster absorption spectra. As already mentioned above the fluctuations in the peak position of this particular feature in the single atom spectra calculated for the Ag_{147} cluster as depicted in figure 4.60 are related to slight changes in the mean next-neighbor distance of the absorbing atom, even if the next-neighbor distance shows a distribution as shown in table 4.2 and figure 4.61. Thus, the small deviation of this peak position compared to the measured Ag reference signal and the calculated XANES spectrum for bulk silver with a fcc crystal structure clearly hints on next-neighbor distances in the

cluster comparable to bulk silver next-neighbor distance.
This structural difference to the cluster coordination file as determined by Huang et al. [Hua11] for free Ag clusters could be a result of the PDMS matrix, which influences the structure and form of the deposited clusters.

	number of next neighbors	mean next-neighbor distance [Å]
atom 1	12	2.73±0.00
atom 2	12	2.83±0.05
atom 3	12	2.86±0.07
atom 4	12	2.82±0.06
atom 5	9	2.89±0.04
atom 6	8	2.87±0.07
atom 7	6	2.81±0.06

Table 4.2: Number of next neighbors and their mean next-neighbor distance for atoms with equal distance distribution to the central atom of Ag_{147} [Mül12].

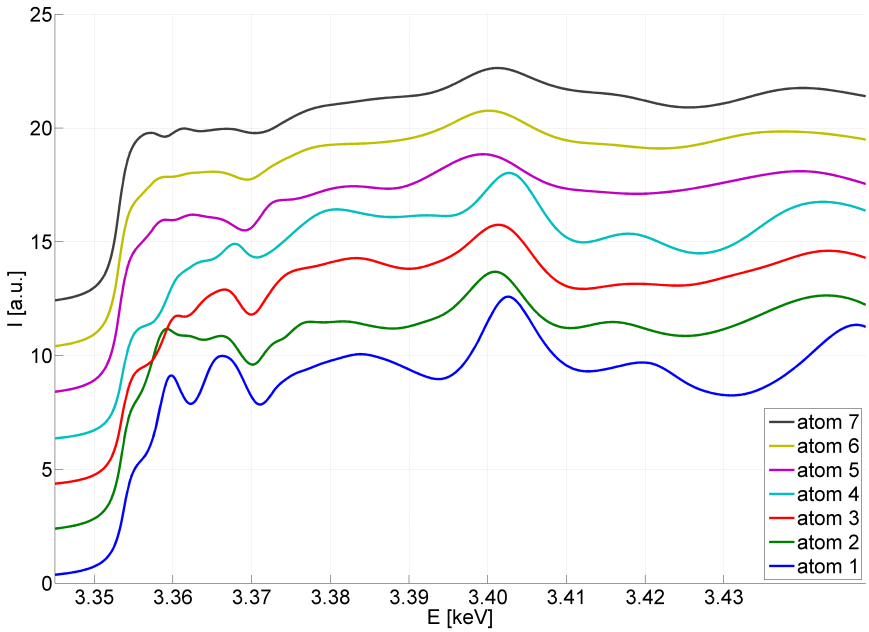

Figure 4.60: Calculated Ag L_3 XANES spectra of the Ag_{147} cluster (calculation done with FEFF9). Here, spectra for each of the different Ag atoms are shown individually.

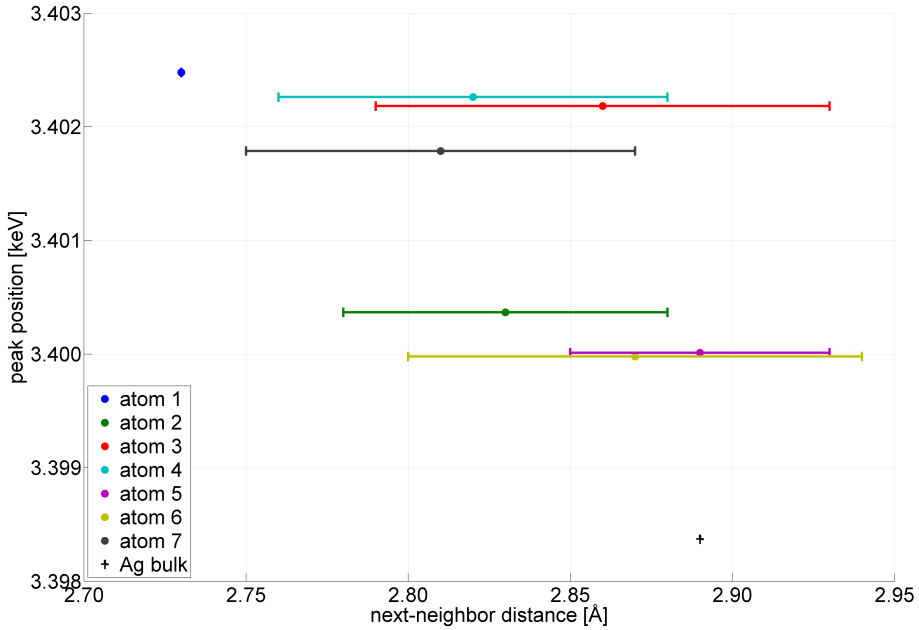

Figure 4.61: Peak positions around 3.4 keV with respect to the mean next-neighbor distance and the standard deviation of distance distribution of the data from [Hua11] for the 7 atoms of the Ag_{147} cluster and the Ag bulk calculation as denoted in table 4.2.

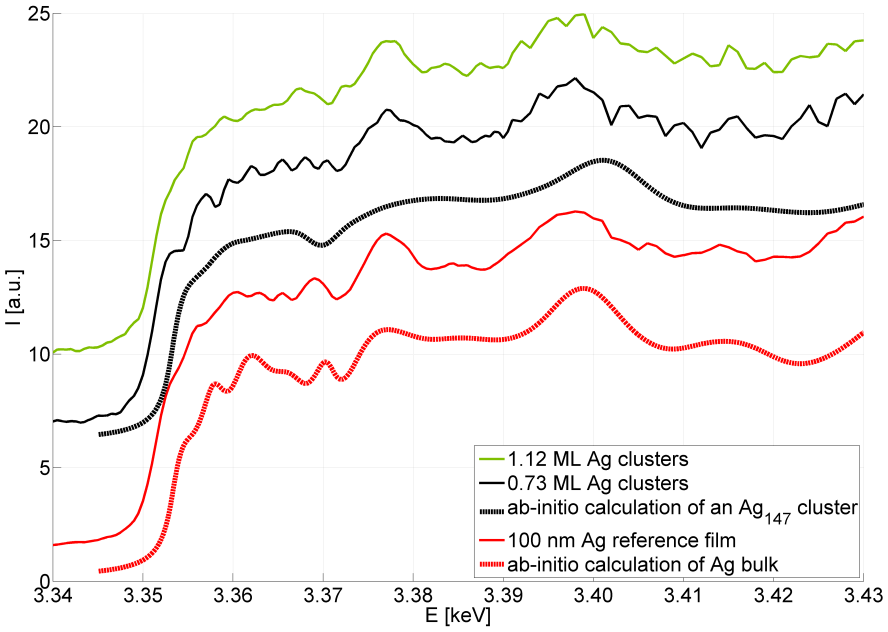

Figure 4.62: Comparison between the cluster Ag L_3 XANES measurements taken for clusters of different coverage in PDMS, a 100 nm silver film reference, a calculated silver bulk XANES spectrum and the Ag L_3 absorption edge as calculated for a Ag_{147} cluster.

4.4.2 Ag L_2 absorption edge

The XANES spectra of the Ag L_2 absorption edge as calculated for the seven individual absorbing atoms of the Ag_{147} cluster can be found in figure 4.63. As already seen for the Ag L_3 absorption edge the spectra of atoms, which can be assigned to one of the three coordination shells, look very similar, particularly directly above the absorption edge (energy region approx. 3.53-3.54 keV). The pronounced structural features found in the absorption spectrum of the innermost atom are directly related to the high number of next neighbors and number of surrounding coordination shells and thus, to the pronounced multiple scattering occurring in the absorption process. With decreasing number of next neighbors and coordination shells the number of structural features in the absorption edge decreases.
The high similarity to the absorption spectra calculated for the Ag L_3 absorption edge is unsurprising since the only difference in the x-ray absorption process between the L_2 and the L_3 absorption edge is the spin of the excited electrons ($2p_{1/2}$ and $2p_{3/2}$, respectively).
A comparison between the calculated absorption spectra of the Ag_{147} cluster, a Ag reference and the experimental data taken at ID26, ESRF, Grenoble, for Ag clusters in PDMS, a 100 nm Ag reference film and a Ag_2O pellet is depicted in figure 4.64. While the calculated XANES signal of the silver reference and the measured silver reference spectrum are in good agreement for most of the visible features the experimentally determined XANES spectrum exhibits even more structural details. This is a direct result of the partial fluorescence yield (PFY) method used at ID26, ESRF, Grenoble, to measure the absorption edges. Therefore, the absorption edge is measured by fixing $\hbar\omega_2$ to the maximum of the fluorescence line (compare section 2.3.2). The advantage is, that the background signal is this low that more structural features can be detected than with total fluorescence yield (TFY), in which the integrated energy over $\hbar\omega_2$ is measured. A slight disadvantage is the comparability to the calculated FEFF9 TFY spectra yielding the explanation for the better agreement between the calculations of the Ag L_3 absorption edge and the measured spectra, which were taken in TFY (figure 4.62).
Particularly the peak slightly above 3.53 keV in the Ag L_2 XANES spectrum of the 0.09 ML clusters in PDMS cannot be explained with the calculations and thus, not with the geometrical structure of the cluster, either. However, the trend, which is the decrease of structural features due to decreased multiple scattering probability can be seen for the measured and the calculated cluster signals. A comparison to the oxide signal shows no similarities to the calculated spectra whatsoever.
A closer look on the measured Ag L_2 absorption edge of clusters with different coverage in PDMS (sample DO_11) in comparison with the XANES Ag L_2 signal of a 100 nm silver film reveals an interesting evolution of the spectral features with increasing cluster coverage (figure 4.65). As already seen before (compare figure 4.50) the absorption spectrum of the clusters more and more resembles the silver reference signal with increasing coverage. Figure 4.65 reveals, that the spectra for cluster coverage of 0.20, 0.63, 1.20 and 2.00 ML might be a superposition of the absorption spectrum of the silver reference sample (100 nm film with face centered cubic (fcc) structure) and the XANES signal measured for the lowest coverage of 0.09 ML Ag clusters, where the clusters are expected to have a mean diameter of approx. 2 nm and thus, a comparably high surface atoms to bulk atoms fraction. This can be seen in the existence of fixed cross-over points in the obtained spectra. For

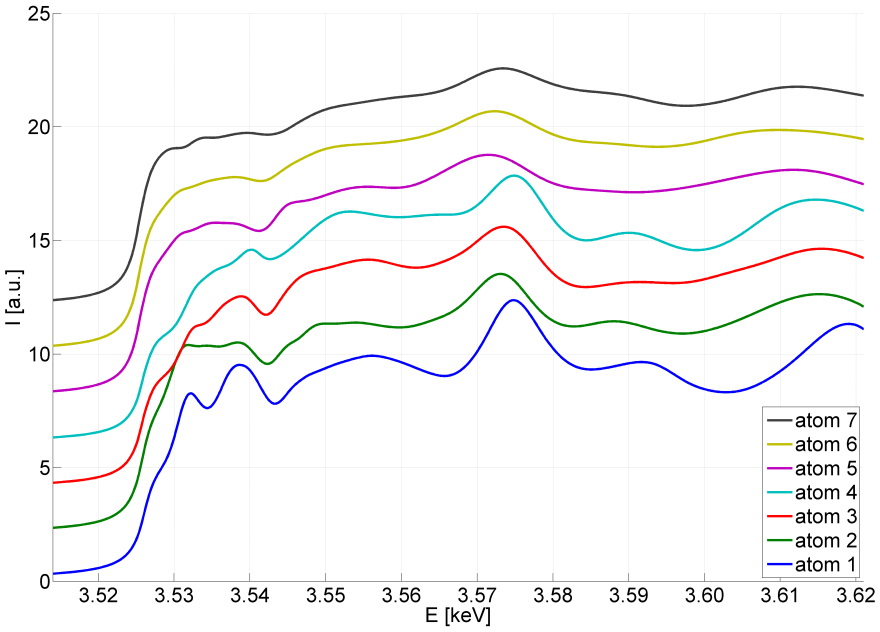

Figure 4.63: Calculated Ag L_2 XANES spectra of the Ag_{147} cluster (calculation done with FEFF9). Here, spectra for each of the different Ag atoms are shown individually.

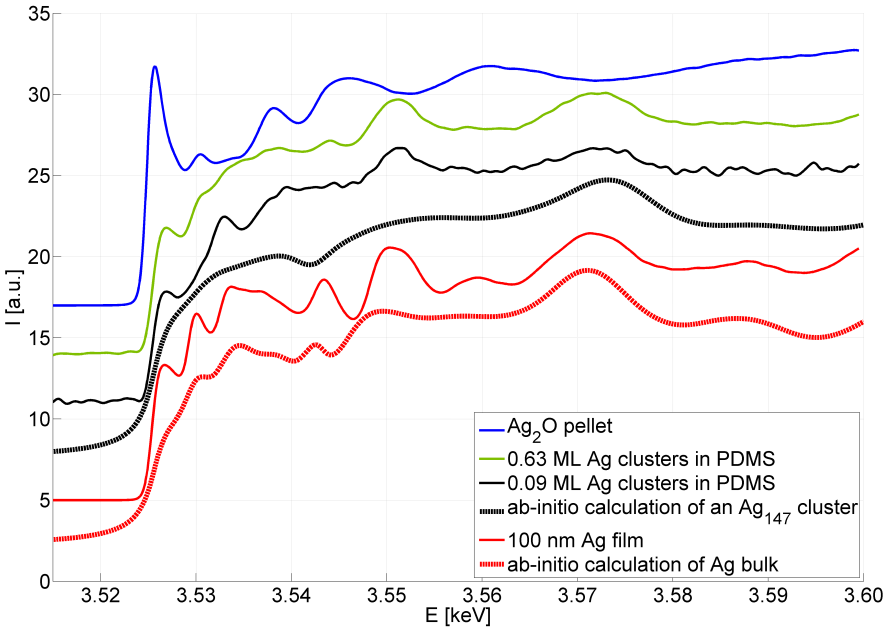

Figure 4.64: Comparison between the cluster Ag L_2 XANES measurements taken for clusters of different coverage in PDMS, a 100 nm silver film reference, a calculated silver bulk XANES spectrum and the Ag L_2 absorption edge as calculated for a Ag_{147} cluster.

a superposition of the absorption signal of the Ag reference film for the bulk-like features and the XANES signal measured for the lowest cluster coverage (0.09 ML) these cross-over points stay stable.
Figure 4.66 shows a first attempt to simulate the evolution of the measured XANES spectra for different cluster coverage by combining the XANES signal measured for the 100 nm Ag reference film and the 0.09 ML Ag cluster signal. It has to be stated, that this can only be an approximation since the cluster signal used to function as the surface atoms signal is already a result of a whole cluster with mean diameter of 2 nm consisting of surface atoms and inner atoms. Nevertheless, the superpositions of both spectra (denoted A and B in the figure) with different surface to bulk fractions (here, the cluster signal is taken as an approximation of the pure surface atoms) show significant similarities to the cluster signals measured for different coverage in PDMS (compare figure 4.65).
A second attempt to prove the conjecture of the cluster signals being a direct result of superposition of the absorption signal seen for surface atoms and bulk atoms can be found in figure 4.67. Here, the calculated Ag L_2 XANES signals of atoms 5, 6 and 7 are summed up weighted to form the signal of the surface atoms B and the calculated absorption signal of bulk silver A is used to simulate the cluster signals. For comparison reasons the same fractions of surface atoms to bulk atoms are used to calculate superpositioned spectra for different cluster sizes. Remarkably, the measured spectra as shown in figure 4.65 show two pronounced features at approx. 3.55 keV and around 3.575 keV, which stay stable for the bulk signal and the cluster spectra. These features can also be found in the calculated superpositions on figure 4.67.
An attempt to simulate the measured cluster signals by combining the calculated spectra of the outer coordination shell of the cluster and the spectrum of the innermost atom (atom 1) used as bulk signal A is shown in figure 4.68. For comparison reasons the same fractions of surface atoms to bulk atoms are used to calculate superpositioned spectra for different cluster sizes. Other than for the calculated bulk silver signal the prominent feature around 3.55 keV can not be simulated by this superposition and the peak structure around 3.575 keV shows a pronounced shift to lower energies with increasing surface fraction. This is in contrast to the measured spectra confirming the considerations for the Ag L_3 absorption edge about the cluster structure, in particular the atom-atom distances, in PDMS being more bulk-like than proposed by the calculated structures in [Hua11] as already discussed in section 4.4.1.
For an estimation of the mean cluster size present in the investigated coverage in figure 4.65 the fraction of the surface atoms to the inner atoms of a silver cluster with specific radius is depicted in figure 4.69. Here, two different approximations are considered: for the dots N_{surf}/N_{bulk} is estimated by $N_{surf}/(N\text{-}N_{surf})$, where $N_{surf}=A_{cluster}/A_{atom}$ with $A_{atom}=3.46\ r^2$ (with the atom radius of silver r=0.1445 nm) and $A_{cluster}=4\pi R^2$ [Höv00]. N is calculated by $N=V_{cluster}/V_{atom}$ with $V_{cluster}=(4/3)\pi R^3$ and $V_{atom}=5.66r^3$ (assuming fcc packing of the atoms). This approximation holds only for large clusters failing for small clusters e.g. R=0.5 nm, where N≈31 and $N_{surface}$ ≈43 and thus, $N_{surface}>N$ and $N_{surface}/N_{bulk}<0$.
For the smaller clusters the icosahedral Mackay clusters with hexagonally packed surface facets are considered. These clusters with fivefold symmetry represent an energetically optimized structure with the so called magic numbers N_k and k being the number of atom shells around the central atom (see figure 4.70). Therefore, the triangles are calculated by

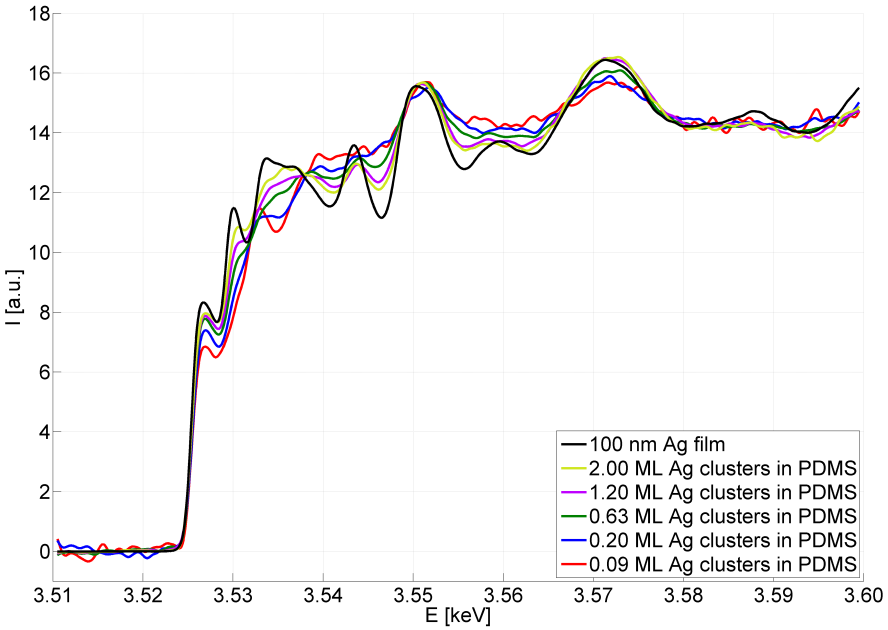

Figure 4.65: Ag L_2 absorption edge measured for different cluster coverage of Ag clusters in PDMS (sample DO_11) compared to Ag L_2 absorption edge of a 100 nm Ag film.

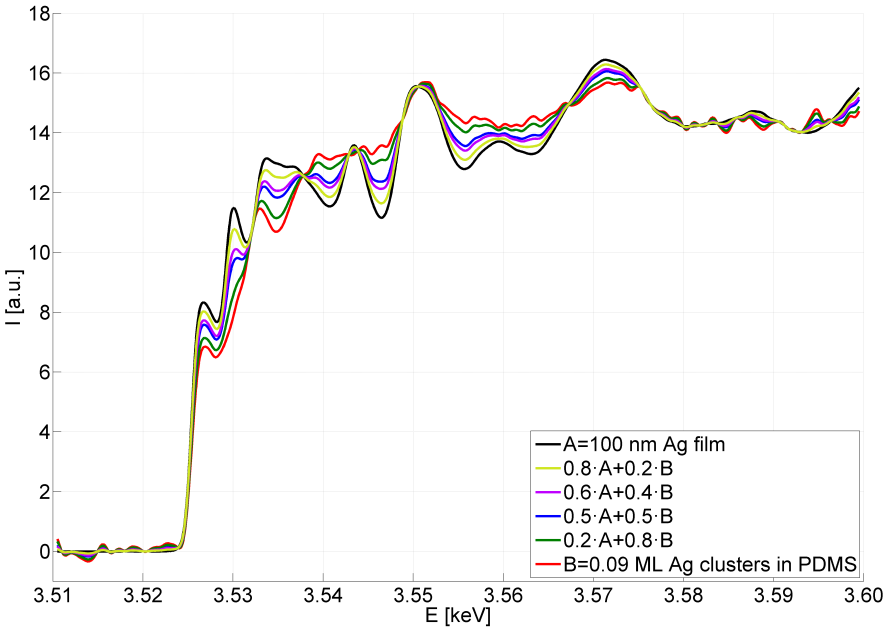

Figure 4.66: Superposition of the Ag L_2 absorption spectra measured for 0.09 ML Ag clusters in PDMS and a 100 nm Ag film to simulate different surface atoms to bulk atoms fractions.

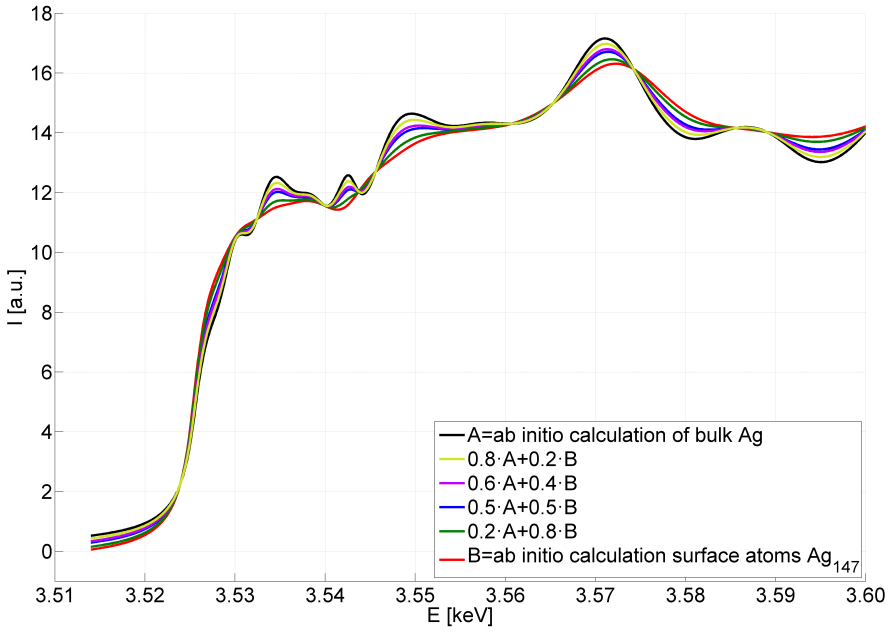

Figure 4.67: Superposition of the calculated absorption spectrum for bulk silver and the outer coordination shell of the Ag_{147} cluster.

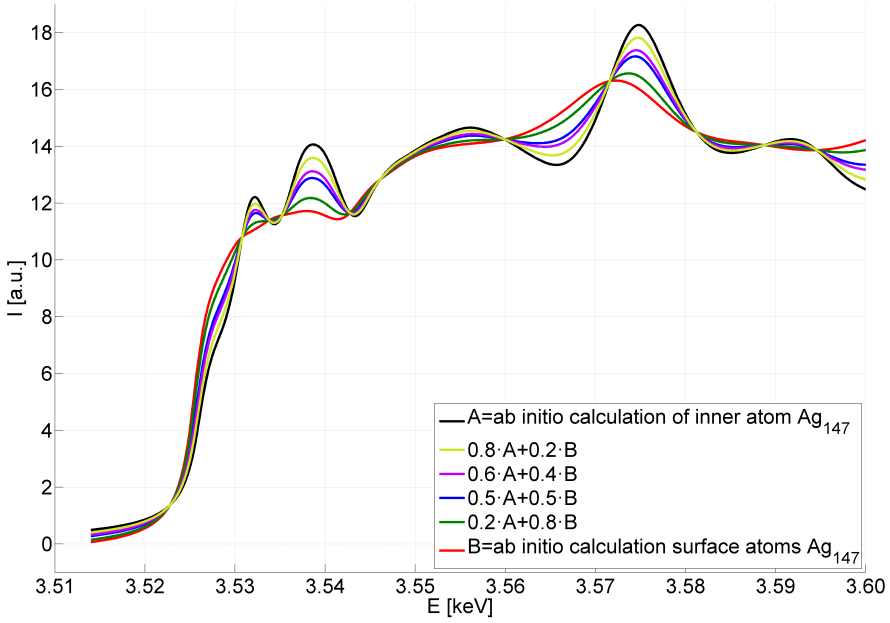

Figure 4.68: Superposition of the calculated absorption spectrum for the inner atom of the Ag_{147} cluster and the outer coordination shell of the Ag_{147} cluster.

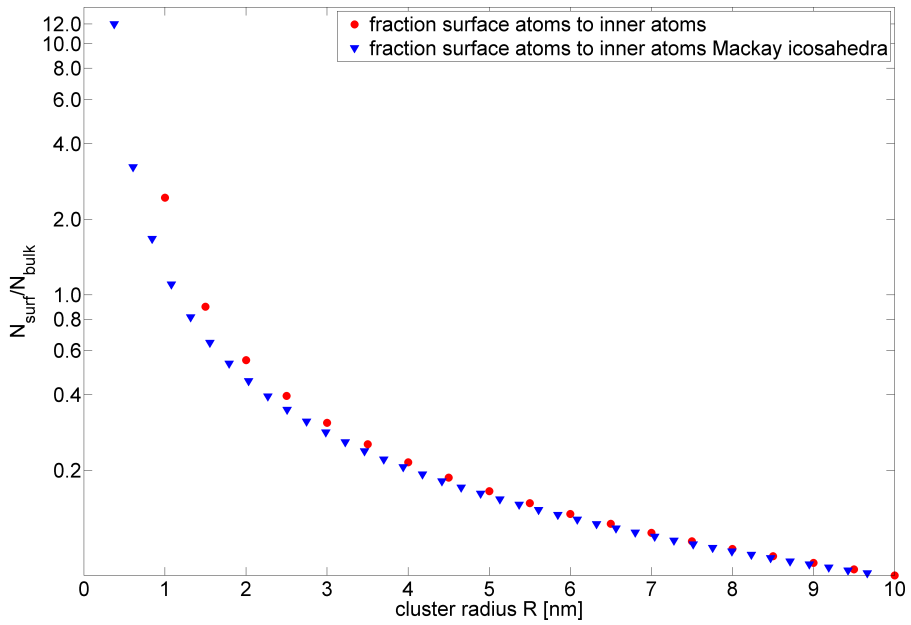

Figure 4.69: Half-logarithmic plot of the fraction of surface atoms to inner atoms of the cluster. Triangles: Fraction for the first eight Mackay icosahedra [Mac62] with 13, 55, 147, 309, 561, 923, 1,415 and 2,057 atoms, dots: Approximation for clusters of radius R with hexagonal close-packed atoms at the cluster surface (for further information see text).

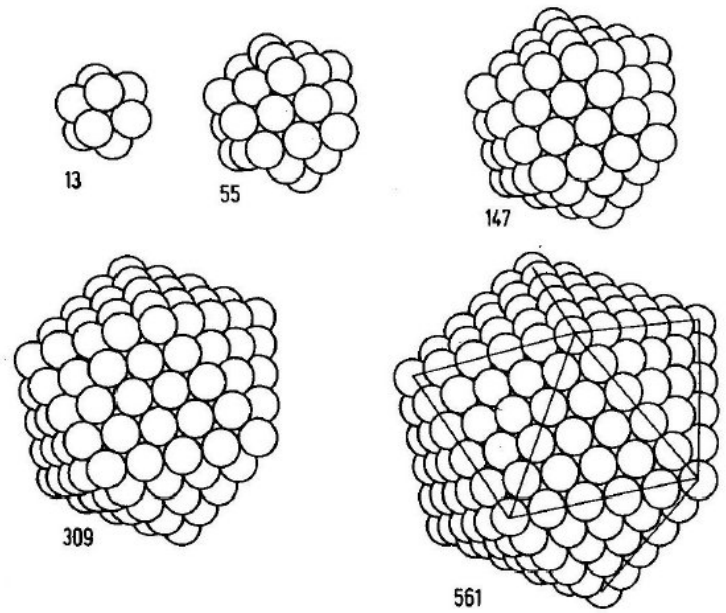

Figure 4.70: Scheme of the first five Mackay icosahedra with magic numbers N_1=13, N_2=55, N_3=147, N_4=309, N_5=561 [Jor84].

$N_{surf}/(N\text{-}N_{surf})_k=(N_k\text{-}N_{k\text{-}1})/N_{k\text{-}1}$ with $N_0=1$ and $R_k=[3/(4\pi)N_kV_{atom}\,]^{-1/3}$ [Höv00].
Regarding the fractions calculated for the superposition of the bulk and surface atoms spectra it is now possible to roughly approximate the cluster size on sample DO_11. In a first approximation of the cluster size for different cluster coverage the spectrum of the 0.09 ML clusters in PDMS is treated as the absorption resulting only from surface atoms (although the fraction $N_{surf}/(N\text{-}N_{surf})$ for clusters of a mean diameter of 2R=2 nm amounts to 1.3 (compare figure 4.69). Thus, the surface to inner atoms fractions amount to 0.2/0.8=0.25, 0.4/0.6=0.67, 0.5/0.5=1 and 0.8/0.2=4 for cluster coverage of 2.00 ML, 1.20 ML, 0.63 ML and 0.20 ML, respectively. This would yield sizes $2R_{0.20\ ML}$ ≈1 nm, $2R_{0.63\ ML}$ ≈2.3 nm, $2R_{1.20\ ML}$ ≈3 nm and $2R_{0.20ML}$ ≈6.5 nm (considering the Mackay icosahedra).
Considering the surface/bulk fraction of the 0.09 ML signal being formed by clusters with R≈1 nm to equal 1, a second approximation yields a surface to inner atom fraction of 0.1/(0.8+0.1)≈0.11, 0.2/(0.6+0.2)=0.25, 0.25/(0.5+0.25)≈0.33 and 0.4/(0.2+0.4)≈0.67 and thus cluster sizes $2R^*_{0.20\ ML}$ ≈3 nm, $2R^*_{0.63\ ML}$ ≈4.6 nm, $2R^*_{1.20\ ML}$ ≈5.2 nm and $2R^*_{2.00\ ML}$ ≈14 nm. The true cluster size might well be in between these two approximations since the fractions result from icosahedral Mackay clusters, which are likely to form for free clusters, but as mentioned above, not for supported.

4.4.3 Ag L_1 absorption edge

The Ag L_1 XANES spectra as calculated with FEFF9 for the highly symmetric Ag_{147} cluster are depicted in figure 4.71. Other than for the absorption spectra for L_2 and L_3 edge here the probed electron excitations are transitions from 2s to p states. The calculated spectra show the already for the Ag L_2 and L_3 edge observed structural changes with changing number of next-neighbors. While the XANES signal of the innermost atom (atom 1) exhibits pronounced structural features being a result of high multiple scattering probability due to a high number of next-neighbors and small next-neighbor distance of 2.73 Å, it shows remarkable similarities to the measured L_1 absorption edge of a 100 nm Ag reference film (see figure 4.72).
Other than for the previously discussed calculated Ag L_2 and L_3 absorption spectra, the XANES signal calculated for the first coordination shell around the innermost atom (denoted atom 2) looks quite similar to the two atoms belonging to the second coordination shell (namely atom 3 and atom 4). Otherwise, this is in good agreement with the fact that all of these atoms have 12 next-neighbors and a mean next-neighbor distance around 2.84 Å. Thus, these similarities of the spectra are reasonable.
The spectra calculated for the atoms belonging to the outer shell (atom 5, atom 6 and atom 7) do not look as similar as the calculated L_2 and L_3 edges of these atoms (figure 4.63 and 4.60, respectively). The spectral features of the outermost atom (atom 7) are comparably low due to the reduced multiple scattering probability at the only six next-neighbors.
Another remarkable feature is the fluctuation of the peak structure around 3.88 keV. Here, the feature does not only shift slightly with altering next-neighbor distance but changes significantly for the different absorbing atoms.
A comparison of the calculated Ag L_1 absorption edge of the Ag_{147} cluster, the calculated Ag L_1 edge of bulk silver and XANES measurements of the Ag L_1 edge of Ag clusters in PDMS, a 100 nm Ag film and a Ag_2O pellet is shown in figure 4.72. As can be clearly seen the calculated spectra do not show high similarity to the measured absorption spectra, not even for the bulk signal. This could well be a result of the differences between partial fluorescence yield used for the measurements and the total fluorescence yield FEFF calculations. For the calculated Ag bulk signal significant similarities between the measurement and the calculation can be seen. However, the experimental data show remarkably more spectral features than the calculation.
A direct comparison between the calculated cluster signal and the experimental data is difficult due to a considerable disagreement in the edge energy and the amplitude of the first feature, which could originate from the use of muffin-tin potentials in the ab-initio calculations [Reh10]. Thus, these calculations should be subject to further investigations.

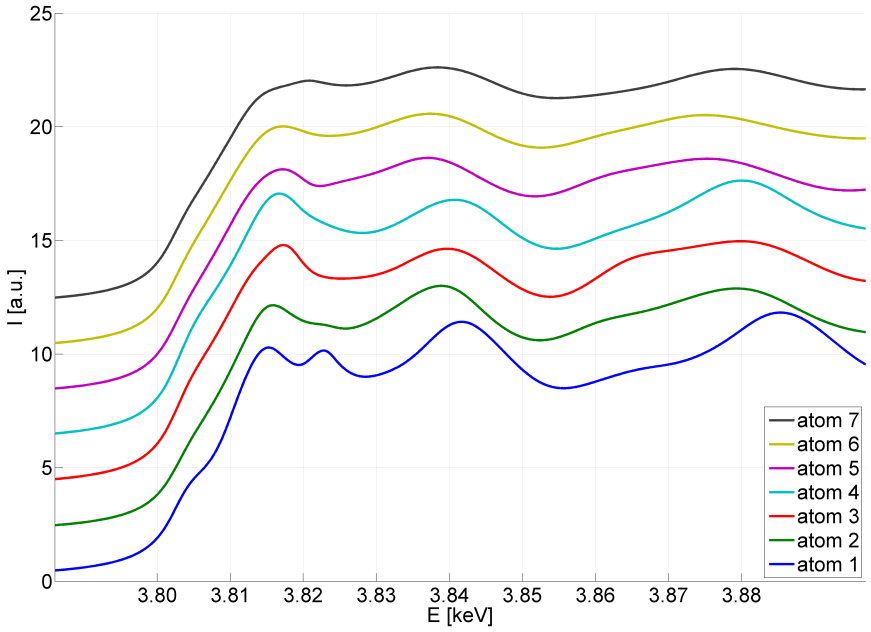

Figure 4.71: Calculated Ag L_1 XANES spectra of the Ag_{147} cluster (calculation done with FEFF9). Here, spectra for each of the different Ag atoms are shown individually.

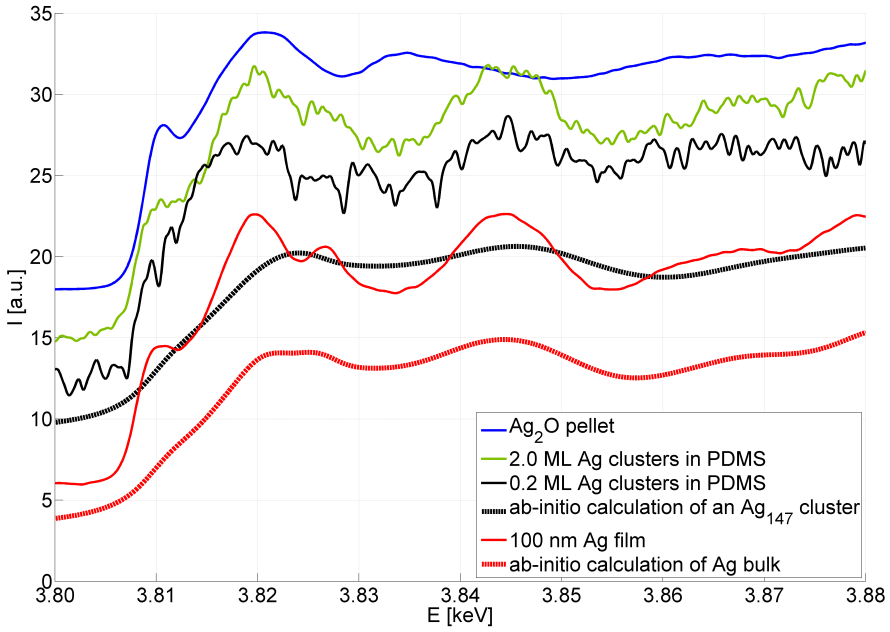

Figure 4.72: Comparison between the cluster Ag L_1 XANES measurements taken for clusters of different coverage in PDMS, a 100 nm silver film reference, a calculated silver bulk XANES spectrum and the Ag L_1 absorption edge as calculated for a Ag_{147} cluster.

4.4.4 Conclusions

In the last sections x-ray absorption near edge structure (XANES) experiments on Ag clusters of different coverage gradients on SiO_2 silica glass, in a polydimethylsiloxane (PDMS) matrix and in a SiO_2 aerogel matrix were presented. Additionally, ab-initio calculations were performed with FEFF9 [Reh10] to gain insight in the structural features of Ag clusters.

First XANES measurements of the Ag L_3 absorption edge in total fluorescence yield (TFY) of Ag clusters in PDMS and in SiO_2 aerogel were performed at BL8, DELTA, Dortmund. By comparison of the absorption spectra of cluster samples with different coverage and the Ag L_3 absorption edge measured on a 100 nm Ag film and a Ag_2O reference sample it was not only possible to prove the feasibility of XANES experiments on dilute samples such as clusters on surfaces or in different matrices, but also no detectable amount of oxide formation on the cluster surface due to the exposure of the samples to air could be found (figure 4.40). The reference sample spectra showed significant differences such as a pronounced white line at the onset of the L_3 absorption edge of the oxide, which can unambiguously be assigned to transitions from 2p to free final d states [Beh92a]. The lowest cluster signals show very few spectral features in the energy region of approx. 3.355-3.375 keV in contrast to the bulk silver absorption spectrum. For increasing cluster coverage similarities to the reference XANES signal evolve originating from cluster coalescence.
An additional experiment, in which a Ag cluster sample as well as a 100 nm Ag film were exposed to H_2S gas to sulfidise the silver and thus change the oxidation number showed significant similarities between the sulfidised clusters and film. Thus, a considerable oxide formation at the cluster surface would show in the absorption spectra. Showing a small white line in the onset of the absorption edge (figure 4.41) the sulfidised cluster signal can well be distinguished from the non-sulfidised clusters in aerogel.
Further experiments on the Ag L_3 absorption edge of Ag clusters in PDMS and in SiO_2 aerogel confirmed the afore mentioned findings of no detectable amount of oxide formation and structural changes in the energy region directly above the absorption edge, particularly the peak around 3.37 keV, which appears for low cluster coverage (compare figures 4.42 and 4.43). The increasing number of similarities to the silver reference signal with increasing cluster coverage is a clear sign for cluster coalescence and thus, a structural size effect.

The Ag L_2 absorption edge yields similar information as the Ag L_3 absorption edge, as both signals originate from excitations of 2p electrons to final d states (only difference being the spin state 1/2 for L_2 absorption and 3/2 for L_3 absorption). At ID26, ESRF, Grenoble, France, XANES experiments at the Ag L_2 absorption edge of Ag clusters in PDMS and on SiO_2 silica glass were performed. First measurements on the clusters on SiO_2 silica glass showed significant radiation damage after 3 scans with a scan time of 5 minutes each, which manifest in a shift of the absorption edge to lower energies and the formation of a pronounced white line. A comparison to reference signals measured at a AgO pellet and a Ag_2O pellet shows, that the Ag clusters are at least partly transformed to AgO after three scans of 5 minutes each (figure 4.44) and a reduction of the scan time to 60 seconds each results in reaction with the oxygen in the air around the sample to Ag_2O (figure 4.45). Even for a 100 nm Ag film those reactions due to x-ray damage could be

found. Thus, for further measurements the x-ray beam was moved across the sample to avoid the damage. Recent results in vacuum confirm that the visible radiation damage is a result of reactions with oxygen in the surrounding air. Measured in vacuum, no detectable damage was observed.
Experimental results on the Ag L_2 absorption edge of Ag clusters on SiO_2 silica glass compared to the Ag_2O reference and the Ag reference film show no similarities of the cluster absorption structure and the oxide structure, but for increasing coverage the absorption signal of the Ag clusters start to evolve bulk-like features (figures 4.47 and 4.48, respectively). The growing similarities to the silver bulk signal are a result of formation of larger islands on the SiO_2 surface, which is in good agreement with findings from optical spectroscopy measurements.
For the second investigated sample system with Ag clusters in PDMS also no detectable amount of oxide could be seen on the clusters. Comparison of x-ray absorption near edge spectra taken for cluster coverage of 0.09 ML to 2.00 ML shows the already for Ag clusters on SiO_2 observed formation of larger clusters with increasing cluster coverage resulting in the growing similarities to the Ag film signal (figure 4.50). For the lowest coverage there is a remarkable peak around approx. 3.533 keV, which can not be found in the absorption spectra for Ag clusters on SiO_2 silica glass. This structure could be a result from differently shaped clusters in the PDMS matrix (clusters on a substrate are oblate, in PDMS they are expected to be almost spherical) or from an influence of the matrix on the absorption of the cluster. The pronounced differences between the cluster absorption spectra and the Ag reference signal even up to higher coverage are a clear sign for better separation of the particles in the PDMS compared to the SiO_2 silica glass.

The XANES measurements of the Ag L_1 edge at clusters in PDMS are presented in figures 4.51 and 4.52 compared to Ag_2O and a Ag film signal, respectively. Other than the L_2 and L_3 absorption edges the Ag L_1 edge does not result from 2p electron excitations but from transitions from 2s electrons to unoccupied states. Due to the lower transition probability only the clusters in PDMS could be investigated. Within the limits of the error no significant similarities to the oxide signal could be detected. Possible structural differences compared to the Ag film signal could be seen with a slight change in the absorption feature and gaining similarities with increasing coverage. Nevertheless, this should be subject to further investigations to be able to confirm the trend.

In the second part of this section ab-initio calculations of all three Ag L absorption edges performed with FEFF9 were presented and compared to the measured cluster x-ray absorption near edge structure signals. Therefore, theoretically determined cluster coordination files with energetically preferable cluster structures were used [Hua11]. In principle it is necessary to calculate individual absorption spectra for each atom of the cluster. The cluster signal is thus a result of the sum over the absorption of each individual atom in the cluster. Due to the highly demanding calculations using CPU time it is of great interest to reduce the number of atoms, for which the spectra actually have to be calculated.
For two different clusters, the highly symmetric icosahedral Ag_{147} cluster and the axially symmetric Ag_{192}, the coordination files were analyzed by determining the distances of every atom to all other atoms in the cluster and grouping them according to their distance to the central atom (in both cases denoted atom 1). In the framework of a bachelor's

thesis [Mül12] was confirmed that for atoms with equal distances to all other atoms the calculated absorption spectra of each of these atoms look alike (figure 4.54). For the Ag_{147} cluster significant similarities between atoms belonging to one coordination shell could be found (figures 4.60, 4.63 and 4.71). While the XANES spectrum of the innermost atom shows numerous spectral features being a result of the pronounced full multiple scattering, which occurs due to a large number of potential scatterers around the absorbing atoms (next neighbors and surrounding shells), the atoms in the outer coordination shell show the lowest number of features in the absorption spectra. Directly above the absorption edge the spectra of the single atoms show remarkable changes, while a slight detectable shift in the higher energy region (around 3.4 keV for L_3, 3.575 keV for L_2 and 3.84 keV for L_1) can directly be assigned to fluctuations of the mean next-neighbor distances of the cluster atoms (compare table 4.2). The allocation of the atoms of the Ag_{147} cluster to the different coordination shells is comparably easy, since the cluster only consists of seven different atoms with respect to their distance to the central atom (see histogram of the distances to the central atom in figure 4.55). For more asymmetric clusters the distance to a central atom can no longer be the sole filter attribute considered to reduce the number of necessary calculations to a minimum. Here, additional attributes such as coordination angles should be considered. Even for the Ag_{192} with a comparably high symmetry the use of the distance to the central atom as sole filter attribute yields only a reduction to 21 single absorbing atoms.
In a first approach approximations were performed for the Ag_{147} cluster and compared to the exact simulation [Mül12]. It could be shown that using the mean value of all atoms in one shell (not weighted by their number of representatives) to determine the spectrum of the whole cluster (approximation 1) is as good an approximation of the real spectrum as the use of only the atom's spectrum, which has the highest number of representatives in the coordination shell (approximation 2, figure 4.73).
The very small differences between the exact Ag_{147} spectrum and the two approximations hint on a possible attempt to reduce CPU time for the calculations of asymmetric cluster spectra by approximating the absorption of the cluster in such a way.

Comparison of the L_3 XANES spectra calculated for the Ag_{147} cluster to the experimental data taken for Ag clusters in PDMS as well as a comparison between the calculated and measured absorption of bulk silver show significant similarities (figure 4.62). Almost all features of the measured 100 nm Ag film can be found in the calculated reference signal. The calculated cluster signal shows a significantly lower number of structural features as also seen in the signal for the low cluster coverage of 0.73 ML. However, the peak around 3.4 keV stays slightly below this value for the measured and calculated reference signals as well as the measured clusters' absorption spectra. In contrast the peak lies slightly above 3.4 keV for the calculated cluster signal. This is a first hint on structural similarities of the clusters to the bulk. Here, particularly the mean next-neighbor distances of the cluster atoms have to be taken into account.
The L_2 and L_1 absorption edges calculated for the Ag_{147} cluster show less similarities in comparison to measured signals of Ag clusters in PDMS (figures 4.64 and 4.72). Here, the reason for the pronounced differences and the higher number of features detected in the experimental data are a result of measuring in partial fluorescence yield, for which almost all background signals are suppressed, and calculations with integration over the

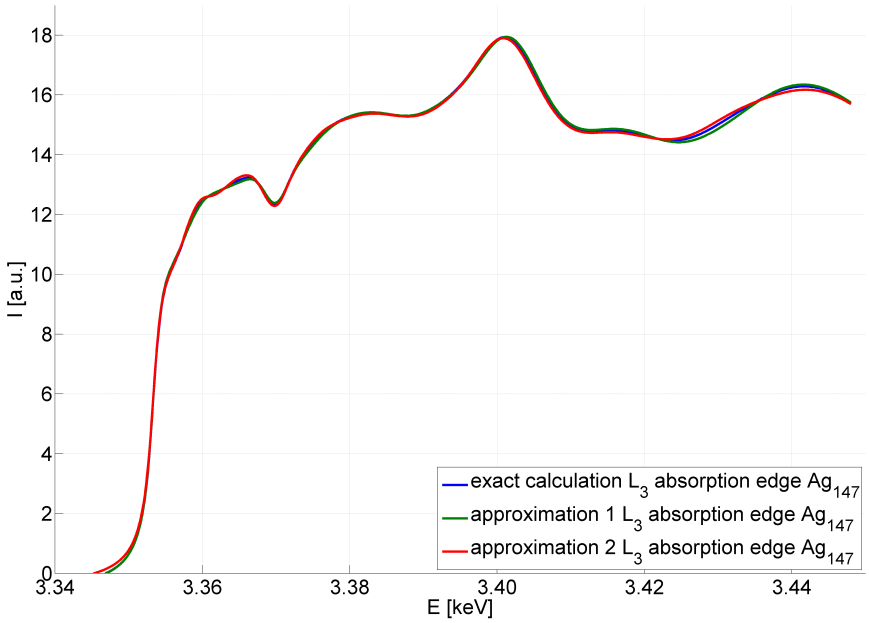

Figure 4.73: Exact Ag L_3 absorption edge calculated with FEFF and added up weighted with the number of representatives per atom compared to 2 different approximations. Approximation 1: Mean value of different atoms per shell times the number of atoms in the shell, approximation 2: Spectrum of the atom with most representatives in the shell times the number of atoms in the shell.

fluorescence energy $\hbar\omega_2$ (compare section 2.3.2). However, the calculated Ag L_2 XANES spectrum of the bulk silver shows a lot of similarities to the measured reference sample. For the cluster signals again a shift of the structure around 3.575 keV can be seen in the calculated absorption as a result of smaller next-neighbor distance, which is not present in the measured absorption of the clusters.

A closer look into the experimental data on the Ag L_2 edge of Ag clusters in PDMS shows, that the cluster signal can be treated as a superposition of two phases: the signal of bulk silver and the signal of surface atoms (figure 4.65). Attempts to simulate these data by superposition of the measured reference signal and the XANES signal for 0.09 ML Ag clusters in PDMS (approximated as sole surface atoms) as well as superpositions of the calculated signal from the outer cluster shell and the calculated silver bulk (figures 4.66 and 4.67, respectively) show remarkable similarities to the measured cluster spectra. Especially the bulk-like structures around 3.55 keV and 3.57 keV can be well simulated. In contrast, the attempt to reproduce the measured cluster absorption edges from a superposition of the calculated outer cluster shell and the innermost atom of the cluster shows significant differences, which can be assigned to the coordination and the next-neighbor distances of the inner atom in the calculated cluster structure. Thus, the structure of the Ag clusters in PDMS seems to be more bulk-like than the icosahedral structures of [Hua11].
Considering the surface to bulk atoms fraction of Mackay icosahedra to roughly estimate the size of the investigated clusters in the PDMS yielded a size range of approx. 3 nm to 14 nm for coverage of 0.20 ML up to 2.00 ML. Since the form of the clusters in PDMS is most probably not icosahedral this can only be accounted for as a very first approach to a more quantitative insight on the structure and size of Ag clusters in PDMS.
The calculated Ag L_1 edge of Ag_{147} clusters shows almost no similarities to the measured cluster signal (figure 4.72). Here, not only the significantly lower transition probability of the 2s electrons to free final states yields a decreased signal to noise ratio for the experimental data but also the calculated spectra show remarkably less features. This can be well seen in the comparison of the calculated signal of the Ag bulk reference and the measured absorption of the 100 nm Ag film. Nevertheless, there are similarities between the bulk signals and the overall form of these spectra is in good agreement. For the cluster signals additionally to the difference resulting from PFY compared to TFY (calculations) a significant edge shift and lowered amplitude of the absorption edge can be found in the calculated spectrum as a result of the overlapping muffin-tin potentials used in the FEFF9 calculation [Reh10]. Gaining experimental data in a higher resolution and additional calculations on the L_1 absorption edge should thus be subject to further investigations.

5 Summary and outlook

In the framework of this thesis Ag clusters deposited on a silica glass surface and into different matrix materials were investigated by means of optical spectroscopy and x-ray absorption near edge structure (XANES) spectroscopy of the Ag L absorption edges.
Optical measurements of the plasmon resonance of clusters showed behavior such as energy shifts with increasing cluster coverage, an additional energy shift after exposure to air and changes in the full width at half maximum of the measured extinction signals. The total plasmon energy as well as the value of the shifts strongly depend on the cluster environment and the amount of the deposited clusters. It could be shown, that a significantly high amount of Ag clusters can be deposited into a SiO_2 aerogel matrix yielding fairly separated clusters.
Since it is well known that structural properties such as size and shape of noble metal clusters influence the position of the plasmon resonance, it was highly important to gain additional information on the cluster samples under investigation. In particular, the energy shift after exposure to air, which can be assigned to formation of an adsorbate on the cluster surface, could not be explained to all extent by only regarding optical absorption spectra. To be able to determine the true origin of this shift and other structural changes XANES measurements of the Ag L absorption edges were performed.

For all three different sample systems (Ag clusters on SiO_2 silica glass, in polydimethylsiloxane (PDMS) and in SiO_2 aerogel) measurements of the Ag L absorption edges showed no significant oxide formation on the clusters. The high sensitivity of this method to changes in the oxidation state as proven by cluster sulfidisation experiments would yield a significant differences to the Ag bulk absorption for pronounced oxide formation. Thus, the lack of detectable changes shows that also the energy shift can not be a result from oxide formation. Here only the formation of an adsorption layer yielding no change in the oxidation number can be the origin of the detected energy shift, i.e. water layers. Such an adsorption layer could well induce a deformation of the clusters or changes in the local density of states yielding alterations in the x-ray absorption spectra of these clusters.

Combining the information obtained from these two different experimental methods provided a better insight into the properties of Ag cluster, particularly in matrices such as PDMS and SiO_2 aerogel. Taking into account the ab-initio calculations of a highly symmetric icosahedral Ag_{147} cluster as proposed to be an energetically preferable structure for free clusters [Hua11] changes in the XANES spectra for increasing cluster coverage with the transition to larger coalesced islands could be reproduced. The remaining discrepancies between calculation and measurement could be assigned to different values for the mean next-neighbor distance of the 7 considered atoms in the Ag_{147} cluster. Especially the comparison between the innermost atom with the lowest next-neighbor distance and the bulk

silver feature shows significant differences. Thus, the structure of the clusters in PDMS should be object to further investigations. Nevertheless, a first hint on more bulk-like distances could be found.

Additionally, in a first attempt is was possible to roughly approximate the size of clusters deposited into PDMS by taking into account the surface/inner atoms fraction and reconstructing the measured absorption spectra of different cluster coverage by superposition of calculated surface atom spectra and a bulk reference. This yielded an approximated size range of 3 nm for comparably low coverage and 14 nm for significantly higher cluster coverage.

The investigated samples were all prepared using a supersonic nozzle expansion. The clusters are not size selected, thus, all measured spectra contain information on Ag clusters exhibiting a certain size distribution. For future experiments the clusters will be size separated by ionization and deflection in an electric field. Thus, the structural investigations will yield a more precise insight in the geometrical and electronic structure of Ag clusters with a comparably narrow size distribution.

Further investigations on the Ag L_1 edge of Ag clusters have already been performed by David Engemann in very recent experiments. Possible size and structure dependent changes in the excitations resulting in the Ag L_1 absorption edge are thus still subject to subsequent research.

Future additional experiments on Ag clusters deposited onto previously heated SiO_2 silica glass are expected to provide interesting insight in the axial ratio of the clusters in this well defined sample system as well as possible pronounced coupling or even coalescence. Recent experimental data on Ag clusters in SiO_2 aerogel are analyzed at the moment.

Regarding ab-initio calculations for representative atoms in the clusters, considerations about possible filter attributes, which would help to reduce calculation time are planned. Thus, calculations on more asymmetric clusters could be performed in the future.

6 Bibliography

[Alo05] Alonso, J.A. *Structure and Properties of Atomic Nanoclusters*. Imperial College Press, 2005.

[And74] Anderson, J.B. *Molecular Beams and Low Density Gasdynamics*, page 1. M. Dekker, New York, 1974.

[Ank98] Ankudinov, A.L.; Ravel, B.; Rehr, J.J.; Conradson, S.D. Real-space multiple-scattering calculation and interpretation of x-ray-absorption near-edge structure. *Phys. Rev. B*, **58**:7565–7576., 1998.

[Bas75] Bassani, G.F.; and Parravicini, G.P. *Electronic states and optical transitions in solids Vol. 8*. Pergamon Press, 1975.

[Beh92a] Behrens, P. Bonding in silver-oxygen compounds from Ag L_3 XANES spectroscopy. *Solid State Commun.*, **81**:235–239, 1992.

[Beh92b] Behrens, P. X-ray absorption spectroscopy in chemistry II. X-ray absorption near edge structure. *Trends Anal. Chem.*, **11**:237–244, 1992.

[Beh99] Behrens, P.; Aßmann, S.; Bilow, U.; Linke, C.; Jansen, M. Electronic Structure of Silver Oxides Investigated by AgL XANES Spectroscopy. *Z. anorg. allg. Chem.*, **625**:111–116, 1999.

[Bie61] Bier, K.; Schmidt, B. Zur Form der Verdichtungsstöße in frei expandierenden Gasstrahlen. *Z. Angew. Phys.*, **13**:493–500, 1961.

[Bie62] Bier, K.; Hagena, O.F. Die Bedeutung von Verdichtungsstößen bei der Erzeugung intensiver Molekularstrahlen mit Düsen. *Z. Angew. Phys.*, **14**:658–664, 1962.

[Blu85] Blume, M. Magnetic scattering of x-rays. *J. Appl. Phys.*, **57**:3615–3618, 1985.

[Bob02] Bobbert, C.; Schütte, S.; Steinbach, C.; and Buck, U. Fragmentation and reliable size distributions of large ammonia and water clusters. *Eur. Phys. J. D*, **19**:183–192, 2002.

[Boh83] Bohren, C.F.; Huffman, D.R. *Absorption and scattering of light by small particles*. Wiley, New York, 1983.

[Bro12] Brolo, A.G. Plasmonics for future biosensors. *Nature Photonics*, **6** November:709–713, 2012.

[Bry07] Bryning, M.B.; Milkie, D.E.; Islam, M.F.; Hough, L.A.; Kikkawa, J.M.; and Yodh, A.G. Carbon nanotube aerogels. *Adv. Mater.*, **19**:661–664, 2007.

[Cor11] Corbelli, G.; Ghisleri, C.; Marelli, M.; Milani, P.; and Ravagnan, L. Highly Deformable Nanostructured Elastomeric Electrodes With Improving Conductivity Upon Cyclical Stretching. *Adv. Mater.*, **23**:4504–4508, 2011.

[Czy89] Czyżyk, M.T.; de Groot, R.A.; Dalba, G.; Fornasini, P.; Kisiel, A.; Rocca, F.; Burattini, E. Ag_2O band structure and x-ray-absorption near-edge spectra. *Phys. Rev. B*, **39**:9831–9838, 1989.

[Eck84] Eckardt, H.; Fritsche, L.; and Noffke, J. Self-consistent relativistic band structure of the noble metals. *J. Phys. F: Met. Phys.*, **14**:97–112, 1984.

[Ehr62] Ehrenreich, H.; Philipp, H.R. Optical Properties of Ag and Cu. *Phys. Rev.*, **128**:1622–1629, 1962.

[Far57] Faraday, M. The Bakerian Lecture: Experimental Relations of Gold (and Other Metals) to Light. *Philos. T. R. Soc. Lond.*, **147**:145–181, 1857.

[Fra85] Frank, F.; Schulze, W.; Tesche, B.; J. Urban, J.; and Winter, B. Formation of metal clusters and molecules by means of the gas aggregation technique and characterisation of size distribution. *Surf.Sci.*, **156**:90–99, 1985.

[Fri73] Fricke, J. Kondensation in Düsenstrahlen. *Physik in unserer Zeit*, **4**:21–27, 1973.

[Gan12] Gans, R. Über die Form ultramikroskopischer Goldteilchen. *Ann. Phys.*, **342**:881–900, 1912.

[Gau99] Gauthier , C.; Solé, V.A.; Signorato, R.; Goulon, J.; Moguiline, E. The ESRF beamline ID26: X-ray absorption on ultra dilute sample. *J. Synchrotron Rad.*, **6**:164–166, 1999.

[Gla05] Glatzel, P.; Bergmann, U. High resolution 1s core hole X-ray spectroscopy in 3d transition metal complexes-electronic and structural information. *Coord. Chem. Rev.*, **249**:65–95, 2005.

[Gla09] Glatzel, P.; Sikora, M.; Grigory Smolentsev, G.; Fernández-García, M. Hard X-ray photon-in photon-out spectroscopy. *Cat. Tod.*, **145**:294–299., 2009.

[Gsp86] Gspann, J. On the phase of metal-clusters. *Z. Phys. D*, **3**:143–145, 1986.

[Gup81] Gupta, R.P. Lattice relaxation at a metal surface. *Phys. Rev. B*, **23**:6265–6270, 1981.

[Hab92] Haberland, H. *Lehrbuch der Experimentalphysik*, chapter Cluster, pages 1–10. de Gruyter, 1992.

[Hae02] Haes, A.J.; Van Duyne, R.P. A nanoscale optical biosensor: Sensitivity and selectivity of an approach based on the localized surface plasmon resonance spectroscopy of triangular silver nanoparticles. *J. Am. Chem. Soc.*, **124**:10596–10604, 2002.

[Hag74] Hagena, O.F. Scaling laws for condensation in nozzle flows. *Phys.Fluids*, **17**:894–896, 1974.

[Hag81] Hagena, O.F. Nucleation and growth of clusters in expanding nozzle flows. *Surf.Sci.*, **106**:101–116, 1981.

[Hag87] Hagena, O.F. Condensation in Free Jets: Comparison of Rare Gases and Metals. *Z. Phys. D*, **4**:291–299, 1987.

[Hag91] Hagena, O.F. Formation of silver clusters in nozzle expansions. *Z. Phys. D*, **20**:425–428, 1991.

[Hen09] Hennes, S. *Herstellung und Charakterisierung von Clustern in einer Überschallexpansion.* Diploma thesis, Technische Universität Dortmund (unpublished), 2009.

[Hil01] Hilger, A. *Grenzflächen-Analyse durch Mie-Plasmon-Spektroskopie an Edelmetallclustern.* PhD thesis, Rheinisch-Westfälische Technische Hochschule Aachen, 2001.

[Hua11] Huang, W.; Lai, X.; Xu, R. Structural optimization of silver clusters from Ag_{141} to Ag_{310} using a Modified Dynamic Lattice Searching method with Constructed core. *Chem. Phys. Lett.*, **507**:199–202, 2011.

[Hub09] Hubenthal, F. Nanoparticles and their tailoring with laser light. *Eur. J. Phys.*, **30**:49–61, 2009.

[Hul84] Hulbert, S.L.; Bunker, B.A.; Brown, F.C. Copper $L_{2,3}$ near-edge structure in Cu_2O. *Phys. Rev. B*, **30**:2120–2126, 1984.

[Hum96] Humphrey, W.; Dalke, A.; and Schulten, K. VMD - Visual Molecular Dynamics. *J. Molec. Graphics*, **14**:33–38, 1996.

[Höv93] Hövel, H.; Fritz, S.; Hilger, A.; Kreibig, U.; Vollmer, M. Width of cluster plasmon resonances: Bulk dielectric functions and chemical interface damping. *Phys. Rev. B*, **48**:18178–18188, 1993.

[Höv95] Hövel, H. *Grenzflächeneigenschaften von Metallclustern.* PhD thesis, Rheinisch-Westfälische Technische Hochschule Aachen, 1995.

[Höv97] Hövel, H.; Hilger, A.; Nusch, I.; Kreibig, U. Experimental determination of deposition induced cluster deformation. *Z. Phys. D*, **42**:203–208, 1997.

[Höv00] Hövel, H. *Geometric and Electronic Structure of Nanoscale Systems on Surfaces.* Habilitation treatise, Universität Dortmund, 2000.

[Jan10] Jansen, R.; Wysong, I.; Gimelshein, S.; Zeifman, M.; and Buck, U. Nonequilibrium numerical model of homogeneous condensation in argon and water vapor expansions. *J. Chem. Phys.*, **132**:244105, 2010.

[Jan11] Jansen,R.; Gimelshein,N.; Gimelshein, S.; and Wysong, I. A Lagrangian-Eulerian approach to modeling homogeneous condensation in high density gas expansions. *J. Chem. Phys.*, **134**:104105, 2011.

[Jor84] Jortner, J. Level structure and dynamics of clusters. *Ber. Bunsenges.*, **88**:188–201, 1984.

[Kis31] Kistler, S.S. Coherent Expanded Aerogels and Jellies. *Nature*, **127**:741–741, 1931.

[Kis34] Kistler, S.S.; Caldwell, A.G. Thermal Conductivity of Silica Aërogel. *Ind. Eng. Chem.*, **26**:658–662, 1934.

[Kon88] Koningsberger, D.C. *X-ray absorption: principles, applications, techniques of EXAFS, SEXAFS and XANES.* John Wiley and Sons Inc., New York, NY, 1988.

[Kra72] Kramer, B. *Festkörperprobleme XII*, page 133. Pergamon, Vieweg, 1972.

[Kra76] Kramer, B. *Physics of Structurally Disordered Solids*, page 369. Plenum Press, New York, 1976.

[Kra05] Krasnochtchekov, P.; Averback, R.S. Molecular dynamics simulations of cluster nucleation during inert gas condensation. *J. Chem. Phys.*, **122**:044319, 2005.

[Kre69] Kreibig, U.; Fragstein, C.v. The Limitation of Electron Mean Free Path in Small Silver Particles. *Z. Phys.*, **224**:307–323, 1969.

[Kre70] Kreibig, U. Kramers Kronig Analysis of Optical Properties of Small Silver Particles. *Z. Phys.*, **234**:307–318, 1970.

[Kre74] Kreibig, U. Electronic properties of small silver particles: the optical constants and their temperature dependence. *J. Phys. F*, **4**:999–1014, 1974.

[Kre85] Kreibig, U.; Genzel, L. Optical absorption of small metallic particles. *Surf. Sci.*, **156**:678–700, 1985.

[Kre95] Kreibig, U.; Vollmer, M. *Optical Properties of Metal Clusters.* Springer: Berlin, 1995.

[Kre98] Kreibig, U.; Gartz, M.; Hilger, A.; Hövel, H. *Advances in Metal and Semiconductor Clusters Vol. 4*, chapter Optical Investigations of Surfaces and Interfaces of Metal Clusters, page 345. JAI press Inc., 1998.

[Lan09] Lange, J.J.; Collinson, M.M.; Culbertson, C.T.; and Higgins, D.A. Single-Molecule Studies of Oligomer Extraction and Uptake of Dyes in Poly(dimethylsiloxane) Films. *Anal. Chem.*, **81**:10089–10096, 2009.

[Lat11] Latussek, K.W. *Optische Eigenschaften und Röntgenabsorptionsspektroskopie von Ag Clustern auf SiO_2-Substrat und in Polydimethylsiloxan.* Diploma thesis, Technische Universität Dortmund (unpublished), 2011.

[Law] Lawrence Berkeley Laboratories: Microstructured Materials Group. Silica Aerogels. online.

[Leo07] Leonhardt, U. Invisibility cup. *Nature Photonics*, **1** April:207–208, 2007.

[Lev09] Leventis, N.; Chandrasekaran, N.; Sotiriou-Leventisa, C.; and Mumtaz, A. Smelting in the age of nano: iron aerogels. *J. Mater. Chem.*, **19**:63–65, 2009.

[Ley08] Leydecker S. *Nanomaterialien*, chapter Entwicklung der Nanotechnologie, pages 20–25. Birkhäuser Basel, 2008.

[Li,08] Li, Z.Y.; Young, N.P.; Di Vece, M.; Palomba, S.; Palmer, R.E.; Bleloch, A.L.; Curley, B.C.; Johnston, R.L.; Jiang, J.; Yuan, J. Three-dimensional atomic-scale structure of size-selected gold nanoclusters. *Nature*, **451**:46, 2008.

[Lüt09] Lützenkirchen-Hecht, D.; Wagner, R.; Haake, U.; Watenphul, A.; and Frahm, R. The materials science X-ray beamline BL8 at the DELTA storage ring. *J. Synchrotron Rad.*, **16**:264–272., 2009.

[Mac62] Mackay, A.L. A dense non-crystallo ,raphic packing of equal spheres. *Acta Cryst.*, **15**:916–918, 1962.

[Mer08] Merlein, J.; Kahl, M.; Zuschlag, A.; Sell, A.; Halm, A.; Boneberg, J.; Leiderer, P.; Leitenstorfer, A.; Bratschitsch, R. Nanomechanical control of an optical antenna. *Nature Photonics*, **4**:230–233, 2008.

[Mie08] Mie, G. Beiträge zur Optik trüber Medien, speziell Kolloidaler Metallösungen. *Ann. Phys.*, **25**:377–445, 1908.

[Miy10] Miyamoto, T; Niimi, H.; Kitajima, Y; Toshio Naito, T; and Asakura, K. Ag L_3-Edge X-ray Absorption Near-Edge Structure of 4d10 (Ag+) Compounds: Origin of the Edge Peak and Its Chemical Relevance. *J. Phys. Chem. A*, **114**:4093–4098, 2010.

[Mül12] Müller, D. *Herstellung von Silber-Clustern und Untersuchung mit Röntgenabsorptionsspektroskopie sowie FEFF.* Bachelor's thesis, Technische Universität Dortmund (unpublished), 2012.

[Nap04] Napari, I.; Vehkamäki, H.; Laasonen, K. Molecular dynamic simulations of atom-cluster collision processes. *J. Chem. Phys.*, **120**:165–169, 2004.

[Org58] Orgel, L.E. Stereochemistry of Metals of the B Sub-groups. Part I. Ions with Filled d-Electron Shells. *J. Chem. Soc.*, pages 4186–4190, 1958.

[Ott61] Otter, M. Temperaturabhängigkeit der optischen Konstanten massiver Metalle. *Z. Phys.*, **161**:539–549, 1961.

[Ott91] Otto, A. Surface-Enhanced Raman Scattering of Adsorbates. *J. Raman Spectrosc.*, **22**:743–752, 1991.

[Pat06] Patrito, N.; McCague, C.; Chiang, S.; Norton, P.R.; and Petersen, N.O. Photolithographically Patterned Surface Modification of Poly(dimethylsiloxane) via UV-Initiated Graft Polymerization of Acrylates. *Langmuir*, **22**:3453–3455, 2006.

[Per93] Persson, B.N.J. Polarizability of small spherical metal particles: influence of the matrix environment. *Surf. Sci.*, **281**:153–162, 1993.

[Qui11] Quinten, M. *Optical Properties of Nanoparticle Systems.* Wiley-VCH Verlag & Co. KGaA, Germany, 2011.

[Rav09] Ravagnan, L.; Divitini, G.; Rebasti, S.; Marelli, M.; Piseri, P.; and Milani, P. Poly(methyl methacrylate)-palladium clusters nanocomposite formation by supersonic cluster beam deposition: a method for microstructured metallization of polymer surfaces. *J. Phys. D*, **42**:082002, 2009.

[Reh00] Rehr, J.J.; Albers, R.C. Theoretical approaches to x-ray absorption fine structure. *Rev. Mod. Phys.*, **72**:621–654., 2000.

[Reh10] Rehr, J.J.; Kas, J.J.; Vila, F.D.; Prange, M.P., Jorissen, K. Parameter-free calculations of X-ray spectra with FEFF9. *Phys. Chem. Chem. Phys.*, **12**:5503–5513., 2010.

[Rot09] Roth, J. *Funktionalisierung von Silikonoberflächen.* PhD thesis, Technische Universität Dresden, 2009.

[Sah11] Sahle, Ch.J. *Temperature and pressure induced changes in the local atomic and electronic structure of complex materials.* PhD thesis, Technische Universität Dortmund, 2011.

[Sal11] Salmen, P. *Untersuchung des Polymers Polydimethylsiloxan (PDMS) zur Deposition von Silberclustern.* Bachelor's thesis, Technische Universität Dortmund (unpublished), 2011.

[Sch84] Schumacher, E.; Kappes, M.; Marti, K.; Radi, P.; Schar, M.; Schmidhalter, B. Metal-Clusters - Preparation, properties, theory. *Ber. Bunsenges.*, **88**:220–228, 1984.

[Sch07] Schülke, W. *Electron Dynamics by Inelastic X-Ray Scattering.* Oxford University Press, UK, 2007.

[Tei76] Teichner, S.J.; Nicolaon, G.A.; Vicarini, M.A.; Gardes, G.E.E. Inorganic oxide aerogels. *Adv. Colloid Interface Sci.*, **5**:245–273, 1976.

[Weg70] Wegener, P.P.; Parlange, J.-Y. Condensation by homogeneous nucleation in the vapor phase. *Naturwissenschaften*, **11**:525–533, 1970.

[Wer85] Wern, H. *Winkelaufgelöste Ultraviolett-Photoelektronenspektroskopie an Silber zur Bestimmung der elektronischen Struktur und empirische Berechnungen zur Bandstruktur und den optischen Eigenschaften der d-Band Metalle Kupfer und Silber.* PhD thesis, Universität des Saarlandes, 1985.

[Wes00] Westphalen, M.; Kreibig, U.; Rostalski, J.; Lüth, H.; Meissner, D. Metal cluster enhanced organic solar cells. *Sol. Energ. Mat. Sol. C.*, **61**:97–105, 2000.

[Wut92] Wutz, M.; Adam, H.; Walcher, W. *Theorie und Praxis der Vakuumtechnik.* Vieweg-Verlag: Braunschweig, 1992.

[Yam74] Yamaguchi, T.; Yoshida, S.; and Kinbara, A. Optical effect of the substrate on the anomalous absorption of aggregated silver films. *Thin Solid Films*, **21**:173–187, 1974.

[Yan92] Yanase, A.; Komiyama, H. In situ optical observation of oxygen-adsorption-induced reversible change in the chape of small supported silver particles. *Surf. Sci.*, **264**:147–156, 1992.

[Yan09] Yano,J.; Yachandra, V.K. X-ray absorption spectroscopy. *Photosynth. Res.*, **102**:241–254, 2009.

[Yos71] Yoshida, S.; Yamaguchi, T.; Kinbara, A. Optical Properties of Aggregated Silver Films. *J. Opt. Soc. Am.*, **61**:62–69, 1971.

Acknowledgments

Nun ist es an der Zeit, ein kurzes Dankeschön an all diejenigen zu richten, die mich während des Entstehens meiner Doktorarbeit begleitet und unterstützt haben.

An erster Stelle möchte ich mich bei meinem Doktorvater Prof. Dr. Heinz Hövel bedanken für die Möglichkeit diese Arbeit in seiner Arbeitsgruppe zu erstellen. Insbesondere großen Dank für das Vertrauen, das Du mir entgegengebracht hast und Dein anhaltendes Interesse an unserer Forschung, was sich auch durch rege Teilnahme an unseren Experimenten und inspirierenden Diskussionen immer wieder gezeigt hat.

Ein herzliches Dankeschön an Herrn Prof. Dr. Shaukat Khan für die Übernahme der Zweitkorrektur meiner Dissertation und das Interesse an meiner Arbeit auch im Zusammenhang mit DELTA, Dortmund.

Vielen Dank an Herrn Prof. Dr. Metin Tolan, für die Möglichkeit im Rahmen der NRW Forschungsschule - "Forschung mit Synchrotronstrahlung in den Nano- und Biowissenschaften" zu promovieren.

Herrn Prof. Dr. Uwe Kreibig möchte ich herzlich danken für die Möglichkeit, THECLA zu übernehmen und somit an dieser Anlage meine Arbeit zu verfassen.

Nicht zu vergessen sind meine Freunde Dr. Martin A. Schroer, Dr. D.C. Florian Wieland und insbesondere Dr. Christoph J. Sahle, welche mir nicht nur den Arbeitsalltag durch Gespräche und Späße verschönert haben (besonders mein Büropartner Martin) sondern auch fachlich und im Umgang mit Auswerte-Software immer mit Rat und Tat zur Seite standen. In dem Sinne auch noch einmal vielen Dank an Christoph für die Hilfe bei der Einarbeitung in FEFF.
Natürlich soll hier auch Dr. Sebastian Tiemeyer, mein zweiter Büronachbar nicht unerwähnt bleiben. Danke Sebo, für die angenehme Atmosphäre in unserem Büro und Deine regelmäßigen Hilfe, beim Kampf mit Matlab.

Ein großes Dankeschön möchte ich auch an die Diplom- und Bachelorstudenten Dipl.-Phys. Kamil W. Latussek, B.Sc. Paul Salmen, B.Sc. David Müller und B.Sc. Erik Kierstein aussprechen, deren Arbeiten ich während meiner Dissertationszeit betreuen durfte. Durch Euer großes Engagement war es erst möglich die Experimente im Rahmen dieser Arbeit erfolgreich zu planen und durchzuführen.

Vielen Dank auch an Dr. Axel Enders für die tolle Betreuung während meiner Aufenthalte an der University of Licoln, Nebraska, USA. Vielen Dank, dass Du und Deine Familie mich

so herzlich aufgenommen habt.

Vielen Dank auch an alle, die bei meinen Experimenten tatkräftig mitgeholfen haben, besonders Frau Dr. Stefanie Duffe und Herrn David Engemann. Natürlich auch den Betreuern der Strahllinien Ralph Wagner und Stefan Balk (BL8, DELTA, Dortmund) und Dr. Pieter Glatzel und Kristina Kvashnina (ESRF, Grenoble, Frankreich) ein großes Dankeschön für die Hilfe und gute Betreuung während der Strahlzeiten.
Ebenso zu erwähnen sind alle meine Kollegen des Lehrstuhls E1a, für interessante Gespräche auch mal abseits der Physik.

Nachdem nun hoffentlich alle Kollegen und besonderen Freunde mit Danksagungen bedacht wurden (sollte ich jemanden vergessen haben, so möge man es mir verzeihen), ist es nun an der Zeit mich bei meiner Familie zu bedanken.
Allen voran möchte ich ein dickes Dankeschön aussprechen an meine Eltern, die mich in allen Dingen meines Lebens unterstützen und mir immer mit Rat und Tat zur Seite stehen. Ihr seid einfach die besten, danke.
Auch meine Schwiegereltern haben mich in den letzten drei Jahren sehr gut unterstützt und mir viele Dinge abgenommen, die in stressigen Phasen der Dissertation auch mal liegen geblieben sind. Dankeschön dafür und auch für die Nervennahrung, mit der Ihr mich in den letzten Wochen immer versorgt habt.
Auch meine Schwester und mein kleiner Neffe haben mir in den letzten Wochen immer wieder geholfen, mich auf das wesentliche zu konzentrieren, indem sie mir kurze Ausflüge weg vom Dissertationsalltag ermöglicht haben (wie sehr einen ein Besuch in einer Krabbelgruppe doch zerstreuen und ablenken kann!!).

Und nun an exponierter Stelle möchte ich meinem Ehemann Lars Hoffmann danken dafür, dass er mich während meines Studiums schon durch den Stress der Diplomarbeit begleitet hat und nicht nach meiner Entscheidung zur Promotion einfach weggelaufen ist. Du bist mein Halt, wenn ich glaube, einer Situation nicht gewachsen zu sein. Danke, dass Du mich in meinem Leben und bei allem was ich mache begleitest.

Eidesstattliche Versicherung

Hiermit erkläre ich an Eides Statt, dass die vorliegende Dissertationsschrift - abgesehen von der Beratung durch meine wissenschaftlichen Betreuer - nach Inhalt und Form meine eigene Arbeit ist. Sie wurde weder ganz noch in Teilen an anderer Stelle im Rahmen eines Prüfungsverfahrens vorgelegt.

Dortmund, den

_____
(Sabrina Hoffmann)